AN ABSTRACT OF THE THESIS OF

Kirk W. Brown for the degree of Doctor of Philosophy in Chemistry presented on October 11, 1991

Title: Coherent Raman Spectroscopy of Non-Polar Molecules and Molecular Clusters

Redacted for Privacy

Abstract approved:

Coherent Raman spectroscopy was used to examine rotational and rovibrational transitions of three non-polar molecules in various states. First, through a combination of pure rotational stimulated Raman spectroscopy (SRS) and electron-diffraction, the gas-phase structure of dicyanoacetylene (C_4N_2) was determined. The diffraction data yield r_α^0 bond lengths of $r_{C\equiv N}$ = 1.161(5) Å, r_{C-C} = 1.367(3) Å, and $r_{C\equiv C}$ =1.198(11) Å for the linear geometry. Harmonic corrections used with the bond lengths give a calculated value of 0.044891 (86) cm^{-1} for the ground-state rotational constant, B_0. Unresolved contributions from thermally populated bending modes prevented determination of B_0 directly from the Raman data but an analysis of the maxima of the rotational bands gives an average value B_{av} = 0.044867(19) cm^{-1}.

A high resolution low-frequency coherent anti-Stokes Raman spectroscopy

(CARS) apparatus was developed for pure rotational Raman spectroscopy and the closely spaced $\Delta N=2$, $\Delta J=2$ triplets of oxygen from N = 1-19 were resolved for the first time. The transition frequencies extracted from the experimental data agree very well with those calculated using molecular parameters obtained from magnetic dipole microwave spectroscopy and a Hund's case a,b coupling Hamiltonian.

Molecular clusters are of significant interest currently, and a range of sizes of carbon dioxide clusters formed in a free jet expansion were examined. Using high jet driving pressures, bulk-like solid clusters were formed which exhibit distinct A_g and T_g modes in the vibrational CARS spectra, evidence that the clusters are crystalline rather than amorphous. Under less condensing expansion conditions, a number of other features were observed which exhibited strong dependence on the source pressure and temperature. These are attributed to small (<5000 molecules) clusters and probably arise from vibrations of molecules on the surface of the clusters.

Finally, a series of new sharp features immediately surrounding the monomer Q-branch peak in the ν_1 CARS CO_2 spectrum were observed in a mildly condensing CO_2 jet expansion and are attributed to rovibrational structure of the carbon dioxide dimer.

COHERENT RAMAN SPECTROSCOPY OF NON-POLAR MOLECULES AND MOLECULAR CLUSTERS

by

Kirk W. Brown

A THESIS

submitted to

Oregon State University

in partial fulfillment of
the requirements for the
degree of

Doctor of Philosophy

Completed October 11, 1991

Commencement June 1992

APPROVED:

Redacted for Privacy

Professor of Chemistry in charge of major

Redacted for Privacy

Head of Department of Chemistry

Redacted for Privacy

Dean of Graduate School

Date thesis is presented October 11, 1991

Typed by Kirk W. Brown

ACKNOWLEDGEMENTS

Many people have helped to make this a great four years at Oregon State University. First and foremost, is my wife Ruth. Her constant support and love made it easy to accomplish the goals that we set when we came to Corvallis. I want to thank her for being a wonderful mother to our two boys, Christopher and Aaron, who have been a very bright spark of joy in my life.

I want to give a big thanks to my advisor and friend, Professor Joe Nibler. He has taught me many important things, some that he probably doesn't even realize. As I look at the knowledge that I have gained while at OSU, I count Raman spectroscopy as but a minor portion. How to think logically, how to carry through on projects, how to treat people with kindness and respect, how to attack a problem with the idea of finding the perfect solution the first time...these and many more lessons have come my way from Joe and I am deeply appreciative. Some of the fondest memories I have of working in the lab were of Saturday afternoons when no one else was around. Joe would come in and together we would tackle some experimental problem. Without fail, within a few hours, the problem would be solved in a most ingenious way with the resulting experiment being even better than before. I am very grateful to have had the opportunity to learn from him.

I would also like to acknowledge the assistance of various individuals who have helped directly with the work in this thesis. In the C_4N_2 work, Rainer Beck took the Raman Loss data and Dr. Kenneth Hedberg and Dr. Lise Hedberg guided me through a working tutorial on electron diffraction. The experimental and

theoretical assistance of Dr. Nathan Rich during the oxygen work is greatly appreciated. The many months that Mansour Zahedi spent developing the spectral convolution routines used to model the O_2 spectra are also very much appreciated. Nathan, along with Alan Richardson, obtained the experimental results in the equilibrium condensed phase study of carbon dioxide which served as an invaluable guide to deciphering the cluster spectra.

Many more people have been very supportive and friendly to me and I would like to collectively acknowledge all the great people that I have been fortunate enough to meet while in Corvallis.

TABLE OF CONTENTS

LIST OF FIGURES

Figure

LIST OF TABLES

COHERENT RAMAN STUDIES OF NON-POLAR MOLECULES AND MOLECULAR CLUSTERS

CHAPTER 1 COHERENT RAMAN SPECTROSCOPY

INTRODUCTION

In the diverse field of molecular spectroscopy, many different techniques have been developed to examine the fundamental properties of molecules. Some of these properties can be explored with techniques that probe the rotational and vibrational motions that are induced by electromagnetic radiation impinging upon the species of interest. For example, microwave and infrared spectroscopy can be used to examine respectively rotational and vibrational transitions within the ground electronic state. Both of these techniques rely primarily on the induction of a change in the permanent electric dipole moment of the molecule. If the molecule does not possess a permanent electric dipole moment however, no microwave pure rotational spectrum can typically be observed and the infrared spectrum will only reveal vibrations that give the molecule a non-zero average dipole moment.

This niche can filled by Raman spectroscopy, however, since transitions are allowed not on the basis of a dipole moment change but rather on the basis of the polarizability of the sample, or in other words the deformability of the electron cloud surrounding the molecule. Thus, a pure rotational spectrum is attainable

through Raman techniques for any molecule except those with spherical top symmetry (where rotation does not alter the perfect sphericity of the polarizability). Furthermore, vibrational-rotational spectra are attainable for the transitions of homonuclear diatomics and of polyatomic molecules that do not result in a net dipole moment change. This thesis is devoted to the examination by coherent Raman techniques of three such non-polar molecules, dicyanoacetylene, oxygen, and carbon dioxide.

Chapter II presents the first reported structural analysis of gas-phase dicyanoacetylene, C_4N_2, obtained by pure rotational stimulated Raman spectroscopy (SRS) and electron-diffraction techniques. C_4N_2 is the longest known stable linear molecule and is believed to exist in the atmostphere of Titan, one of the moons of Saturn. Because of its length, C_4N_2 is easily bent and at room temperature, several low-frequency bending modes are thermally populated. Since the molecule rotates at a slightly different frequency in each of these bent configurations, the SRS pure rotational spectrum is somewhat convoluted and only an average rotational constant, B_{av} is determinable. Therefore, a gas-phase electron-diffraction study was performed in collaboration with Dr. Kenneth Hedberg and Dr. Lise Hedberg to obtain ground state structural parameters. The SRS and electron-diffraction results as well as results from *ab initio* calculations are analyzed and discussed.

In Chapter III, the pure rotational Raman spectrum of O_2 is presented as a demonstration of a newly developed high resolution low frequency coherent anti-Stokes Raman spectroscopy (CARS) apparatus. Each O_2 rotational "line" actually is comprised of six transitions, three of which are separated by only ~0.02 cm^{-1}.

These triplets are resolved here for the first time. The peak frequencies, obtained from a modeling of the CARS spectra, match well with frequencies obtained in a calculation of the spectrum using a Hamiltonian appropriate to an angular momentum coupling scheme intermediate between Hund's case (a) and (b) with molecular constants obtained from magnetic quadrupole microwave spectroscopy.

In Chapter IV, vibrational CARS is used to examine medium-to-large CO_2 clusters formed in a free jet expansion. The frequencies and linewidths of spectral peaks arising from these clusters are very sensitive to temperature and a comparison with equilibrium solid CO_2 spectra elucidates the cooling rates of the large ($>10^5$ molecules) clusters as they travel in the free jet expansion. Also, several intriguing spectral features are visible when jet expansion conditions are used that favor the formation of somewhat smaller (<5000 molecules) clusters. The possible origin of these features is discussed in light of different theories regarding the growth of small clusters.

Chapter V presents a group of heretofore unseen, sharp peaks observed in the vibrational CARS spectrum of CO_2. These regularly spaced peaks surrounding the ν_1 CO_2 monomer peak are attributed to the rovibrational spectrum of the CO_2 dimer. This marks the first rotationally resolved Raman spectrum of a molecular dimer. First, however, a brief description of the common thread to all of these experiments, coherent Raman spectroscopy, will be presented with relevant references cited for the interested reader.

RAMAN SPECTROSCOPIC TECHNIQUES

Spontaneous Raman scattering was first discovered in 1928 by Sir Chandrasekhara V. Raman[1] but its early use was somewhat limited by the lack of a sufficiently intense light source. This changed with the discovery of the laser in 1960, which provided the needed, extremely high intensity source of light. The intensity of the laser emission is so great, in fact, that the interaction of the radiation with the sample can induce nonlinear effects. This was first reported in 1962 by Woodbury and Ng[2] in the discovery of stimulated Raman scattering followed by the observation of CARS by Maker and Terhune in 1965[3]. The subsequent development of commercially available Nd:YAG and tunable dye lasers accelerated the development of various coherent Raman spectroscopic techniques including stimulated Raman gain (SRG) and loss (SRL) spectroscopy. (In this thesis, the related (SRG) and (SRL) techniques will simply be denoted as stimulated Raman spectroscopy (SRS).)

All of these coherent Raman techniques enjoy higher spectral resolution and sensitivity than spontaneous Raman scattering due to fundamental differences in the light scattering process. In conventional Raman spectroscopy, an incident photon is coupled with a scattered photon in an inelastic collision with the molecule. Most of the scattered photons will be of the same frequency as the incident photons (Rayleigh scattering) but some will be lower (Stokes) or higher (anti-Stokes) in frequency by an amount that coincides with the vibrational or rotational energy

levels of the molecule. In coherent Raman spectroscopy, however, the light of two or three intense laser beams is coupled in a non-linear fashion in the sample, producing a signal that is a coherent laser-like beam.

This can be observed in Figure 1.1 which depicts the processes involved in CARS (a), and SRS (b). In the normal CARS process, two intense beams, ω_1 and ω_2, drive the molecule into an upper vibrational or rotational state when the frequency difference between the two beams matches a resonance in the molecule. A third beam, ω_1', pumps the molecule into a virtual level from which a fourth coherent laser-like beam, ω_3, is emitted to bring the molecule back to the initial state. This ω_3 beam can be separated from the input beams either spatially as in the case of the folded BOXCARS arrangement[4] used here, or with filters and polarizers when all of the input beams are collinear. In the SRS process, two beams, ω_1 and ω_2, are focused on the sample. When a molecular resonance occurs, the intensity of the higher frequency beam is diminished and the intensity of the lower frequency beam is augmented. Thus the signal is detected by measuring the change in intensity of either beam when resonance occurs.

The CARS and SRS processes offer many advantages over conventional Raman spectroscopy. For example, the spectral resolution in a gas-phase CARS or SRS experiment is limited by the linewidths of the input lasers rather than by the slitwidths of a monochromator as is the case in conventional spontaneous Raman experiments. Also, the crossed, tightly focused input beams in CARS and SRS define a very small sampling volume, thus allowing the spatial probing of different areas in the sample, an important feature in the examination of free jet expansions.

The theoretical and mathematical framework for all of the coherent Raman processes has been thoroughly discussed in a number of excellent articles and reviews[5-25]. The practical aspects of the various techniques will be discussed in the Experimental sections of the following chapters.

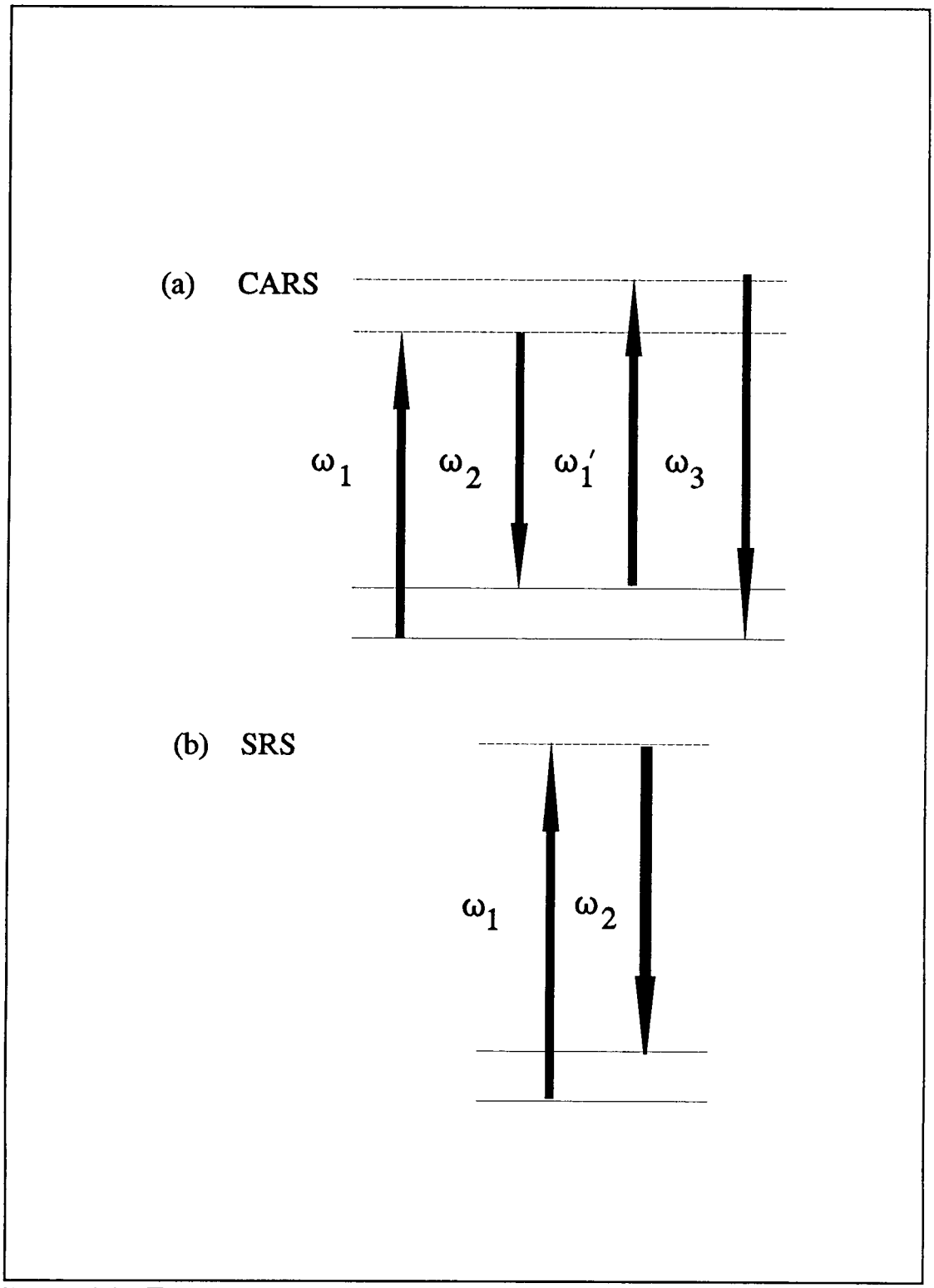

Figure 1.1: Energy level diagrams for CARS (a), and SRS (b). The increased width of ω_2 in (b) depicts the augmented intensity of this beam that occurs with a molecular resonance.

CHAPTER 2 THE STRUCTURE OF DICYANOACETYLENE BY ELECTRON DIFFRACTION AND COHERENT ROTATIONAL RAMAN SPECTROSCOPY

INTRODUCTION

As the first example of non-polar molecules studied in this thesis, we will examine dicyanoacetylene, N≡C-C≡C-C≡N, an unusual linear molecule first reported by Moureu and Bongrand in 1909[26].Dicyanoacetylene is a photoreactive species which readily undergoes polymerization and hence its possible use as a precursor for polyacetylenes is of interest[27]. The vibrational spectrum of C_4N_2 has also been reexamined recently[28], stimulated by the detection of similar nitriles in the thermal emission spectrum of the atmosphere of Titan, one of the moons of Saturn[29]. This has led to the postulate that a 478 cm^{-1} peak in the infrared emission spectrum recorded by the Voyager space probe is due to the presence of dicyanoacetylene[28].

The first vibrational analysis of C_4N_2 was reported in 1953 by Miller and Hannan[30]. Based on Raman spectra of the liquid phase and infrared spectra of the vapor phase, peak frequency assignments were made for eight of the nine fundamental vibrational modes. The assignments were later revised and the last mode identified by Miller *et al.*[31] in 1955. In 1987, Khanna *et al.* reported the

Raman and infrared spectra for solid C_4N_2 as well as the liquid phase Raman and vapor phase infrared spectra[28]. Revised assignments were given for the symmetric stretching fundamental frequencies and a new set of valence force constants based on these assignments was offered.

The structure of C_4N_2 is of some interest because of its unusual linear arrangement of three alternate triple bonds and because the molecule is simple enough to permit theoretical calculations of its properties. From x-ray crystallography, the C_4N_2 crystal belongs to the monoclinic space group $C_{2h}{}^5$-$P2_1a$ with bond lengths found to be $r_{C\equiv N}$ = 1.14 Å, r_{C-C} = 1.37 Å, and $r_{C\equiv C}$ = 1.19 Å[32]. The structure in the vapor phase has not been determined. No high resolution vibrational-rotational data have been recorded and, due to the centro-symmetric nature of C_4N_2, no microwave spectrum can be observed. The pure rotational spectrum is accessible by Raman methods, however, and we report here the high resolution Raman loss spectrum of C_4N_2. These data have been analyzed to obtain a B_{av} rotational constant which is the average for several low-lying bending states. In addition, band shape calculations were done in an effort to define a range for the vibration-rotation constant α for these excited states.

In collaboration with Dr. Kenneth Hedberg and Dr. Lise Hedberg, an electron diffraction experiment was carried out in order to obtain thermally-averaged interatomic distances (r_a, r_g) and vibrational amplitudes (ℓ) for the molecule. Quantities for the conversion of these distance types to ground vibrational state $r_\alpha{}^0$ values were calculated from a harmonic force field and the resultant geometry leads to a B_0 rotational constant that is slightly larger than

expected, given the value deduced from the Raman data. To explore one possible explanation of this discrepancy, simple *ab initio* calculations have been done to examine the importance of bond length changes as the molecule is bent.

EXPERIMENTAL

The dicyanoacetylene used in this work was prepared in a manner similar to the one described by Moureu and Bongrand[33]. Acetylene dicarboxamide, sand, and P_2O_5 were thoroughly mixed by grinding and placed in a 500 ml round bottom flask. This was then connected to a vacuum system which was subsequently evacuated to ~40 mTorr. The vessel was immersed in a 220°C oil bath. White crystals of dicyanoacetylene soon formed in a collection tube held at liquid nitrogen temperature. Upon completion of the reaction, the collection tube was warmed to dry-ice temperature and pumped to remove the CO_2 generated during the reaction. The sample was then warmed to room temperature and left in contact with P_2O_5 for two hours to remove water vapor. Due to the low reaction efficiency, (<10%), isotopic substitution was not considered practical.

To ascertain the quality of the sample, a vapor-phase infrared spectrum was taken on a Mattson Instruments Sirius 100 FTIR spectrometer at 0.125 cm^{-1} resolution. The locations of the peaks were consistent with those noted by previous researchers[28,31] and spectral features arising from possible sample impurities were minimal.

The electron diffraction data were obtained on the Oregon State apparatus.

Due to the limited supply of sample, only two plates were obtained, both at a nozzle-to-plate distance of ~300 mm (middle camera). The nozzle tip was maintained at room temperature and the sample container at ~0°C. Exposure time was two minutes for each plate, with beam currents of 0.47 μA and ambient pressures in the diffraction chamber of 2-5 x 10^{-6} Torr. The 8x10 inch Kodak projector slide plates were developed in D19 developer solution diluted 1:1.

The Raman studies were performed using the coherent Raman Loss apparatus at Oregon State University[34]. The spectral resolution of this system is about 0.003 cm^{-1} with a wavenumber accuracy of 0.007 cm^{-1}. The sample cell was at room temperature which resulted in a vapor pressure of ~50 Torr. Due to the photosensitive nature of C_4N_2, a polymer-like product began to form as a brown fog in the sample cell after a few minutes into a scan, thus degrading the strength of the signal. As a result, a spectrum showing a total intensity profile of the S-branch was not possible. Nevertheless, several short spectral regions were recorded at various shifts and at data intervals ranging from 0.002 to 0.01 cm^{-1}. A composite which covers a wide range of rotational transitions is shown in Figure 2.1.

RESULTS AND ANALYSIS

Electron diffraction

The procedures involved in obtaining the raw data, reducing the data to obtain the total scattered intensities $s^4I_t(s)$, and removing the background to yield the molecular intensities $sI_m(s)$ have been described previously[35,36]. The total intensity curves with backgrounds are shown at the top of Figure 2.2. The unusual slope of the total intensity curve of the second plate is probably a consequence of the poor alignment arising from near exhaustion of the sample.

The interatomic distances most directly derived from the electron diffraction data are denoted by r_a. These distances are related to the thermal average of the instantaneous internuclear distances r_g by

$$r_g = r_a + \ell^2/r_a \tag{2.1}$$

where ℓ^2 is the mean-square amplitude of vibration. For comparison with spectroscopic ground state rotational constants, harmonic corrections are applied via the relations

$$r_\alpha^0 = r_z = r_a^T - (3/2)a[(\ell^2)^T - (\ell^2)^0] - \delta r^T - K^0 + (\ell^2)^T/r_\alpha \tag{2.2}$$

$$B_0 - B_z = -\sum_{i}^{3N-6} \alpha_i(har)/2 \qquad (2.3)$$

where superscripts denote temperatures. The Morse anharmonicity parameter, a, is taken to be that of the corresponding diatomic molecule for the bonded distances and zero for the non-bonded distances. The mean-square amplitudes, ℓ^2, centrifugal distortions, δr, perpendicular amplitude corrections, K, and harmonic vibration corrections, α^{har}, are calculated from quadratic force constants in the usual fashion[37].

The choice of an appropriate force field was examined since there exist two different frequency assignments for the totally symmetric stretching modes of C_4N_2[28,31]. For each assignment, harmonic force constants were derived using the Schactschneider FPERT program[38]. A purely diagonal force field proved insufficient to fit the frequencies exactly and inclusion of a significant C≡N•••C≡N interaction constant was found necessary. Thus coupling of the "isolated" C≡N end bonds via the pi-electron network system appears to be important in C_4N_2.

Since no isotopic frequency data is available for C_4N_2, all other off-diagonal force constants were set equal to zero. The possible use of the experimental electron-diffraction amplitudes of vibration as added force-field constraints was explored. The different sets of force constants corresponding to the two alternative frequency assignments[28,31] were used in the program ASYM20[36] to generate values of ℓ^2, K, δr, and α. It was found that these quantities were not significantly different for the two sets of force constants, and thus, that force fields derived from

either frequency assignment gave adequate correction terms for the least squares fit of the electron-diffraction intensity data.

Two models were used in the refinement of the diffraction data. In Model A the molecule was explicitly constrained to a linear geometry and the geometrical parameters subject to refinement were taken to be the three non-equivalent bond lengths. Eight amplitudes of vibration were also refined. The nearly equal C≡C and C≡N amplitudes were refined as a pair with maintenance of their difference at a value calculated from the force field. The results of this analysis are given in Tables 2.1 and 2.2 and in the radial distribution curve shown in Figure 2.3.

In C_4N_2, vibrational averaging effects are expected to be significant: in particular, the two low frequency bending modes, (ν_7 = 263 cm^{-1}, ν_9 = 107 cm^{-1}), could lead to appreciable "shrinkage effects" in which the measured values for the nonbonded distances are somewhat smaller than the sum of the relevant bond lengths. To determine shrinkage values, δ_g, a second refinement, Model B, was done in which all nine atom-atom distances were treated as independent variables, along with the same treatment of amplitudes as for Model A. The thermally-averaged distances and amplitudes obtained in this case are also given in Table 2.1 and the shrinkage effect values are presented in Table 2.3, along with values for similar molecules.

Raman Frequency Analysis

At room temperature, less than 10% of the molecules are in the ground vibrational state and several of the low-lying excited bending states of C_4N_2 are significantly populated, as shown in Table 2.4. As a result, the observed pure rotational Raman spectrum is a complicated average over many vibrational states. For C_4N_2, the rotational constant B_v is given by

$$B_v = B_e - \sum_i^9 \alpha_i (v_i + 1/2 d_i) \tag{2.4}$$

where v stands for the set of vibrational quantum numbers $v_i ... v_9$ and α_i and d_i are respectively the vibration-rotation interaction constant and the degree of degeneracy of the i^{th} vibrational mode. The rotational energy levels are given by

$$F_{vJ} = B_v[J(J+1) - \ell^2] - D_{vJ}[J(J+1) - \ell^2]^2 \tag{2.5}$$

where D_{vJ} is the centrifugal distortion constant and the symbol ℓ used here is the quantum number characterizing the angular momentum about the internuclear axis.

The frequencies of the allowed S-branch ($\Delta J = +2$) rotational transitions are given by

$$S(J) = (4B_v - 6D_{vJ})(J + 3/2) - 8D_{vJ}[(J + 3/2)^3 - \ell^2(J + 3/2)] \tag{2.6}$$

For non-degenerate Σ levels, $\ell = 0$, and the J even/odd S-branch lines will have a 2/1 intensity ratio due to the nuclear spin of nitrogen. This alternation will be

obscured by overlapping S-branch transitions from degenerate vibrational states with $\ell > 0$ since, for these, unresolved $\pm \ell$ components will have opposite nuclear spin weights. The exact degeneracy of these $\pm \ell$ levels is lost since the energy of the molecule depends upon whether the bending is with, or opposed to, the direction of rotation. This results in a splitting of $\Delta\nu = qJ(J+1)$ in each rotational level, where $q \sim 10^{-3}$ to 10^{-4} cm^{-1} [39] is the ℓ-type doubling constants. In general, the $+\ell$ and $-\ell$ levels give rise to somewhat different values of B and D_J.

For the $\ell > 0$ levels, R-branch ($\Delta J = +1$) rotational transitions are also allowed, although the intensity of these falls off very quickly, as 1/J. For example, even at the first line seen in our spectra, S(12), the overlapping R(26) feature contributes only about 1% to the intensity; hence only S-branch lines are considered in our analysis.

Although the instrumental resolution is high and the collisional broadening at 50 Torr is estimated to be only ~ 0.04 cm^{-1} for C_4N_2, the plethora of thermally populated states results in only partially resolved structure in the rotational spectrum. This is a consequence of the fact that the two lowest frequency bends occur at 263 cm^{-1} (ν_7) and 107 cm^{-1} (ν_9). Table 2.4 shows that the 15 lowest levels, involving mainly overtone/combinations of ν_7 and ν_9, account for 2/3 of the total population. The state degeneracy of each excited level is also given. Given such a variety of B values, it is perhaps surprising that the rotational spectrum is as resolved as it is over the large range of J values observed.

To extract a rotational constant representing the average over the many vibrational states, each feature in each of several recorded spectra was subjected to

an eleven-point parabolic fitting operation to find the best peak frequency. These frequencies were then fit to Eq. 6, with neglect of the small ℓ^2 term, to yield values of B_{av}, D_{av}, and a small constant ($\sim\pm0.02$ cm^{-1}) representing the calibration error in the Raman loss apparatus for that particular day. After shifting each data set by these calibration constants, all of the data were combined and the process repeated to obtain a B_{av} of 0.044867(19) cm^{-1} and D_{av} of 9.3(6) x 10^{-9} cm^{-1}. The resultant corrected frequencies and differences (obs'd - calc'd) are given in Table 2.5.

Raman Bandshape Analysis

Examination of the expanded Raman loss spectra show hints of some regular but poorly-resolved structure within each J transition, as illustrated in the top spectra of Figure 2.4. An attempt was made to extract more information from these data using a simple model to simulate the spectrum. This was done by calculating the frequencies and intensities of the rotational transitions arising from the ground state and all states in Table 2.4 involving the ν_7 and ν_9 modes only. The energy levels were assumed to fit the expression

$$F(J) = [B_0 - \alpha(\nu_7 + \nu_9)][J(J+1) - (\ell_7 + \ell_9)^2] - D[J(J+1) - (\ell_7 + \ell_9)^2]^2 \qquad (2.7)$$

i.e., it was assumed that a single value of the vibration-rotation constant α applied for all states involving ν_7 and ν_9. These transitions were then summed using the appropriate degeneracies and Boltzmann weights, the Raman line-strength factors, and a Lorentzian line shape of 0.04 cm^{-1} to account for collisional broadening.

For each J transition, this model predicts five significant lines, corresponding

to $v_7 + v_9$ values of 0 to 4. These lines are evenly spaced by $4\alpha J$, with the maximum intensity occurring at about $v_7 + v_9 = 2$. Thus one might expect that $B_{av} \approx B_0 - 2\alpha$. The constant α is expected to be negative for states involving the bending modes since the end-to-end atom distances are less for a bent geometry. Typically α_{bend}/B is -0.001 to -0.004 for linear molecules[40], and such a range was explored for C_4N_2. Figure 2.4 shows the contours calculated for low and high J transitions for several values of α. Because of the assumption that $B_0 = B_{av} + 2\alpha$, the center of each transition set is well matched to the experimental peak average but it is clear that the peak modulation depth is changed greatly as α varies. At high J values, the five line multiplets spread and start to overlap in a constructive or destructive fashion, producing a higher or lower apparent frequency modulation in the calculated spectrum. Such interference may account for the reduced modulation seen for Raman shifts greater than 16 cm^{-1} where $J > 90$.

In view of the simplified nature of the model, it is not surprising that it was not possible to produce a very satisfactory match simultaneously for low and high J values. However, it does appear that an average negative α value of about -0.0002(1) gives the best overall fit to the spectrum and hence B_0 is about 0.0445(1) cm^{-1}. Because this value is not very well-determined, it was not used as a constraint in a combined electron diffraction - spectroscopy least squares structural determination, one of our original intents.

DISCUSSION

Bond Lengths

The r_α^0 bond lengths obtained from the refinement of the electron-diffraction data are listed in Table 2.6 along with some r_0 distances for similar compounds. Comparison of the bond lengths of C_4N_2 in the gas and solid phases suggests that condensation produces a small contraction of the triple bonds and an expansion of the C-C single bonds. This is somewhat surprising since packing forces in the solid should preferentially compress the weaker C-C bonds, while any long range delocalization of the pi electrons would be expected to result in longer triple bonds in the solid. It may be, however, that these small differences are spurious since no uncertainties were given in the x-ray studies.

As can be seen in Table 2.6, molecules with alternate single and triple bonds have a C-C distance of ~1.37 Å, a remarkably short value approaching the C=C distance of 1.339 Å in ethylene rather than the C-C value of 1.536 Å in ethane. This suggests that ionic resonance structures such as $^-N{=}C{=}C{=}C{=}N^+$ may be important in the bonding description. The increased charge separation possible in $N{\equiv}C{-}C{\equiv}C{-}C{\equiv}N$ compared to $N{\equiv}C{-}C{\equiv}N$ should favor such forms and this could account for the slightly smaller C-C distance in the former molecule. The difficulty with this simple picture, however, is that it predicts a corresponding increase in the $C{\equiv}N$ and $C{\equiv}C$ distances relative to those in HCN and C_2H_2 whereas the experimental values are essentially constant. The simple valence bond description is thus not a good model for these compounds and a molecular orbital approach is

to be preferred.

We have carried out an *ab initio* calculation (Gaussian 86 at the HF/6-31G* basis level[41]) which gives an energy level pattern and an orbital description close to that predicted by a simple Huckel model. The net charge distribution corresponds to $^{-\delta}N{=}C^{+\delta}{-}C{\equiv}C{-}^{+\delta}C{=}N^{-\delta}$ with δ = 0.45 electrons and the central C≡C atoms essentially neutral as in C_2H_2. The predicted r_e bond lengths, shown in Table 2.6, are sensibly shorter than the experimental r_o values. This offers some encouragement that other physical properties such as vibrational frequencies and transition intensities may also be reliably estimated from these calculations. In particular, the three calculated unscaled Σ_g^+ symmetric stretching vibrational frequencies and Raman activities (in brackets) can be compared with the assignments of Khanna *et al.*[28] and Miller *et al.*[31]:

Mode	Calculated	Khanna	Miller
ν_1 (C≡N)	2706 [1300]	2271 [vs]	2290 [vs]
ν_2 (C≡C)	2455 [1.3]	2327 [vs]	2119 [m]
ν_3 (C-C)	640 [1]	640 [vw]	692 [m]

Close absolute agreement is not to be expected but it may be meaningful that the calculated frequency ordering and relative intensity patterns are more consistent with Miller's assignment. This ordering of the C≡N and C≡C stretching frequencies is also in line with the bond length ordering found experimentally. These two stretching modes are undoubtedly heavily mixed, however, and further study using isotopic substitution will probably be necessary to provide a definitive choice among the two assignments.

Rotational Constants

The B_0 rotational constant derived from the electron-diffraction bond lengths is 0.04489(9) cm^{-1}, nearly identical to the B_{av} value of 0.04487(2) deduced from the Raman data. This is somewhat surprising since, as discussed earlier, the contribution of excited bending states should be such as to make $B_{av} > B_0$ by perhaps 0.0002 cm^{-1}. It is, of course, possible that the harmonic corrections used to obtain B_0 from the r_a values of the diffraction analysis are insufficient. In the case of C_3O_2, a molecule with an exceptionally low bending mode at 17 cm^{-1}, an analogous discrepancy between electron diffraction - spectroscopic rotational constants was resolved only by explicit inclusion of anharmonic terms involving this mode.[42] This "quasi-linear" molecule is quite unusual in that it is thought to have a barrier of 27(16) cm^{-1} at the linear geometry, the minimum occurring for a central bend angle of 20(2) degrees. A clear indication of the inadequacy of the harmonic corrections for "linear" C_3O_2 is given by the poor agreement between calculated and observed shrinkage effects in Table 2.3. In contrast, the agreement for C_4N_2 is comparable to that seen for other linear molecules. Similarly, the comparison of calculated and observed mean square amplitudes shown in Table 2.1 indicates that the harmonic force field is acceptable for C_4N_2.

The equality of B_{av} and B_0 implies a distribution of excited state B values centered about B_0. Smaller B values could come from excited states involving axial stretching modes but these have a much lower thermal population than the bending levels. If however, the bond lengths should increase appreciably as the molecule is

bent, a net decrease in the B value might result. In fact, such a stretch-bend interaction has been observed for C_3O_2, the C=C bond lengths extending slightly as the molecule bends[42]. A similar, but smaller, effect has also been noted for other linear geometries such as CO_2[43], CS_2[44], and $CH_2=C=CH_2$[45].

To examine this possibility for C_4N_2, our *ab initio* calculations at the 6-31G* level were extended by optimization of the structure for fixed and bent conformations. Bond angles of 174.7° (C≡C-C) and 177.8° (C-C≡N) were chosen since these correspond to mean bending amplitudes (thermally averaged) obtained from the force field analysis for the 107 cm^{-1} bending mode. The effect of bending was quite small: an increase of 0.0004 Å in the C≡C distance and a decrease of 0.0001 Å in the C≡N and C-C distances. Such changes are insufficient to account for the discrepancies in the B_0 rotational constants. Calculations with a larger basis set and electron correlation might change this conclusion of course.

One final possible cause of low B values for excited bending states is intriguing, albeit highly speculative: that C_4N_2, like C_3O_2, is quasi-linear with an appreciable barrier at the linear geometry. Bending states above the barrier would then be linear and thus have B values smaller than B_0. It should be said that the electron diffraction shrinkage data do not support such an unusual structure however and it should also be noted that our theoretical calculations converged at the linear geometry. Thus a resolution of the small difference between the electron diffraction and spectroscopic B_0 values does not seem possible with the data in hand. Further high-resolution Raman and infrared examination of the bending modes and their overtones would be desirable for C_4N_2 since these would better

establish the bending potential function and give more accurate B values of the bending states.

ACKNOWLEDGEMENTS

Special thanks go to Rainer Beck for assistance in obtaining the Raman Loss spectra.

Table 2.1: Distances and Amplitudes for Dicyanoacetylene[a]

	A. Constrained linear model					B. Unconstrained model		
	r_α^0	r_g	r_a	$\ell_{obsd.}$	$\ell_{calcd.}$	r_g	r_a	$\ell_{obsd.}$
N_1-C_2	1.161(5)	1.169	1.167	0.047(4)	0.040	1.163(3)	1.161	0.041(6)
C_3-C_4	1.198(11)	1.205	1.203	0.048(4)	0.042	1.230(16)	1.228	0.041(6)
C_2-C_3	1.367(3)	1.373	1.371	0.049(3)	0.045	1.376(4)	1.374	0.049(3)
N_1•C_3	2.528(6)	2.535	2.534	0.060(9)	0.052	2.527(49)	2.526	0.055(31)
C_2•C_4	2.566(11)	2.570	2.568	0.057(7)	0.051	2.580(60)	2.579	0.054(34)
N_1•C_4	3.727(7)	3.731	3.730	0.063(7)	0.055	3.730(10)	3.728	0.065(3)
C_2•C_5	3.933(11)	3.935	3.934	0.066(18)	0.058	3.949(23)	3.948	0.064(6)
N_1•C_5	5.094(8)	5.096	5.095	0.066(10)	0.058	5.094(14)	5.093	0.067(3)
N_1•N_6	6.255(8)	6.256	6.255	0.080(27)	0.066	6.239(36)	6.238	0.078(9)

[a]All values in Å. In Model A, all non-bonded distances were constrained to be sums of bonded distances so as to produce a linear structure. In Model B, each distance was treated as an independent variable to permit determination of the shrinkage effects given in Table 2.3. Uncertainties in parentheses are 2σ and include estimates of systematic error. Uncertainties are assumed to be equal for each set of r_α^0, r_g, and r_a values.

Table 2.2: Correlation Matrix (x100) for Dicyanoacetylene

	σ^a	r_1	r_2	r_3	ℓ_1	ℓ_2	ℓ_3	ℓ_4	ℓ_5	ℓ_6	ℓ_7	ℓ_8
r(C≡N)	0.16	100										
r(C≡C)	0.79	-92	100									
r(C-C)	0.17	34	-41	100								
$\ell(N_1 \cdot C_2)$	0.13	80	-82	50	100							
$\ell(C_2 \cdot C_3)$	0.09	-30	17	-9	-18	100						
$\ell(N_1 \cdot C_3)$	0.30	62	-69	<1	58	6	100					
$\ell(C_2 \cdot C_4)$	0.25	-1	9	40	14	1	-50	100				
$\ell(N_1 \cdot C_4)$	0.23	-10	11	3	<1	5	-5	8	100			
$\ell(C_2 \cdot C_5)$	0.62	23	-27	3	29	-3	23	-7	-10	100		
$\ell(N_1 \cdot C_5)$	0.34	14	-14	3	8	4	3	5	4	<1	100	
$\ell(N_1 \cdot N_6)$	0.96	2	-1	1	4	<1	2	2	1	<1	<1	100

[a]Standard deviation (x100) from least-squares refinement. Distances (r) and amplitudes (ℓ) in Å.

Table 2.3: Comparison of shrinkage effects

	δ_g (Å) obs.	δ_g (Å) calc.
N≡C-C≡C-C≡N[a]		
C•N	0.012 ±0.017	0.0096
C•C	0.026 ±0.022	0.0148
C••N	0.039 ±0.007	0.0288
C••C	0.033 ±0.010	0.0324
C•••N	0.050 ±0.007	0.0507
N••••N	0.068 ±0.014	0.0728
H-C≡C-C≡C-H[b]		
C•H	0.033 ±0.03	0.020
C•C	0.014 ±0.002	0.011
C••H	0.064 ±0.03	0.035
C••C	0.030 ±0.006	0.027
C•••H	0.076 ±0.03	0.054
N≡C-C≡N[c]		
C•N	0.0126 ±0.0045	0.011
N••N	0.0226 ±0.0068	0.024
O=C=C=C=O[d]		
O•C	0.006 ±0.0015	0.0067
C•C	0.08 ±0.05	0.991
O••C	0.109 ±0.009	1.303
O•••O	0.156 ±0.019	1.894

[a]This work. δ_g values for C_4N_2 were derived from the r_g values of model B in Table 2.1, with the uncertainties calculated from 1σ for each r_g value. [b]Ref. 46. [c]δ_g obs. from ref. 47 and δ_g calc. from ref. 48. [d]δ_g obs. from ref. 42 and δ_g calc. from a harmonic force field fit to the vibrational frequencies reported in ref. 49 and ref. 50.

Table 2.4: Occupation of the 15 lowest vibrational levels of C_4N_2 at 293 K[a]

Level	Frequency (cm^{-1})	Degeneracy	Occupation Percent
GROUND	0	1	8.33
ν_9	107	2	9.75
$2\nu_9$	214	3	8.57
ν_7	263	2	4.47
$3\nu_9$	321	4	6.69
$\nu_7+\nu_9$	370	4	5.24
$4\nu_9$	428	5	4.90
ν_8	471	2	1.58
$\nu_7+2\nu_9$	477	6	4.60
ν_6	504	2	1.34
$2\nu_7$	526	3	1.80
$5\nu_9$	535	6	3.44
$\nu_8+\nu_9$	578	4	1.85
$\nu_7+3\nu_9$	584	8	3.59
$\nu_6+\nu_9$	611	4	1.57

[a]Levels are arranged in order of increasing frequency. The sum of the occupations in this table is 68% with the remaining 32% of all molecules lying in higher vibrational states. Frequencies and degeneracies are for strictly harmonic vibrations.

Table 2.5: Wavenumber shifts of S-branch transitions of C_4N_2

J	$\nu_{obs.}$[a]	$\nu_{obs.}$ - $\nu_{calc.}$	J	$\nu_{obs.}$	$\nu_{obs.}$ - $\nu_{calc.}$	J	$\nu_{obs.}$	$\nu_{obs.}$ - $\nu_{calc.}$
12	2.406	-0.017	47	8.715	-0.010	80	14.589	-0.010
13	2.554	-0.049	48	8.866	-0.012	81	14.770	-0.003
15	2.974	0.012	49	9.052	0.002	82	14.956	0.006
16	3.125	-0.016	50	9.230	-0.006	83	15.129	0.008
17	3.320	-0.000	51	9.418	0.005	84	15.309	0.010
18	3.513	0.013	52	9.579	-0.006	85	15.309	0.010
19	3.698	0.018	53	9.760	-0.004	86	15.670	0.015
20	3.862	0.003	54	9.948	-0.001	87	15.840	0.008
21	4.033	-0.005	55	10.124	-0.004	88	16.027	0.017
22	4.218	0.000	56	10.305	-0.007	89	16.182	-0.005
23	4.407	0.010	57	10.482	0.004	90	16.343	-0.022
24	4.579	0.002	58	10.659	-0.006	91	16.552	0.009
25	4.767	0.012	59	10.834	-0.004	92	16.744	0.024
26	4.940	0.005	60	11.018	-0.001	93	16.909	0.011
27	5.124	0.019	61	11.202	0.004	94	17.094	0.019
28	5.303	0.009	62	11.374	-0.009	95	17.271	0.018
29	5.481	0.006	63	11.550	0.001	96	17.434	0.004
30	5.657	0.004	64	11.730	-0.002	97	17.613	0.006
31	5.858	0.007	65	11.920	0.011	98	17.785	0.000
32	6.033	0.001	66	12.093	-0.008	99	17.978	0.016
33	6.213	-0.001	67	12.269	-0.008	100	18.148	0.008
34	6.394	0.007	68	12.444	-0.011	101	18.309	-0.007
35	6.575	0.013	69	12.627	-0.001	102	18.478	-0.016
36	6.756	0.006	70	12.811	-0.010	103	18.667	-0.004
37	6.935	0.012	71	12.981	-0.002	104	18.852	0.005
38	7.111	-0.002	72	13.158	-0.009	109	19.727	-0.005
39	7.285	-0.003	73	13.327	-0.013	110	19.924	0.016
40	7.465	-0.001	74	13.518	0.007	113	20.425	-0.013
41	7.648	-0.008	75	13.695	-0.010	114	20.622	0.007
42	7.820	0.003	76	13.872	-0.009	119	21.538	0.041
43	8.004	-0.004	77	14.056	-0.013	122	21.988	-0.037
44	8.182	-0.003	78	14.228	-0.006	123	22.157	-0.044
45	8.359	-0.003	79	14.410	-0.009	127	22.910	0.005
46	8.536	-0.012						

[a]Shifts determined by fit of each unresolved J-transition of Figure 2.1.

Table 2.6: Comparison of structural parameters

		r_0 bond lengths (Å)		
		$r_{C\equiv N}$	r_{C-C}	$r_{C\equiv C}$
N≡C-C≡C-C≡N	[a]gas, ED	1.161(5)	1.367	1.198
	[b]solid, x-ray	1.14	1.37	1.19
	[a]r_e, *ab init.*	1.136	1.389	1.186
H-C≡C-C≡C-H	[c]gas, Raman	-----	1.376(2)	1.205
H-C≡C-C≡N	[d]gas, MW	1.157(1)	1.382(1)	1.203(1)
N≡C-C≡N	[e]gas, IR	1.154(6)	1.389(10)	-----
H-C≡C-H	[f]gas, Raman	-----	-----	1.2086(1)
H-C≡N	[g]gas, IR	1.15313(2)	-----	-----

[a]This work. [b]Ref. 31. [c]Ref. 51. The C≡C distance was assumed. [d]Ref. 52. [e]Ref. 53. [f]Ref. 54. [g]Ref. 55.

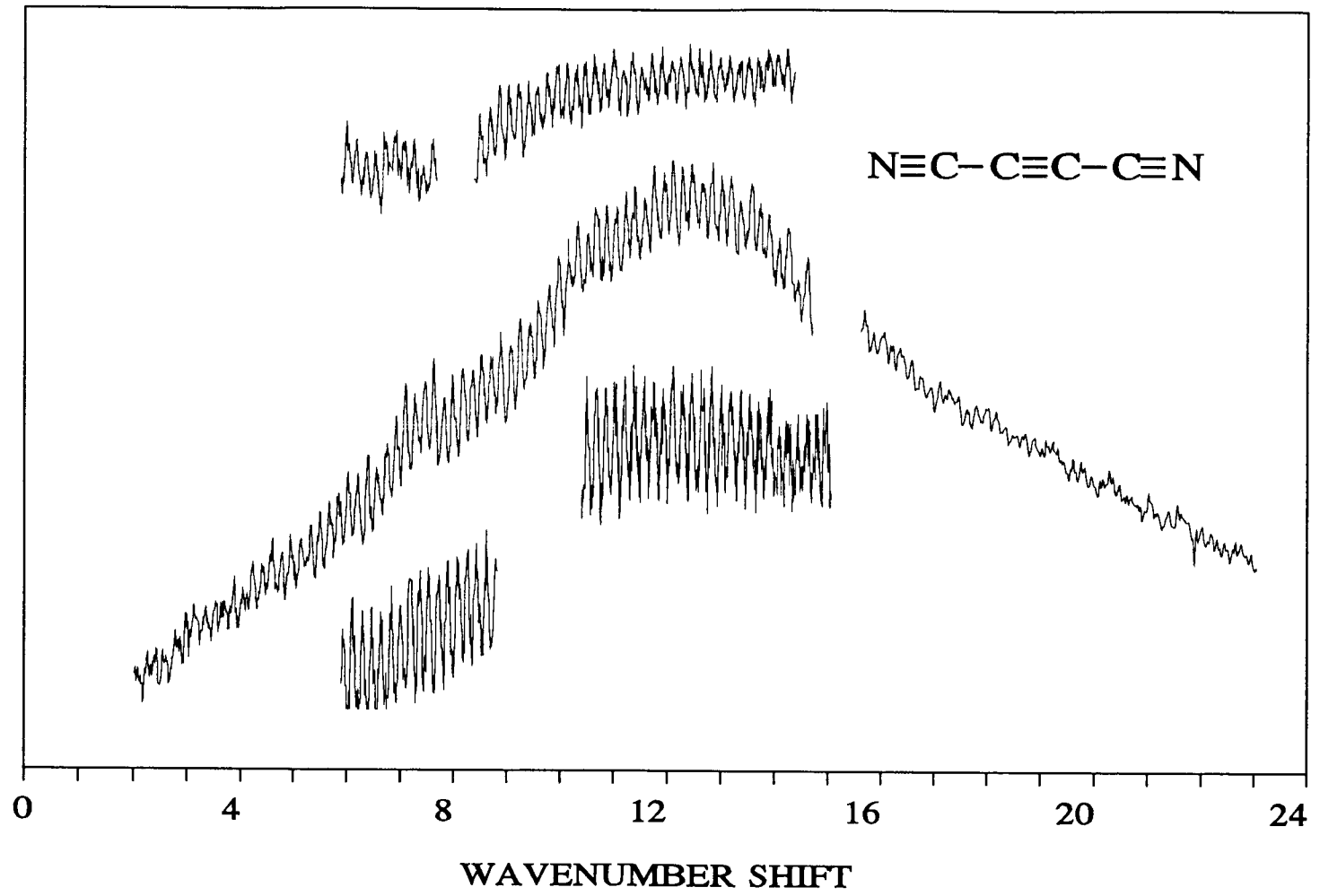

Figure 2.1: Pure rotational Raman Loss spectra of C_4N_2. The lower two segments were recorded at 0.007cm^{-1} data intervals and the remaining segments at 0.010 cm^{-1} intervals.

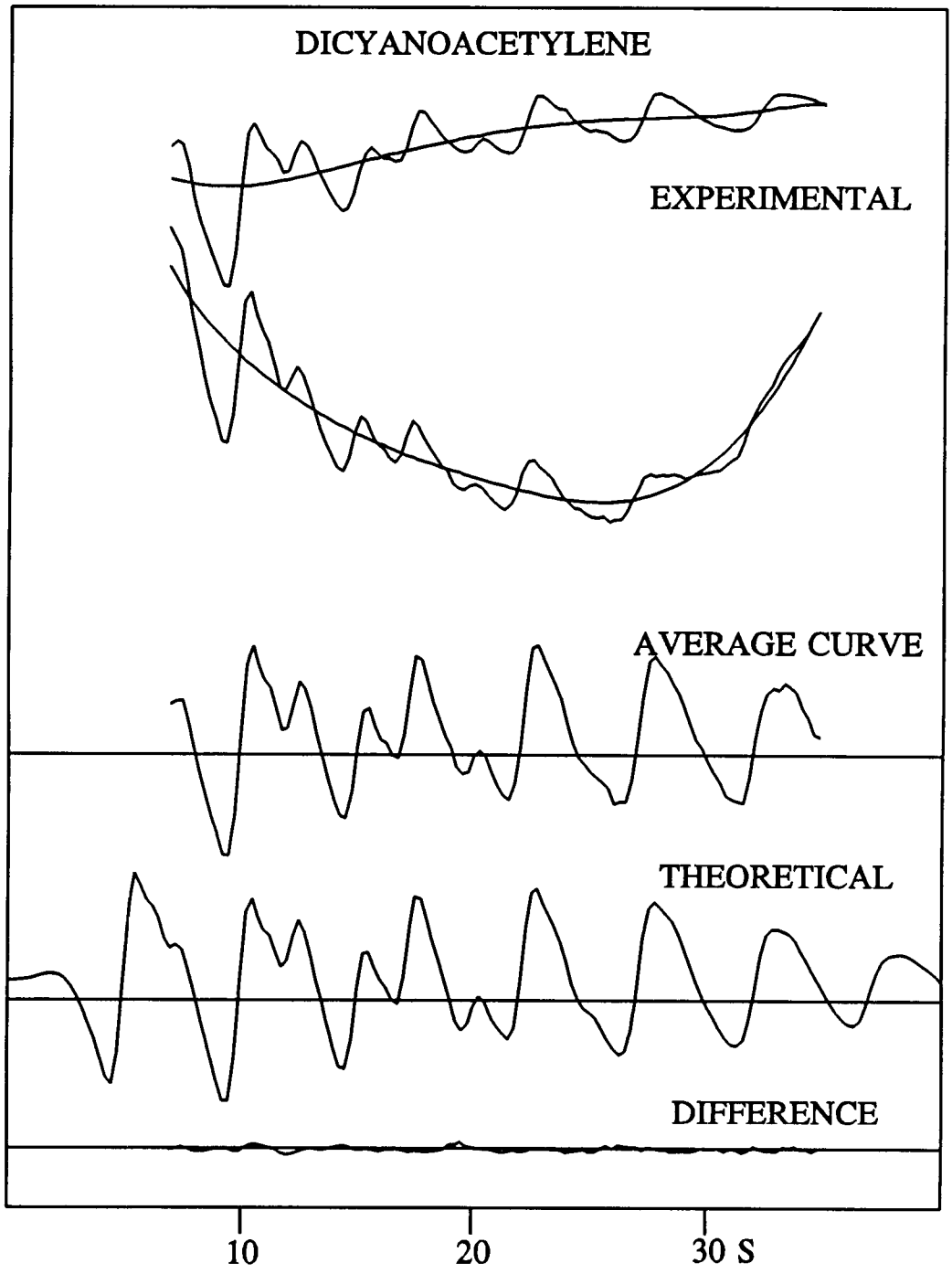

Figure 2.2: The $s^4I_t(s)$ electron diffraction intensity curves from each plate are shown superimposed on the final backgrounds and are magnified 3x relative to the backgrounds. Difference = experimental - theoretical.

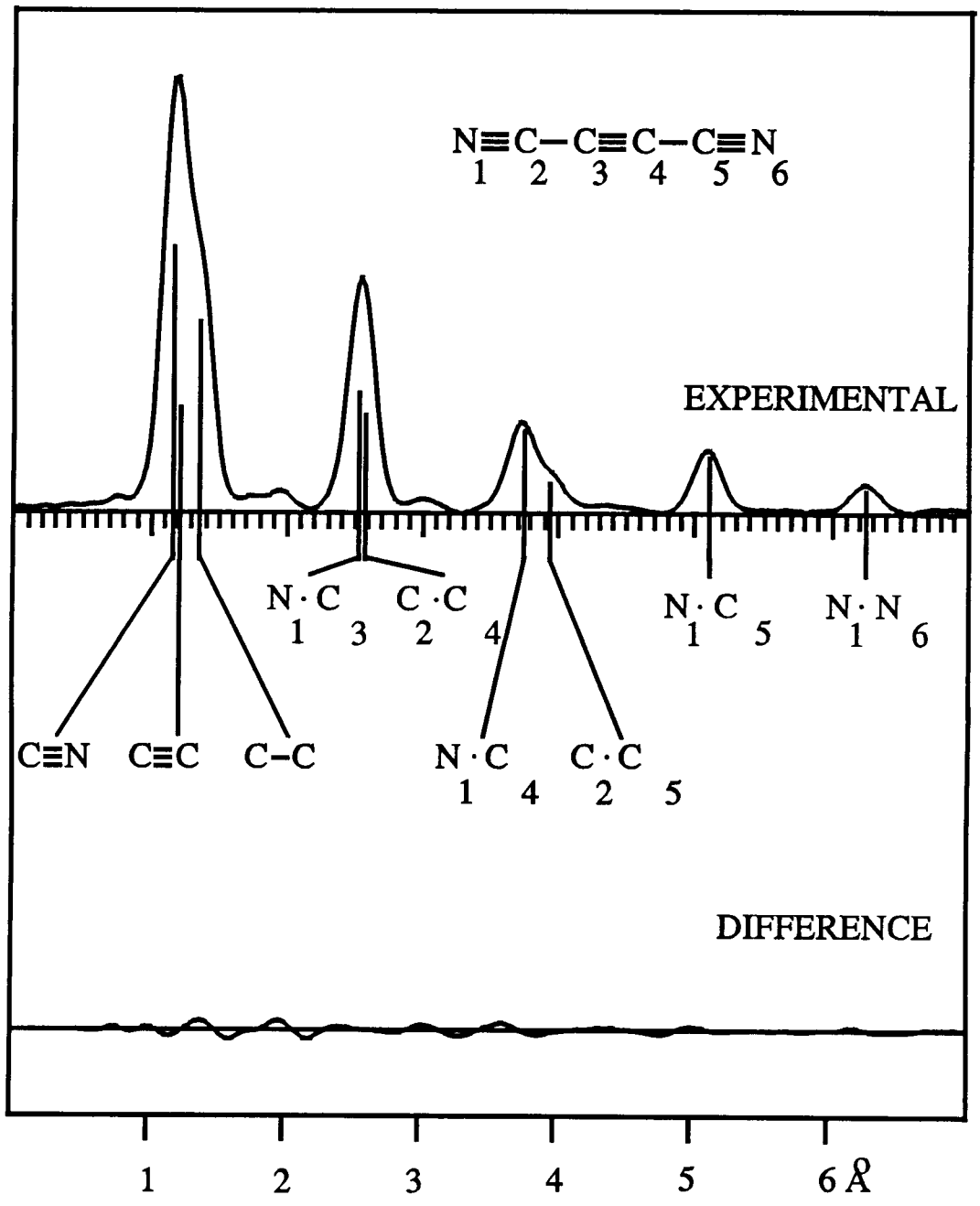

Figure 2.3: Experimental radial distribution curve derived from the average curve of Figure 2.2. The convergence factor B was equal to 0.0025Å^2. Difference = experimental - theoretical.

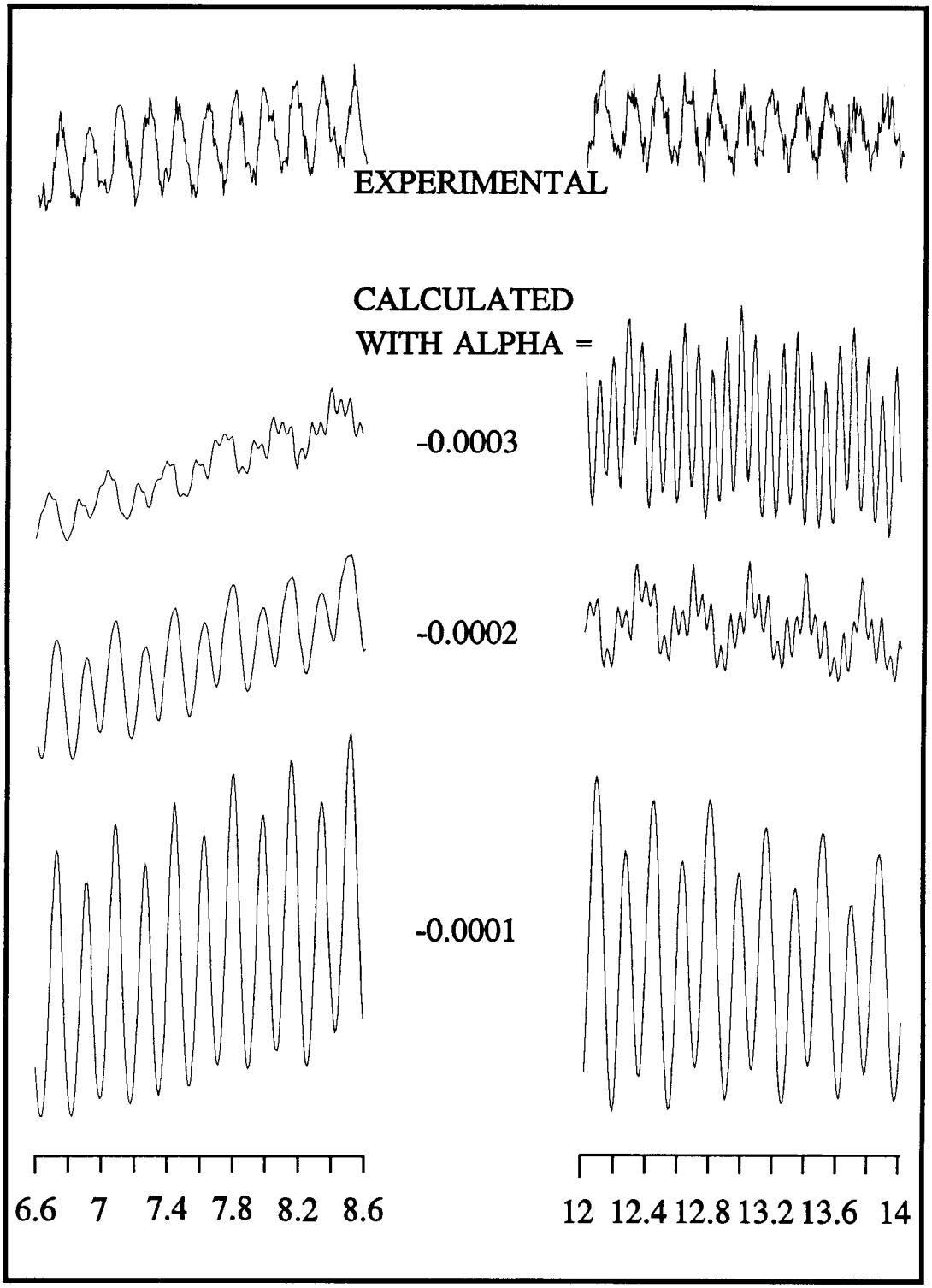

Figure 2.4: Experimental vs. calculated Raman Loss spectra of C_4N_2. Calculated spectra are based on a model involving a single value of the vibration-rotation interaction constant, α, for the low-lying bending levels.

CHAPTER 3 HIGH RESOLUTION ROTATIONAL CARS SPECTRUM OF OXYGEN

INTRODUCTION

The rotational Raman spectrum of oxygen is unusual in that each of the $\Delta N=2$ S branch transitions is split by electron spin couplings into three sets of transitions, $\Delta J=2$, $\Delta J=1$, and $\Delta J=0$ which are made up of three ^{S}S, two ^{S}R, and one ^{S}Q components respectively (see Figure 3.1). The strongest of these sets is the $\Delta N=2$, $\Delta J=2$ ^{S}S triplet but these have not been resolved by conventional Raman spectroscopy since the individual lines are closely spaced (0.02 cm^{-1} average peak-to-peak separation). The ^{S}S triplet can, however, be resolved using coherent Raman techniques and in this paper, we report the rotational transition frequencies of each individual ^{S}S line of oxygen from N=1-19, obtained for the first time using a low frequency high resolution CARS apparatus recently developed at Oregon State University. The extraction of accurate transition frequencies and intensities through lineshape modeling of the spectra is discussed and the results are compared to those calculated using parameters obtained from magnetic dipole microwave spectroscopy.

The initial rotational Raman spectra reported for oxygen by Rasetti[56] in 1930 using a prism spectrograph and the Hg 2537 Å exciting line showed only the overall $\Delta N=2$ bands. The two $\Delta J=1$ lines appear as satellites separated ~2 cm^{-1} from the $\Delta J=2$ band and were later resolved by Jammu *et al.* in 1966[57]. The

intensities of these satellites relative to the central line decrease very rapidly with N[58,59]. The $\Delta J=0$ line is very weak and is very near the $\Delta J=2$ triplet[60]. To our knowledge, the only reported experimental observation of resolved $\Delta N=2$, $\Delta J=2$ transitions was by Hill *et al.*[61] who showed two of the S(1) lines obtained by stimulated Raman spectroscopy in a discussion of optical Stark effects in O_2.

The frequencies and intensities of the various Raman lines can be calculated from molecular parameters obtained from microwave spectroscopy, using an effective Hamiltonian appropriate to a coupling scheme intermediate between Hund's cases (a) and (b)[62]:

$$H_{rot} = B(J-S)^2 + 2\lambda(S_z^2-S^2) + \gamma(J-S)\cdot S \qquad (3.1)$$

The first term is the usual rotational part and the others represent spin-spin and spin-rotation interactions. γ is the coupling constant between the electron spin and the end-over-end rotation and S_z is the component of **S** along the internuclear axis. The constant λ was derived by Kramers[63] who showed that the interaction of the two unpaired electron spins, when averaged over the rotation of the molecule, is equivalent to a coupling between the total spin and the spin component along the figure axis and is proportional to $3\cos^2\theta - 1$, where θ is the angle between **S** and S_z. Its inclusion in the Hamiltonian results in a slight mixing of $N\pm1$ states, corresponding to a coupling case intermediate between Hund's case (a) and (b). The Hamiltonian in Eq. 3.1 can be solved to yield the three term values, $F_1(N)$, $F_2(N)$, and $F_3(N)$ which correspond to $J = N+1$, $J = N$, and $J = N-1$, respectively[64]:

From the term values, one may readily calculate the Raman shifts and

$$F_1(N) = F_2(N) + B_0(2N+3) - \lambda - \tfrac{1}{2}\gamma - [\lambda^2 - 2\lambda(B_0 - \tfrac{1}{2}\gamma) + (2N+3)^2(B_0 - \tfrac{1}{2}\gamma)^2]^{\frac{1}{2}},$$
$$F_2(N) = B_0N(N+1) - D_0N^2(N+1)^2, \qquad (3.2)$$
$$F_3(N) = F_2(N) - B_0(2N-1) - \lambda - \tfrac{1}{2}\gamma + [\lambda^2 - 2\lambda(B_0 - \tfrac{1}{2}\gamma) + (2N-1)^2(B_0 - \tfrac{1}{2}\gamma)^2]^{\frac{1}{2}}.$$

intensities of each rotational line as has been done by Altmann *et al.*[60] (1972) and by Berard *et al.*[65] (1983). Their transition frequencies are in close accord with the values listed in Table 3.1, which we have calculated from the microwave constants suggested by Johns and Lepard[66].

EXPERIMENTAL

The high resolution CARS apparatus used in this experiment (see Figure 3.2) is a recent version which permits both vibrational and pure rotational spectroscopy with only small modifications. In the pure rotational configuration used for this study, the 568.2 nm line of a single-mode Kr^+ ion laser (Coherent 90-K) is directed through an amplifier chain consisting of three R6G containing dye cells pumped by the 532 nm output of a seeded, single-frequency Nd:YAG laser (Quanta Ray DCR-1A). An identical amplifier chain is used to pump the tunable output of a cw single-mode ring dye laser (Coherent 699-29) that has been optimized to operate in a range overlapping the 568.2 nm Kr^+ line. It is these two beams that drive the rotational transition while the 532 nm Nd:YAG beam is used as the probe source in the CARS process. The signal beam near 532 nm passes through a shielded tunnel into a 1/3 m monochromator and is detected by a Hamamatsu R955 photomultiplier tube whose output is directed into a SRS Model SR250 gated integrator. This signal is averaged over 8-16 shots by a microcomputer and is stored

for analysis.

Discrimination of the very weak signal from the intense pump beams has always been a significant difficulty in rotational Raman spectroscopy. Several methods have been used in this experiment to overcome this obstacle. First, by using two yellow beams and one green beam rather than three green sources as is usually done in rotational CARS, we can effectively discriminate against any yellow light with the monochromator. This leaves only the background scatter from the green probe to contend with. Second, the three input laser beams are arranged in the folded BOXCARS configuration[4] to allow for spatial filtering of the signal beam from the three input beams. Even with these two techniques, an appreciable amount of 532 nm light scattered by the sample and optics tracks the same path as the signal beam. This background light still dominates the spectrum near zero shift but was greatly reduced by using a scheme wherein the polarizations of the Kr^+ and the 532 nm beams were rotated 90° with respect to the tunable dye and signal beams. A Glan polarizer was then inserted between the sample cell and the monochromator to reject light having the same polarization as the 532 nm beam. This setup reduced the background at zero Raman shift by a factor of four. This was decreased another factor of ten by improving the linear polarization of the green beam with a Glan-Thompson polarizer inserted in the 532 nm input beam just before the cell.

Finally, by adjusting the temperature of the Nd:YAG crystal in the seed laser, a single mode within the Nd:YAG gain profile was chosen whose doubled frequency coincides with an iodine absorption line. Then, a 20 cm I_2 cell was

placed in the signal beam path so that any residual 532 nm photons were absorbed. This narrow "notch filter" reduced the signal due to the Nd:YAG photons by another factor of twenty. Of course, when the Raman transition frequency matches that of an iodine absorption, the signal beam is also absorbed. This "hole" in the spectrum can be recognized however, by scanning through the same transition on the opposite side of zero shift, since the likelihood of an I_2 absorption occluding both signal peaks is small. Together, all of these schemes reduced the noise due to the Nd:YAG light at zero Raman shift by a factor of 800; effectively giving a zero background level for pure rotational CARS studies.

The experimental Raman shifts reported in Table 3.1 were obtained after calibration by sending a portion of the ring dye laser beam through an I_2 cell to a photodiode whose signal was collected simultaneously with the data. The I_2 frequencies were taken from the I_2 atlas[67]. The Kr^+ line position was determined by scanning through rotational lines on both sides of the Kr^+ line and calculating the midpoint between transitions with identical J,N values.

The oxygen in this experiment was contained in a 10 cm glass cell filled to 70 Torr. To obtain a good spectrum of the S(1) line, however, it was necessary to increase its intensity by cooling the sample in a free jet expansion. The nozzle, a modified Bosch fuel injector valve with a 0.2 mm orifice, was operated at room temperature and with a reservoir pressure of 4 atm, yielding a rotational temperature of about 25 K. The ambient pressure of the sample chamber was maintained at ~100 mTorr by a combination vane pump/Roots blower.

RESULTS

Figure 3.3 shows a representative scan of one of the S-branch triplets, S(9), for both jet and static cell conditions. Figures 3.4-3.8 show CARS spectra of each line of static O_2 from N=1-19 while Figure 3.9 shows the CARS spectrum of the N=1 triplet obtained using a free jet expansion of O_2. The wavenumbers of the peak maxima, along with the more correct transition values from spectral simulations are given in Table 3.1 for each $\Delta N=2$, $\Delta J=2$ line from N=1-19. A combination of the uncertainties of the I_2 lines (2σ = 0.002 cm^{-1})[67] and in the CARS peak determination leads us to an estimated uncertainty of ± 0.005 cm^{-1} for the absolute rotational frequencies reported in Table 3.1; relative frequencies within each triplet are believed to be accurate to 0.001 cm^{-1}.

DISCUSSION

To obtain the true transition frequencies and intensities in the O_2 spectrum, wherein the width of the peaks is comparable to the peak-to-peak separation, it is necessary to model the interference of each line with its neighbors. The magnitude of this interference will vary depending on the dominant line broadening mechanism (e.g., collisional, Doppler, instrumental, etc.). Correct modeling is especially important in CARS since interference of both the real and imaginary parts of the lineshape function must be considered, as discussed in some detail below.

Interference effects

In a spontaneous Raman spectrum with two adjacent peaks, the inner

shoulder of each line adds intensity to the other line, resulting in a higher apparent transition frequency for the lower peak and *vice versa*. In CARS, however, the intensity is proportional to:

$$I \propto \left(\sum_j \chi_j' + \chi_{NR}\right)^2 + \left(\sum_j \chi_j''\right)^2 \qquad (3.3)$$

where χ_j' is the real part and χ_j'' the imaginary part of the third order susceptibility $\chi^{(3)}$ for each transition. The term χ_{NR} represents a small, constant nonresonant contribution which was taken to be zero in this work. It is well known that the Raman intensity is simply proportional to χ'' but, as seen in Eq. 3.3, the contribution of both the real and imaginary parts of χ for all active transitions must be considered when calculating $|\chi|^2$ to get the intensity of a CARS transition. The contributions of transitions very close in frequency to the line of interest will have the greatest perturbing effect but there is still a significant effect when the peaks are separated as much as 10 times the full linewidth.

To illustrate these points, Figure 3.10a shows both the real and imaginary parts of two Lorentzian peaks, spaced by 1.5 times their full widths (Γ_{Lor}). In this situation, the positive contribution of χ_{real} of the lower peak destructively interferes with the negative contribution of χ_{real} of the upper peak as shown in Figure 3.10b. Note also that constructive interference increases the magnitude of χ_{real} on the outer wings of the two peaks. Thus, when χ_{imag} and χ_{real} are squared (Figure 3.10c) to obtain the CARS intensity, χ_{real}^2 has the effect of shifting the apparent peak maxima of the two peaks outward and also of extending the wings of the peaks, as shown in the CARS spectrum in Figure 3.10d.

The net shift from the true transition frequency of a peak as a function of its separation from another equal intensity, higher frequency peak is shown in Figure 3.11 for both spontaneous Raman scattering and CARS. The case of two Lorentzian peaks treated in Figure 3.11a would correspond to an experimental situation in which collisional broadening dominates. Both the ordinate and abscissa are in units of peak fullwidth at half maximum. As can be seen by the steep, linear portion of the curves, until two peaks are resolved a single maximum is located at a frequency halfway between the two lines. In the CARS case (solid line), the resolution of the two peaks occurs at a smaller peak-to-peak separation than in the spontaneous Raman case (dashed line). This is due again to the cancellation of the real contributions in the intermediate frequency region for CARS.

The two peaks are first resolved at a separation of ~$0.5\Gamma_{Lor}$, at which point, the apparent maxima will be shifted inward by ~$0.25\Gamma_{Lor}$ from their true positions due to the constructive interference of χ_{imag}. This maximum shift decreases with increasing peak-to-peak separation. The shift from the true maxima in the spontaneous Raman spectrum drops quickly to 10% of Γ_{Lor} when the separation is greater than one fullwidth. In the CARS spectrum, however, the contribution of χ_{real} of the two peaks serves to push them away from each other. This effect reaches a maximum when the peak to peak separation is approximately 1.5 times Γ_{Lor} and then decreases very slowly, due to the long wings of χ_{real}. In fact, at a separation of 10 x Γ_{Lor}, the shift from the true maximum is still equal to five percent of Γ_{Lor}.

Figure 3.11b illustrates the shifts that occur when the Doppler effect is the

dominant line broadening mechanism and the peaks are almost purely Gaussian. Here, two Lorentzian lines of negligible width are used, with χ_{real} and χ_{imag} then individually convoluted with a Gaussian lineshape before combining for the CARS spectrum. The shift trends are the same as for the Lorentzian case (Figure 3.11a) but the effect falls off more rapidly. Finally, we note that when the dominant source of line broadening is instrumental, the CARS and spontaneous Raman peak frequency shift trends are similar to the Raman case in Figure 3.11b, since instrumental broadening is usually modeled by convoluting a Gaussian lineshape over χ^2, rather than the individual parts[68].

Spectral simulation

From the above considerations, one would expect noticeable interference effects for each closely-spaced O_2 triplet, with the outermost peaks shifted away from the center peak, which would be relatively unperturbed in frequency. The intensity and linewidth of the center peak should be diminished however, due to the cancellation of χ_{real} by the outer peaks. Thus, to extract the best measure of the true transition frequencies and intensities, the following procedure was used. First, a stick spectrum was generated for each triplet with lines initially at the experimental peak frequencies. Each of these lines was given a Lorentzian lineshape to account for the collisional broadening. For the static 70 torr experiments, the FWHM for this Lorentzian was estimated from earlier O_2 pressure broadening studies[57,64,69,70] to be 0.006-0.009 cm^{-1}, depending on the N-value. For the low density jet expansion experiments, a width of 0.001 cm^{-1} was used. The

contributions to each line of both χ_{real} and χ_{imag} of the three triplet transitions were then calculated.

To account for the Doppler broadening, a Gaussian function was convoluted over both the real and imaginary parts of the Lorentzian lineshape using a program adapted from that of Palmer[71]. In order to properly treat the Doppler effect it was also necessary to consider the crossed beam geometry of our experiment. For this configuration, the Doppler FWHM is

$$\Delta\nu = \Delta\nu_{DOP}\left[1 + 4\sin^2\frac{\theta}{2}(\nu_0^2 + \nu_0\nu_R)/\nu_R^2\right]^{\frac{1}{2}} \qquad (3.4)$$

where $\Delta\nu_{DOP}$ is the collinear width, θ is the crossing angle of the two yellow beams, ν_0 is the laser frequency, and ν_R is the rotational transition frequency in cm^{-1} [72]. The second term in the brackets becomes dominant at small Raman shifts, and in fact, at our crossing angle of 1.95°, gives a Doppler width of 45 ν_{DOP} for the S(1) lines at 14 cm^{-1}. For the O_2 static cell experiments at 300K, the Doppler fullwidths were nearly constant, ranging from 0.00140 cm^{-1} for N=3 to 0.00142 cm^{-1} for N=19. For the jet spectra, these values dropped by a factor of $(25/300)^{1/2} = 0.29$ since $T_{ROT} = 25K$ ($\approx T_{TRANS}$) was deduced from the relative intensities of vibrational *Q*-branch lines of jet-cooled O_2 obtained under identical experimental conditions.

After Doppler convolution, χ_{real} and χ_{imag} were squared, added, and the sum then was convoluted with a Gaussian lineshape function to account for instrumental broadening. The two yellow input beams responsible for the rotational transition have a FWHM of ~4 ns which gives a Fourier-transform FWHM of 0.004 cm^{-1} for each. Since the beams are basically Gaussian in their time profile, the

square of the linewidths are additive to predict a minimum 0.005 cm^{-1} FWHM for the instrumental broadening contribution. In fact, the FWHM value that gave the best fit to all of the data was somewhat larger, 0.010 cm^{-1}. This excess width may be due to residual amplitude modulations in the Nd:YAG amplifier pump due to imperfect seeding. A portion of the excess width may also be due to saturation broadening or to Stark broadening caused by the intense laser beams focused on the sample, as has been reported by other groups[61,73].

The final product of this convolution process, which was performed on a PC with spreadsheets and simple Fortran routines, is a calculated spectrum that can be compared to the experimental data. One may then iteratively adjust the initial peak frequency and intensity parameters to reproduce the experimental spectrum more exactly. The simulated spectra match the experimental data reasonably well as can be observed in Figure 3.3. The experimental data are represented with diamonds and the narrow calculated peaks represent the collisionally and Doppler broadened transitions while the broad calculated peaks that fit the data well also include the 0.010 cm^{-1} instrumental linewidth. The sticks show the peak frequencies and intensities that result in the best fit to the data upon convolution.

Several interesting features can be noted in Figure 3.3. First, the near elimination of Doppler and collisional broadening in the jet-cooled spectrum causes a dramatic improvement in the resolution of the peaks. Indeed the widths of the peaks are virtually entirely due to the instrumental linewidth. Second, since the linewidths of the jet-cooled spectral peaks are much narrower, the interference effect of neighboring transitions is minimized. This can be seen by noting the

positions of the lines in the stick spectra relative to the experimental and/or calculated peaks. In the static O_2 spectrum, the outer experimental peaks are shifted away from the stick peaks whose frequencies correspond to the true Raman transition frequencies. In the jet-cooled O_2 spectrum, the stick and experimental peaks coincide almost exactly.

Third, the relative intensity of the three peaks in the triplet changes as one cools the sample. This effect can be understood by recognizing that, in CARS, the intensity is proportional to the square of the population difference between the initial and final states of the transition. Of the three F_1, F_2, F_3 energy level differences, the F_2 term, which corresponds to the middle peak in each $\Delta J=2$, $\Delta N=2$ triplet, has the smallest Boltzmann population difference and hence the smallest intensity. This effect is minimal at 300 K where the ratio of the square of the Boltzmann factor of F_1, F_2, and F_3 is 1.0:0.98:1.0 for the *S(9)* line. At 25 K, however, the same ratio becomes 1.00:0.78:0.99; thus, the intensity of the center peak is seen to diminish by 20% relative to the intensity at 300K.

Frequency and intensity results

The peak frequencies obtained from the simulation process are tabulated in column 3 of Table 3.1. These corrected positions differ from the experimental peak maxima by 0.000 to 0.003 cm^{-1}, an appreciable fraction of the average triplet spacing of 0.022 cm^{-1} for the N>5 lines. In general, the corrections are greatest for the most closely spaced triplets, as expected. The difference between the corrected frequencies and the frequencies calculated from Eq. 3.3 is shown in column 4 of

Table 3.1. As can be seen, the frequency agreement is excellent with no apparent trend in discrepancies; virtually all of the frequencies agree with the calculated values within the 0.005 cm^{-1} level of uncertainty.

The intensities of each peak of the 300K spectra were obtained from the spectral simulation and converted to values (column 6 of Table 3.1) that can be directly compared to the Raman intensities calculated by Altmann *et al.*[60] (column 7 of Table 3.1). All values have been normalized to the highest J member of each triplet. Since each triplet was scanned separately, no attempt was made to obtain accurate relative intensities for different values of N. The agreement between the simulated and calculated intensities is fair but a systematic deviation does seem to exist. In particular, relative simulated intensities of low J=N, N-1 triplet members are consistently higher than the calculated values in each case.

The source of this discrepancy is not certain although one possible explanation may be that the assumption of constant linewidth within each triplet is incorrect. Some evidence that such might be the case was seen in the simulations, which suggest that within each triplet, the low J widths might be narrower than the high J values. We note that this would yield relative peak intensities closer to the theoretical values but also that this is the opposite of the linewidth increase observed with decreasing N[65,69,70]. The latter occurs because inelastic collisions, the dominant broadening source[65], are more effective for closely spaced levels (low N). However, this energy gap effect should be comparable for the different J sublevels of a given N value. It may be significant that the high J sublevel has more M_j orientational states and, in fact, Gardiner *et al.*[74] have measured varying

collisional linewidths for different M_j levels of O_2 studied by EPR spectroscopy. The effect is small but suggestive of a larger width for larger M_j values, a result that would be consistent with our observations. Another factor which might contribute a greater width for high J levels is the greater number of components (J+1) expected for any AC Stark broadening. A more thorough study of the linewidth pressure-dependence and of the Stark effect on each $\Delta N=2$, $\Delta J=2$ peak would be useful in gaining a clearer picture of the true intensity patterns of these triplets.

SUMMARY

Experimentally-determined frequencies for the $\Delta J=2$, $\Delta N=2$ rotational transitions of oxygen are reported, using a newly developed high resolution low-frequency CARS spectrometer. These frequencies match well the prediction obtained by using a Hamiltonian appropriate to a coupling scheme intermediate between Hund's case (a) and (b) and molecular constants obtained from magnetic dipole microwave studies. The appearance of each triplet was simulated and the corrected transition frequencies obtained by considering the various contributions to the CARS spectral linewidth. Some discrepancies in intensities remain and may be due to a J dependance of the triplet linewidth.

ACKNOWLEDGEMENTS

Special thanks go to Mr. Mansour Zahedi for his work in developing the spectral simulation routines.

Table 3.1: Rotational Raman transitions of oxygen.

S(J,N)	Observed cm^{-1}	Corrected cm^{-1}	Corrected-calculated	Simulated intensity	Calculated intensity[a]
S(0,1)	16.252	16.252	-0.001	0.48	
S(1,1)	14.377	14.377	0.001	0.49	0.51
S(2,1)	14.303	14.303	0.000	1.00	1.00
S(2,3)	25.947	25.946	-0.001	0.70	0.59
S(3,3)	25.878	25.877	0.002	0.89	0.76
S(4,3)	25.837	25.839	0.003	1.00	1.00
S(4,5)	37.407	37.407	0.000	0.76	0.72
S(5,5)	37.368	37.369	0.000	0.94	0.84
S(6,5)	37.341	37.341	0.000	1.00	1.00
S(6,7)	48.883	48.882	-0.003	0.83	0.78
S(7,7)	48.854	48.855	-0.002	0.89	0.88
S(8,7)	48.830	48.832	-0.001	1.00	1.00
S(8,9)	60.361	60.359	-0.002	0.90	0.82
S(9,9)	60.336	60.337	0.000	1.00	0.90
S(10,9)	60.314	60.316	0.000	1.00	1.00
S(10,11)	71.831	71.829	0.000	0.94	0.85
S(11,11)	71.809	71.809	0.001	1.04	0.92
S(12,11)	71.787	71.790	0.002	1.00	1.00
S(12,13)	83.291	83.290	0.003	1.01	0.87
S(13,13)	83.270	83.270	0.003	1.07	0.93
S(14,13)	83.249	83.252	0.005	1.00	1.00
S(14,15)	94.734	94.731	-0.001	0.97	0.88
S(15,15)	94.712	94.712	0.000	1.07	0.94
S(16,15)	94.692	94.695	0.002	1.00	1.00
S(16,17)	106.160	106.159	-0.002	1.03	0.90
S(17,17)	106.141	106.142	0.000	1.09	0.95
S(18,17)	106.120	106.123	-0.001	1.00	1.00
S(18,19)	117.579	117.578	0.004	0.96	0.91
S(19,19)	117.560	117.560	0.005	1.02	0.95
S(20,19)	117.542	117.543	0.006	1.00	1.00

[a]Intensities from Ref. 61. S(0,1) is omitted since it overlaps with the R(2,1) line.

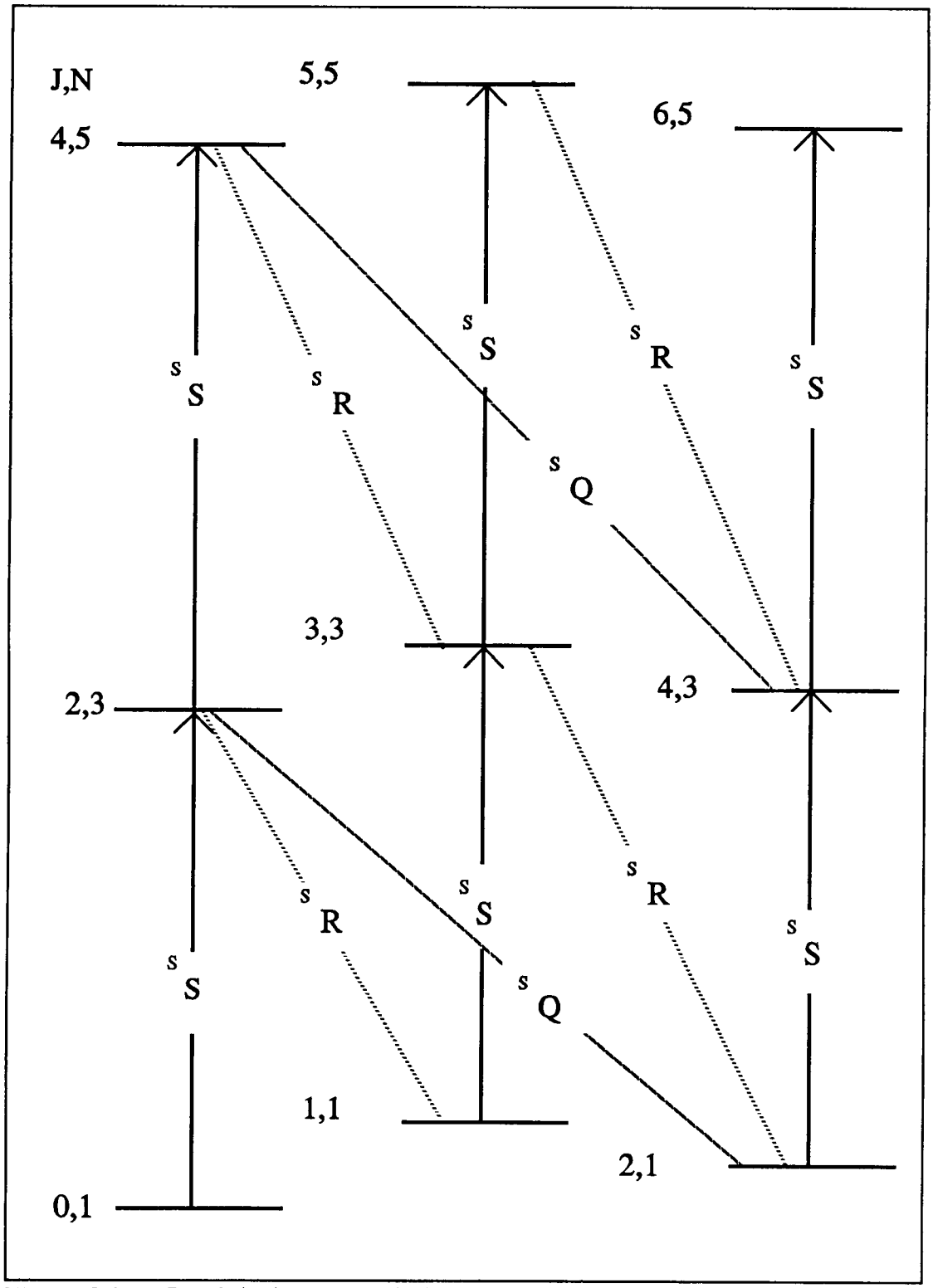

Figure 3.1: $\Delta J = 0$ (Q-), $\Delta J = 1$ (R-), and $\Delta J = 2$ (S-) branch transitions of the $N = 1$, 3, and 5 rotational levels of oxygen.

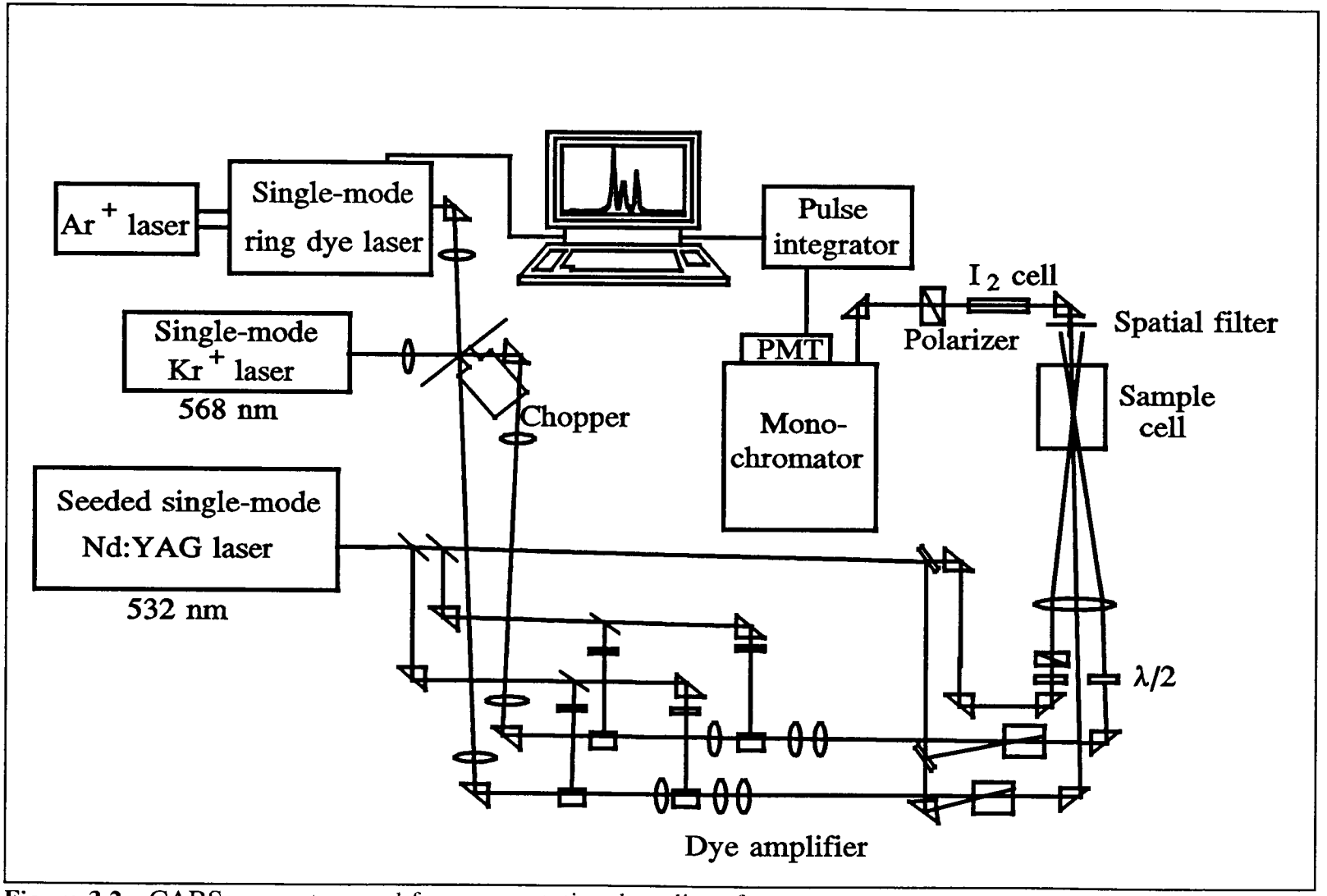

Figure 3.2: CARS apparatus used for pure rotational studies of oxygen.

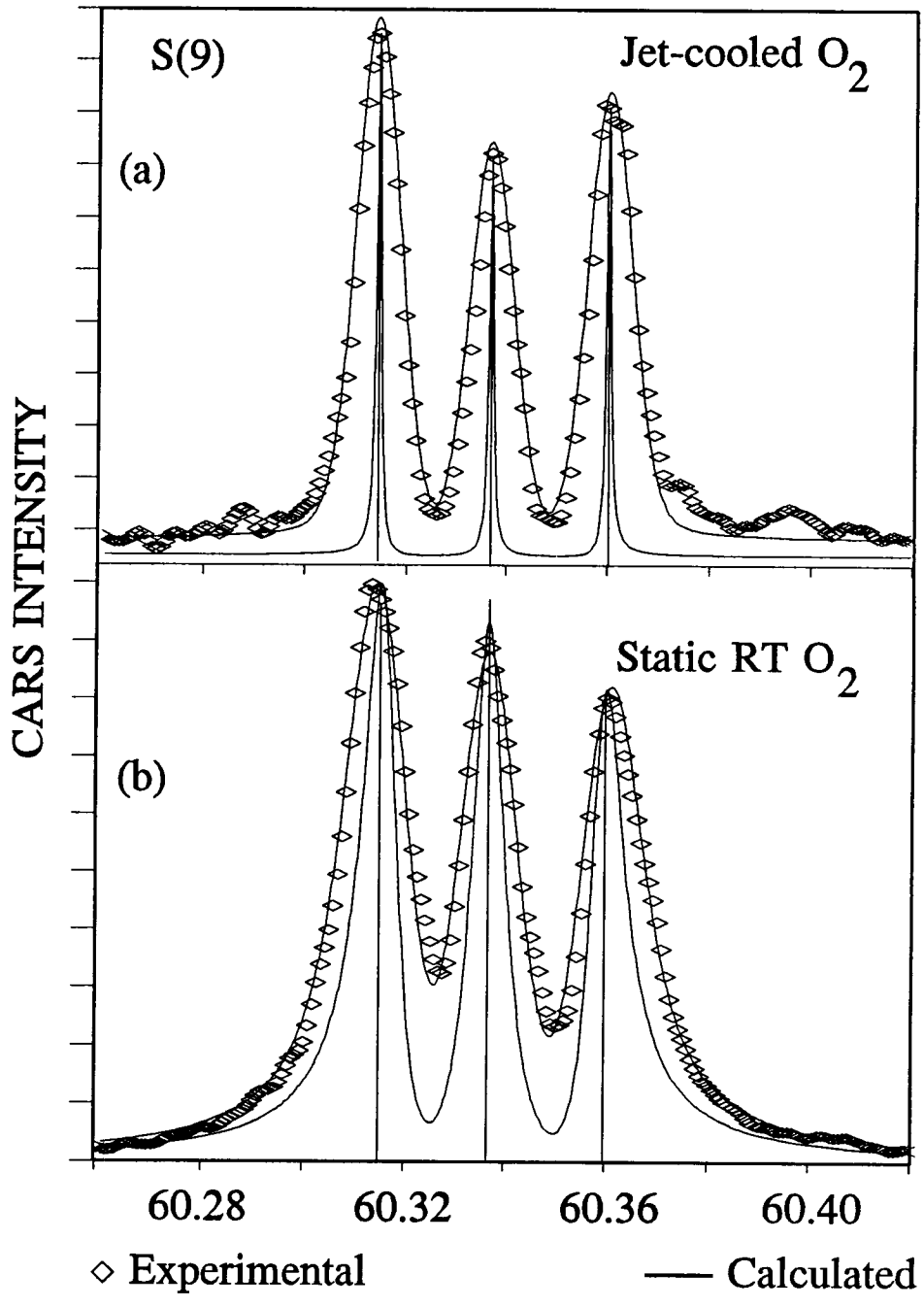

Figure 3.3: O_2 in jet expansion (a), and in static cell (b). Narrow calc. peaks represent natural, collisional, and Doppler widths. Broad calc. peaks include laser linewidth.

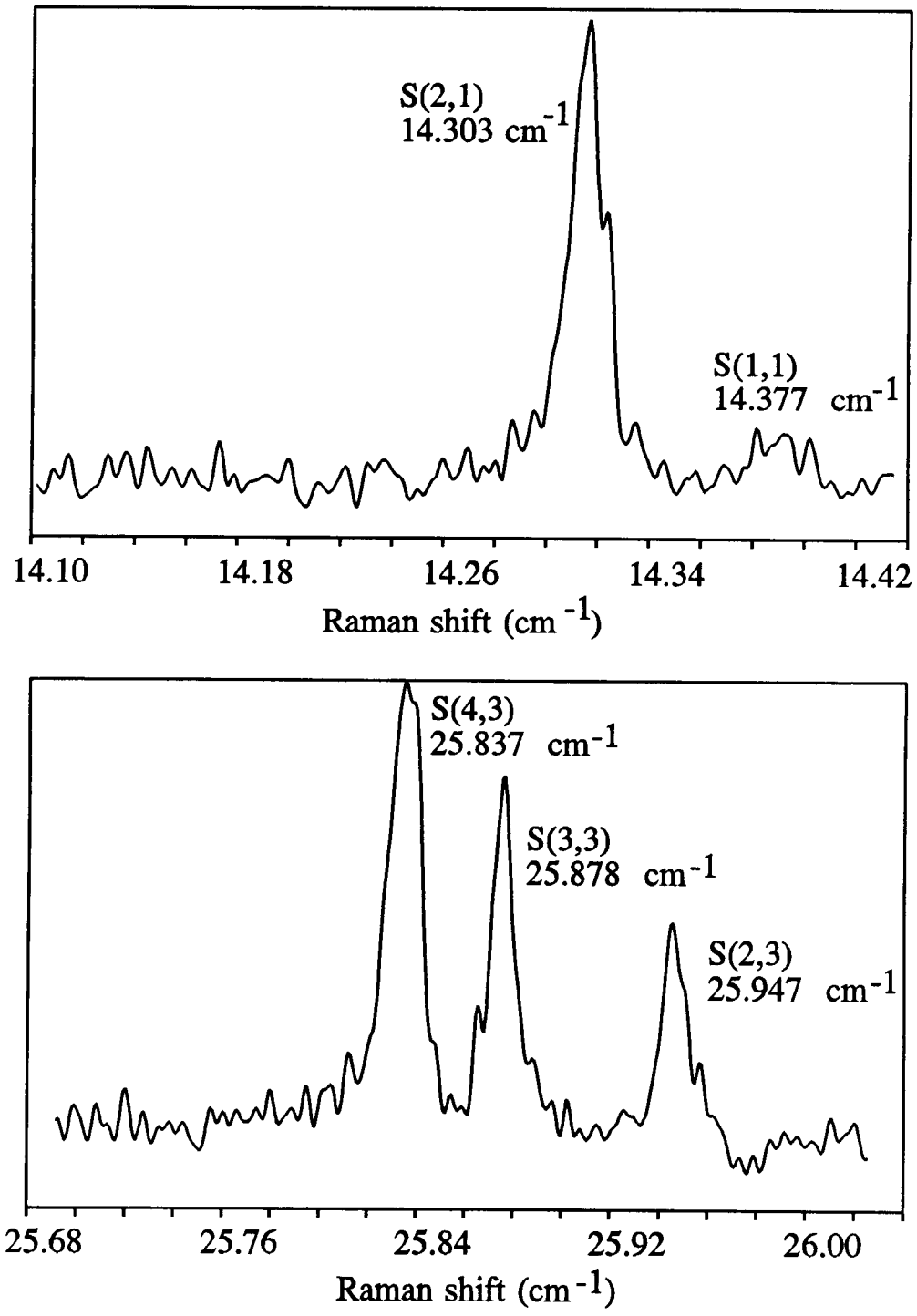

Figure 3.4: Pure rotational spectra of S(1) and S(3) triplets of O_2 (static, 70 torr).

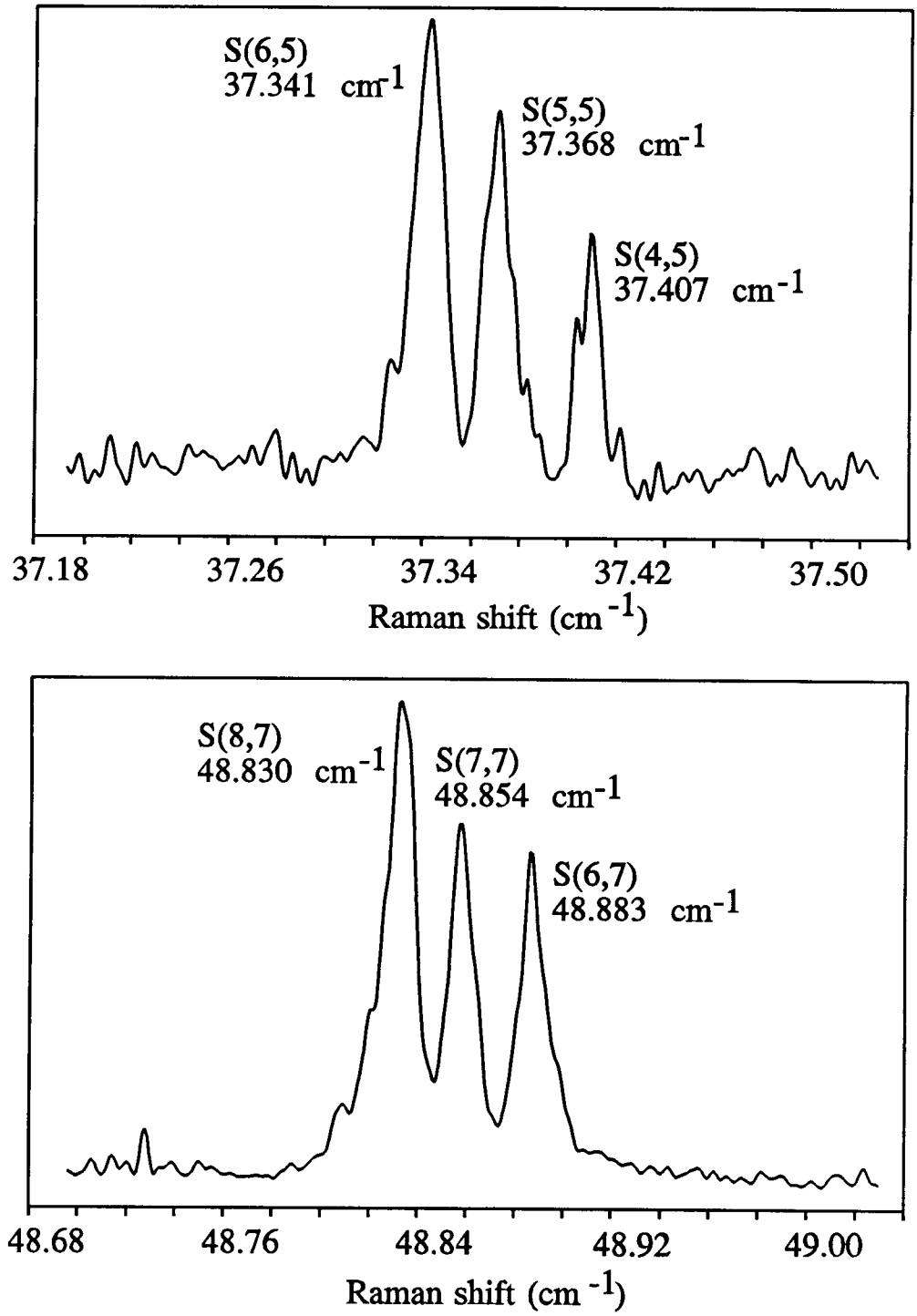

Figure 3.5: Pure rotational O_2 spectra of S(5) and S(7) triplets (static, 70 torr).

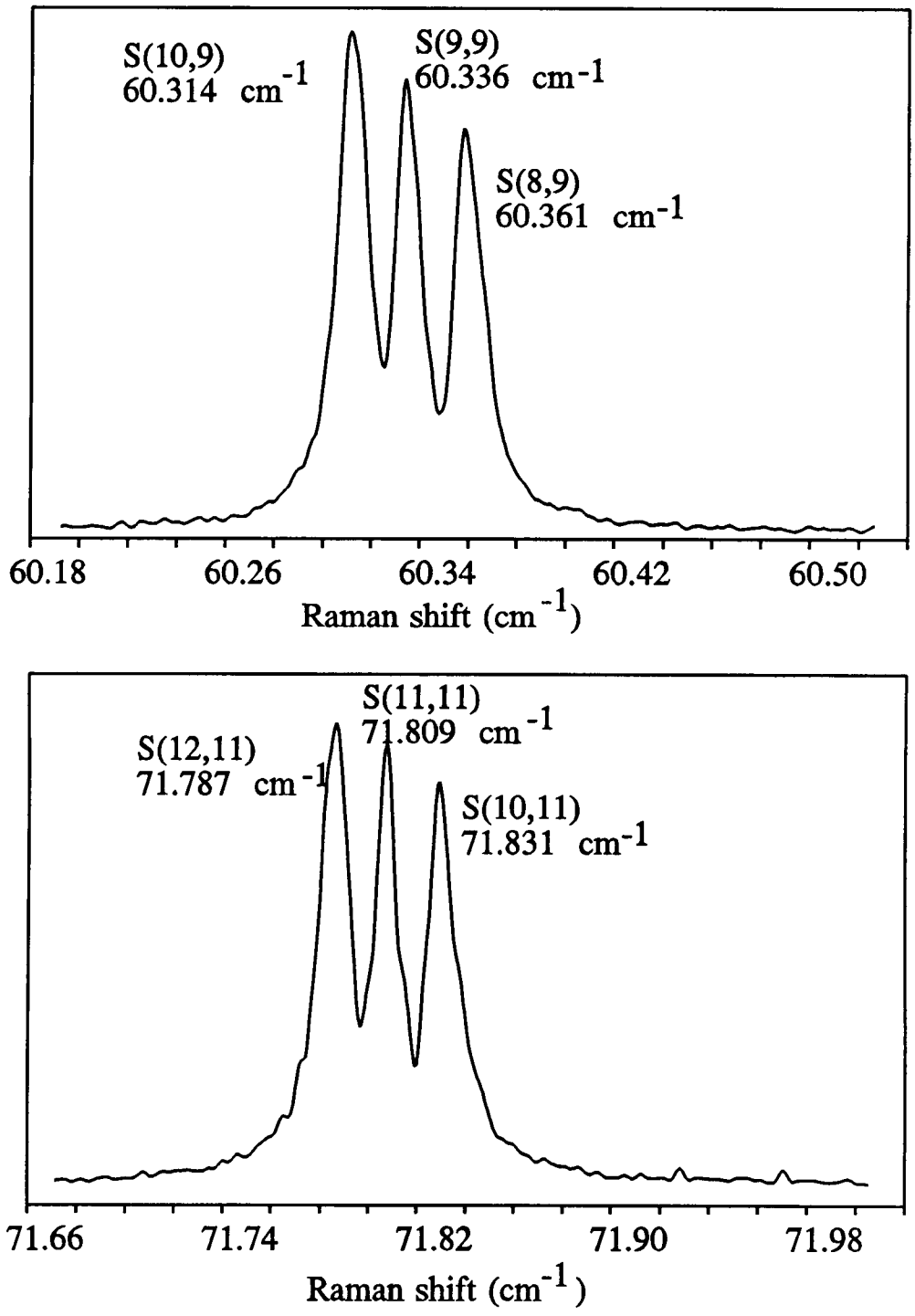

Figure 3.6: Pure rotational O_2 spectra of the S(9) and S(11) triplets (static, 70 torr).

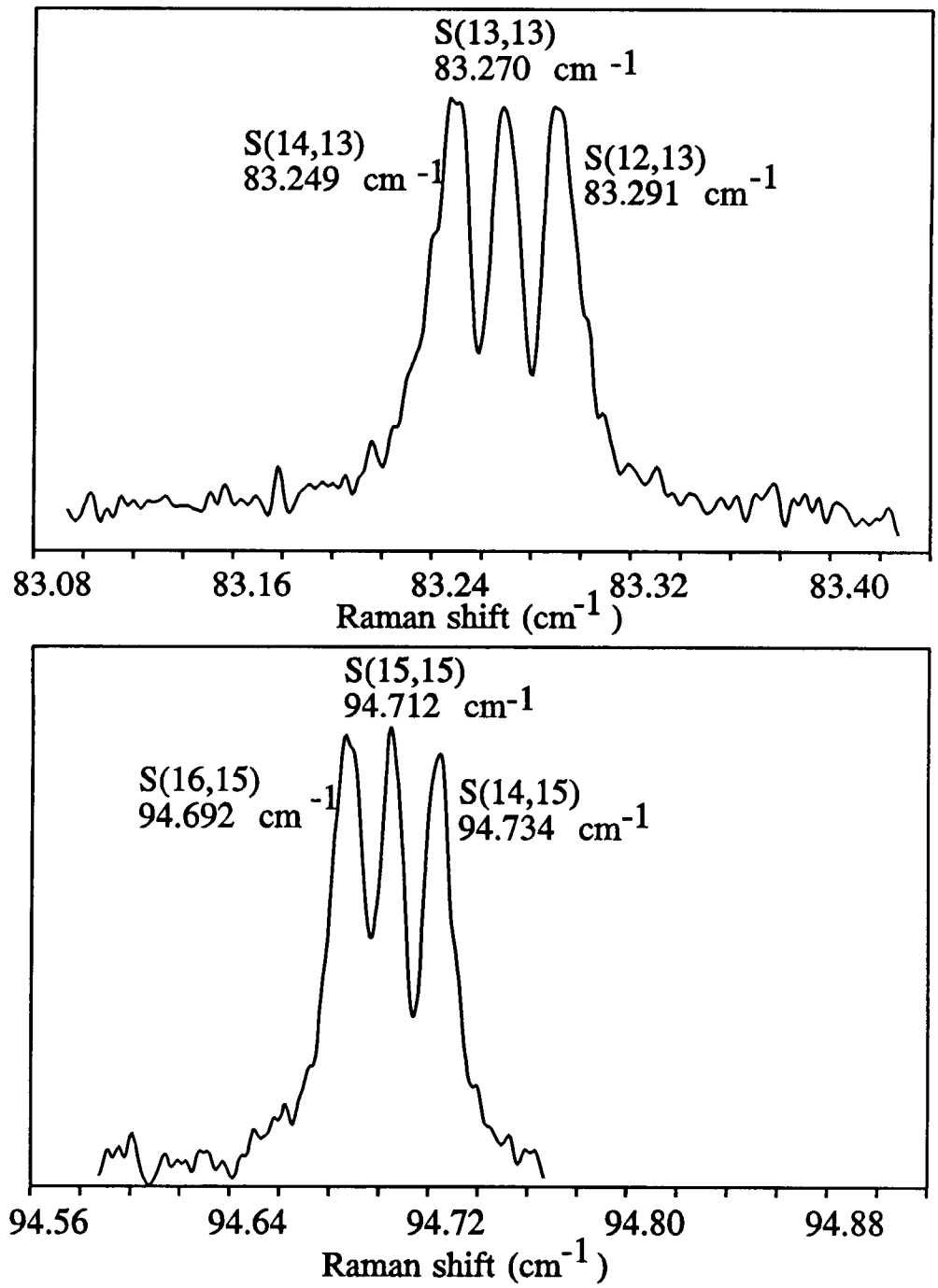

Figure 3.7: Pure rotational O_2 spectra of the S(13) and S(15) triplets (Static, 70 torr).

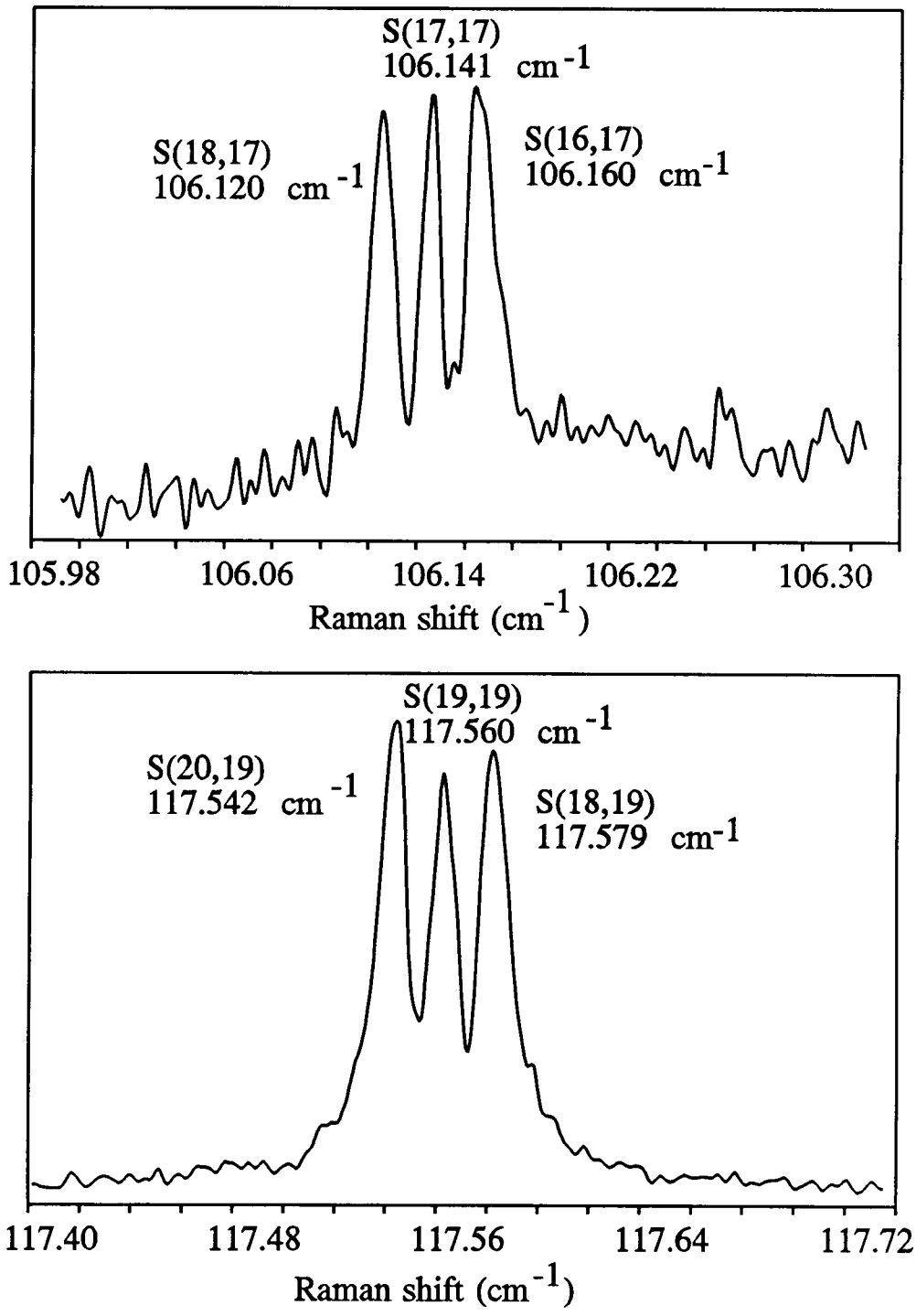

Figure 3.8: Pure rotational O_2 spectra of the S(17) and S(19) triplets (static, 70 torr)

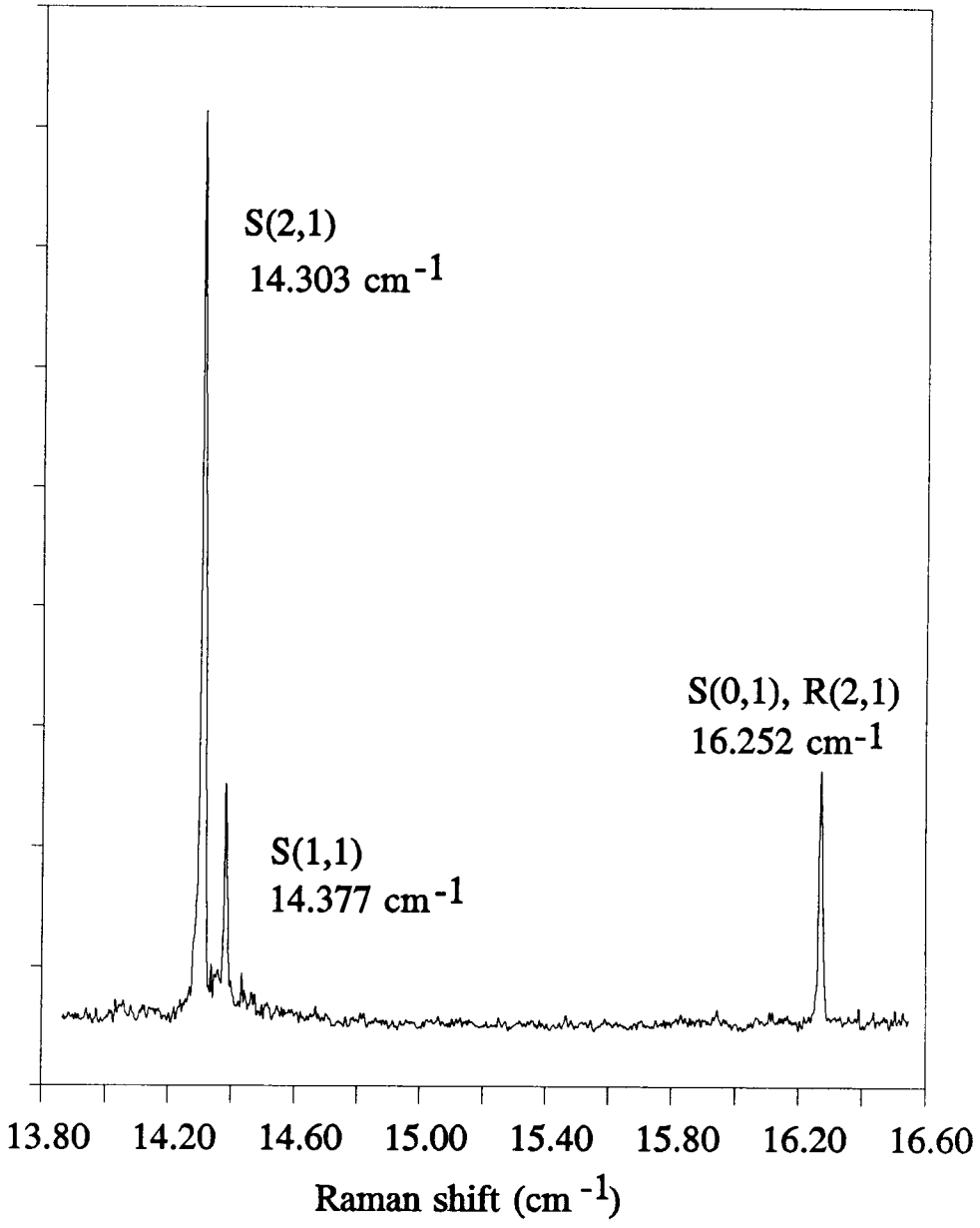

Figure 3.9: Pure rotational O_2 spectra of S(1) triplet (neat jet expansion, p_0 = 5 atm, T_0 = 300 K. The S(0,1) and R(2,1) lines are coincident in frequency.

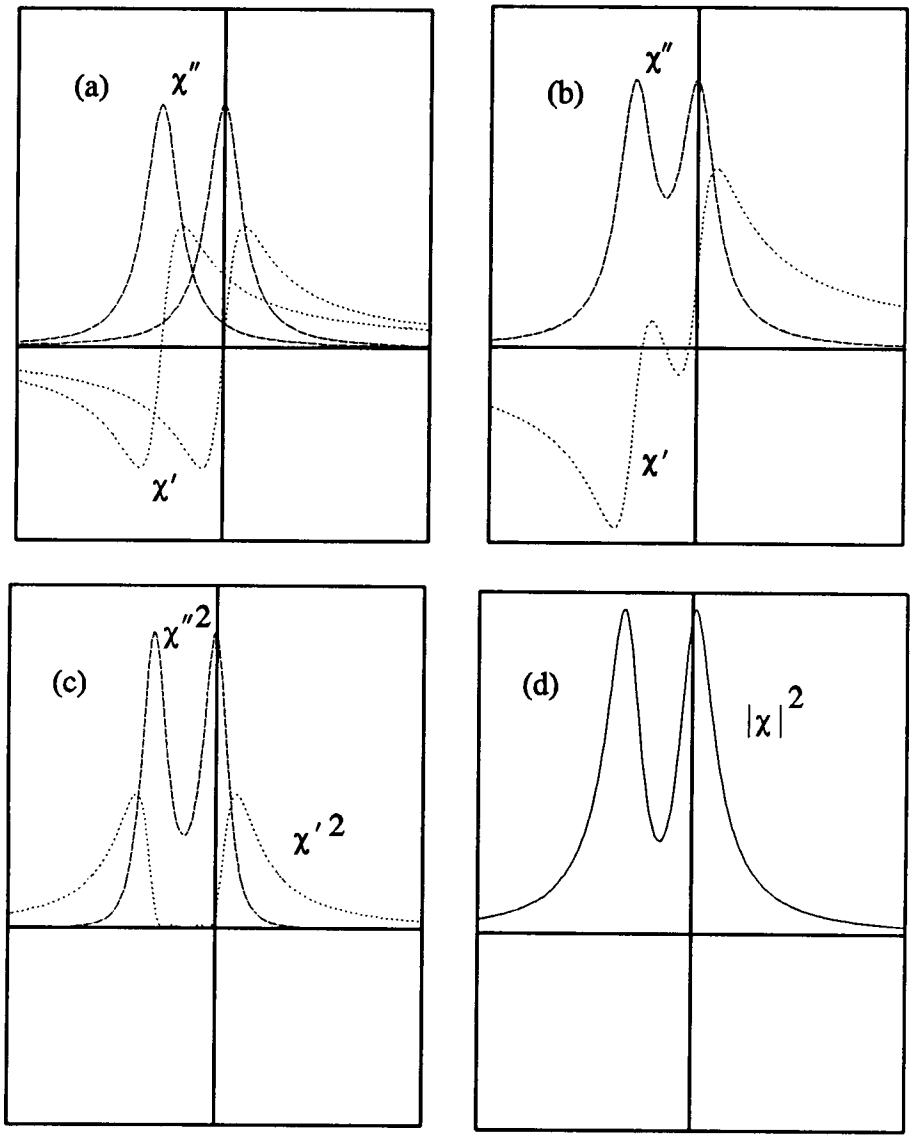

Figure 3.10: (a) Real χ' and imaginary χ'' parts of two Lorentzian lines spaced by 1.5 full linewidths. (b) Real parts and imaginary parts separately summed. The latter is equivalent to the Raman spectrum. (c) Real and imaginary sums squared. (d) Resulting CARS spectrum.

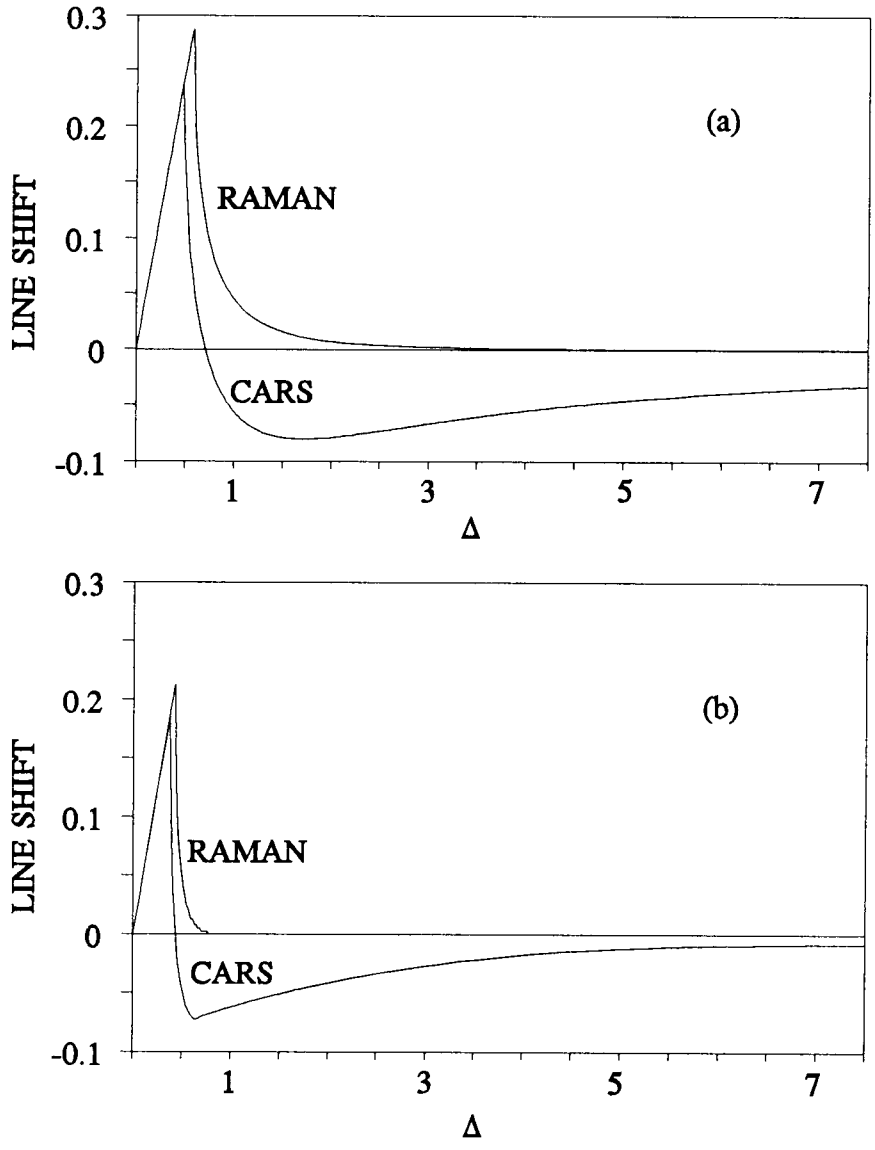

Figure 3.11: Line position shifts as a function of spacing Δ between two equal intensity Lorentzian-shaped lines (a), and Gaussian-shaped lines (b). Both shifts and Δ are in units of respective FWHM linewidths.

OXYGEN

$$^3\Sigma_g^-$$

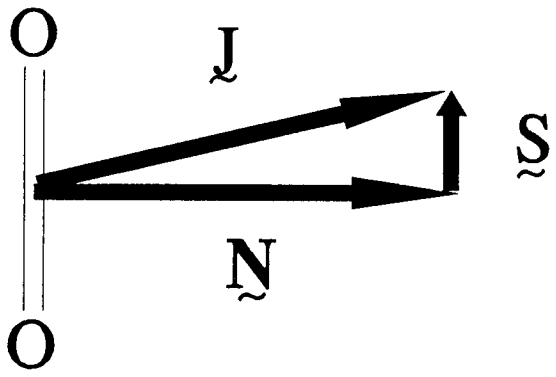

$$J = N + 1$$
$$S=1 \Rightarrow J = N$$
$$J = N - 1$$

Figure 3.12: Coupling of molecular angular momentum with electron spin.

CHAPTER 4 THE CARS STUDY OF MEDIUM-TO-LARGE SIZED CLUSTERS OF CO_2

INTRODUCTION

In a molecular free jet expansion, a gas sample contained in a high pressure reservoir is exhausted into an evacuated chamber through a small orifice. The random thermal energy of the sample is converted into kinetic energy of directed flow in this isentropic, isenthalpic process. In the region just outside the nozzle tip, a highly supersaturated condition can exist where the molecules in the expansion are cooled to such an extent that when collisions occur, the attractive forces between molecules can exceed the repulsive interactions, resulting in the growth of clusters[75,76,77]. This process of molecular accretion is the subject of this and the following chapter. Here, we focus on the use of high-resolution coherent anti-Stokes Raman spectroscopy (CARS) for the examination of medium to large CO_2 clusters formed in a free jet expansion.

In previous work done in this laboratory, clusters of several non-polar molecular species have been examined by coherent Raman techniques[78,79,80,81]. Through these studies, a better understanding of cluster thermodynamics has been obtained, particularly with respect to phase changes in the expansion region. Raman spectroscopy is well-suited to this application since both the vibrational frequency and peak lineshapes are very

sensitive to both the temperature and the level of order in condensed-phase clusters. If the aggregates are large enough, they exhibit properties characteristic of bulk material. Just how many molecules are necessary to form a bulk-like cluster is an open question and estimates have ranged from as low as 10 molecules per cluster[82] to 100 per cluster[83].

The importance of understanding the progression from single molecules to bulk material is reflected in the wide variety of fields in which cluster properties are studied. For example, in atmospheric science, many phase changes such as hail formation, water condensation, and formation of solid aerosols require small nuclei to initiate the process. In metallurgy, the physical properties of bulk metals are determined in part by the cluster concentration and thus the metal grain size. The nucleation and growth of small metal particles on substrates is important in the solid-state semiconductor industry. In catalysis, it has been shown that small metal and metal-oxide clusters with large surface area are much more effective in promoting chemical reactions than the same bulk materials of larger size.

In an interesting discussion, Stein[84] has illustrated the importance of understanding the properties of clusters. His argument can be paraphrased as follows. In bulk macroscopic thermodynamics, a single component system can be completely described by three properties. The volume of the system, for example, is a function of pressure, temperature and mass, $V_1 = f_1(P,T,m_1)$. When the system is halved, each half can then be correctly described by $V_2 = f_2(P,T,m_2)$ where $m_2 = m_1/2$. If one continues to divide the system in half, however, eventually, other properties start to be exhibited that must be described by other variables. For

example, when the size becomes very small, the components of the system begin to stick to each other and the surrounding surfaces. At an even smaller system size, the individual particles begin to levitate in the medium, exhibiting Brownian motion. Clearly, additional properties such as size, surface charge, and surface free energy must be specified to uniquely describe the thermodynamics of the system.

In a classic physics problem, a gas is enclosed in a cylinder by a freely moving piston that is subject to constant pressure. As heat is removed from the gas, the piston slowly descends until a phase change occurs, producing droplets at the bottom of the cylinder. Classical thermodynamics predicts that this phase change will occur at the vapor-liquid equilibrium temperature. In reality, however, one often finds that supersaturation of the gas occurs and the phase change takes place at a lower temperature than the equilibrium.

To form a droplet, a surface is needed onto which the liquid will collect. If no surface is available, as in the case of a free jet expansion, homogeneous nucleation must occur. In other words, the droplet must grow upon itself. This is only possible in a supersaturated system. From classical nucleation theory[78], the smallest possible radius of such a droplet is given by

$$r* = 2\sigma m/[\rho_L kTlnS] \qquad (4.1)$$

where σ is the surface tension, m the molecular mass, ρ_L the liquid density, and S the saturation ratio P/P_0, where P_0 is the equilibrium vapor pressure. Once this minimum radius is exceeded, the droplet will grow until thermodynamic equilibrium is reestablished in the system. It follows from Eq. 4.1 that the greater the supersaturation, the smaller the minimum droplet radius, and the greater the rate

of formation of the droplets or clusters.

In a free jet expansion, the extent of supersaturation and hence condensation is governed by many factors. It has been shown[85] that the average cluster size decreases with decreasing source pressure, p_0, and increasing source temperature, T_0. Furthermore, diluting a sample such as CO_2 in a carrier gas such as Ne or He promotes the formation of smaller clusters. This is due to the fact that when a collision between a CO_2 molecule and a Ne gas atom occurs, energy from the internal degrees of freedom of the CO_2 is transferred to kinetic energy of the Ne. This cools the CO_2 and increases the likelihood of aggregation when the cooled molecule collides with other CO_2 molecules; hence, the minimum cluster size is smaller. However, due to the small relative density of CO_2, this minimum cluster size is not reached until further downstream than in the neat case. Then, after this initial aggregate has formed, the number of additional accreting collisions rapidly diminishes at greater distances from the nozzle, thereby limiting the final size of the cluster.

By appropriately varying the source conditions, therefore, a range of sizes of clusters can be selectively produced and examined to model the progression from single molecules to bulk-like aggregates. Two extreme cases can be considered: the expansion of a pure sample from a jet where p_0 is high and T_0 is low, resulting in large bulk-like clusters; and the expansion of a dilute sample with low p_0 and high T_0 to produce very small clusters. Both cases have been explored in this work with CO_2 as the sample gas. Here, large- to medium-sized clusters are studied and in the following chapter, the formation of very small clusters, e.g., dimers and trimers,

is described.

BACKGROUND INFORMATION

Carbon dioxide has been the subject of many theoretical and experimental studies, due perhaps both to its ubiquity in nature and its simple nonpolar structure, which limits the types of fundamental intermolecular forces. Monomeric CO_2 has three fundamental vibrational modes, of which only the totally symmetric stretch, ν_1 is Raman active. An interesting feature of CO_2 is the fact that the frequency of ν_1, 1340 cm^{-1}, is nearly equal to the frequency of the first overtone ν_2 of the bending fundamental mode, 1330 cm^{-1}. When two vibrational levels belonging to different vibrations of the same symmetry species have nearly equal energy, a perturbation of the vibrational energy levels occurs. This was first treated by Fermi[86] for CO_2, hence such a perturbation is termed Fermi resonance. The interaction causes one of the vibrational levels to be shifted downward and the other to be shifted upward in energy, with a mixing of the eigenfunctions of the two states. The magnitude of the shift and mixing are greatest when the unperturbed energy level difference is the smallest. In carbon dioxide, the Fermi resonance between $2\nu_2$ and ν_1 results in the appearance in the gas-phase Raman spectrum of two vibrational bands at 1285 cm^{-1} and 1388 cm^{-1}. Although the mixing of eigenstates is so complete that it is inaccurate to designate one band ν_1 and the other $2\nu_2$, we will follow convention in labeling the 1388 cm^{-1} band ν_1 and the 1285 cm^{-1} band $2\nu_2$.

The ν_1, $2\nu_2$ vibrational transitions of the condensed phases of CO_2 give rise to spectral peaks that have slightly lower Raman shifts than the monomer. The vibrational peaks of liquid CO_2 (which only exists at pressures greater than 5.1 atm) are broad in both the lower and upper spectral regions (2 cm^{-1} FWHM) and occur at 1279 cm^{-1} and 1385 cm^{-1} respectively (at T = 218 K and P = 5.4 atm).

Solid CO_2 has a cubic structure with four molecules per unit cell. Each monomer vibration gives rise to a totally symmetric mode, A_g, in which all four molecules are vibrating in phase, and an asymmetric mode, T_g, where the molecules are vibrating out of phase from each other. In the $2\nu_2$ solid CO_2 spectrum, the A_g and T_g mode peaks are separated by ~0.37 cm^{-1} and with sufficient spectral resolution, both can be observed at cryogenic temperatures. In the ν_1 spectrum, however, the two peaks are nearly coincident in frequency and have not been resolved[87].

The linewidths and frequencies of the solid peaks are sensitive to temperature and are thus good measures of the thermodynamic temperature of the solid and, as applied here, of large bulk-like clusters. For this purpose, it was necesary to obtain high-resolution Raman data on cryogenic CO_2, in order to deduce temperature vs. frequency and temperature vs. linewidth curves from the triple point down to near absolute zero. This work was done in collaboration with Alan Richardson and Dr. Nathan Rich and the full experimental details may be found in the thesis of Alan Richardson[88].

CARS spectra were taken of the $2\nu_2$ mode of solid CO_2 at 25 different temperatures in the range of 8K to 217K. The peak frequencies at the different

temperatures are listed in Table 4.1. A sampling of these spectra is shown in Figure 4.1. As the temperature of the solid is lowered, the peak widths become narrower and the T_g mode becomes resolved. The shift to lower peak frequencies with lower temperature is also apparent. Note that the entire frequency shift is only 1.6 cm^{-1}; thus high spectral resolution is necessary to obtain accurate frequency/linewidth vs. temperature curves as shown in Figures 4.2 and 4.3. The linewidth of only the A_g mode peak is plotted in Figure 4.3 since the T_g mode intensity is small, with a larger linewidth uncertainty. Note that in both of these figures the magnitude of change in both the frequency and linewidth decreases sharply when the temperature is dropped lower than 50K. This suggests that nearly maximum order is reached in the CO_2 crystals when cooled below 50K; e.g., no further crystal reordering or contraction occurs. Further details on the spectroscopy of CO_2 and other solid samples can be found in the thesis of Alan Richardson[88].

Again, the purpose of the equilibrium solid CO_2 CARS studies was to obtain frequency and linewidth data to compare with spectral data gleaned from the spectroscopic examination of large bulk-like clusters formed in a free jet expansion. The cluster studies will be described in the ensuing sections.

CARBON DIOXIDE CLUSTERS FORMED IN A FREE JET EXPANSION

Experimental

The setup of the high-resolution CARS spectrometer used in these experiments is similar to that used in the pure rotational studies of oxygen, with

some simplifications as shown in Figure 4.4. Briefly, the frequency-doubled output of a DCR-1 Quanta Ray pulsed Nd:YAG laser, equipped with a Lightwave Electronics Model 6300 injection seeder system, is split into three portions. Two-thirds of the 532 nm output pumps a three-stage dye amplifier chain through which passes the tunable output of a Coherent 699-29 ring dye laser. The amplifier chain, which consists of two transversely pumped cells and one longitudinally pumped cell each containing a dye solution (R6G in this experiment), amplifies the ring dye laser output from ~1 W to ~1 MW in power. The dye beam is then combined with the remaining two portions of 532 nm light, and is directed into the sample cell in a folded BOXCARS configuration[4]. This configuration provides high spatial resolution which is useful in exploring the free expansion zone of the jet; furthermore, it allows for spatial filtering of the CARS signal beam from the input beams. Following spatial filtering, the CARS beam is collimated and directed through a single monochromator into a Hamamatsu R955 photomultiplier tube. The output of the PMT is sent into a SRS SR250 gated pulse integrator and then to the ring dye laser's Apple II computer where it is averaged and stored. Simultaneously, a portion of the ring dye laser output is passed through a cell containing I_2 and onto a photodiode, the signal of which is also collected by the computer to provide a frequency calibration.

The jet nozzle, connected to a commercial grade CO_2 cylinder with a Matheson model 451 filter attached, is a modified Bosch fuel injector valve that operates in a pulsed mode with each 300 μs pulse synchronized to the firing of the Q-switch of the Nd:YAG laser. The details of the nozzle assembly have been

described elsewhere[89]. With the exception of the neat CO_2 expansion experiment, the nozzle used in these studies had a circular orifice 0.2 mm in diameter with a channel length of 0.4 mm.

This geometry is similar to that of the sonic nozzles used in the landmark study of cluster formation by Hagena and Obert[87] wherein the effects of pressure, temperature, nozzle size and test gas on mean cluster size was explored. In that study, experiments were performed using three different types of nozzles: sonic, Laval, and conical (see Figure 4.5a, b, c). It was shown that the source pressure required to form CO_2 clusters of a given size with the sonic nozzle was 5 times that necessary when using a Laval or conical nozzle at temperatures and nozzle diameters similar to the one used in this experiment. In fact, expansions from sonic nozzles have been termed the "worst case" with respect to cluster generation for similar nozzle diameters and stagnation pressures[90] and have been used precisely for the purpose of minimizing cluster formation which is regarded as a nuisance in many beam experiments. Nevertheless, the sonic nozzle used here proved satisfactory for the production of medium and large clusters formed in an expansion of a dilute mixture of CO_2 in a driving gas, and proved even ideal for the formation of very small clusters as described in the following chapter.

The nozzle used in the study of neat CO_2 expansions was a cylindrical type nozzle with a channel length of 2.0 mm and an orifice diameter of 0.2 mm (see Figure 4.5d). This type of nozzle is more favorable than the sonic nozzle for the formation of clusters since the molecular flux along the centerline of the expansion remains high further away from the nozzle; hence, more accreting collisions are

likely to occur.

EXPERIMENTAL RESULTS

Inasmuch as the goal of these experiments has been to learn more of the growth of clusters from dimers to bulk-like solids, it has been necessary to explore a wide range of source conditions, i.e., sample temperature and pressure in the reservoir behind the nozzle, dilution in a carrier gas, etc. Varying these conditions alters the appearance of the CO_2 CARS spectrum significantly. This is especially true in the $2\nu_2$ spectrum of CO_2 which is shown in Figure 4.6 with the spectral regions outlined wherein peaks associated with different-sized clusters are found.

The sharp peak at the right of the spectrum is the Q-branch of the CO_2 monomer. In an expansion where the source pressure, p_0 is very low (2-4 atm), and the source temperature is warm (300 K), small sharp features appear immediately surrounding the Q-branch peak. These features are especially pronounced in the ν_1 spectral region and will be described in detail in the following chapter.

The group of peaks between 1277 cm^{-1} and 1283 cm^{-1} appears in moderate to harsh expansions with the relative intensity of the constitutent peaks varying strongly with source conditions. Although the frequency of at least one of these features coincides with that of bulk liquid CO_2 at 1279 cm^{-1}, a comparison of the linewidth of these peaks vs. the liquid CO_2 peak shows that the liquid peak is much broader (2 cm^{-1} FWHM at 213 K). Furthermore, Beck[91] has shown that with N_2, condensed phase transitions occur almost instanteously in the jet expansion and that

except for the point in the jet expansion where the phase transitions actually occur, coexisting phases do not exist. The origin of these middle spectral peaks will be considered in a later section of this chapter, but first, the 1275 cm^{-1} peak will be explored.

Bulk-like solid CO_2 clusters

To see if the spectral feature near 1275 cm^{-1} can be compared to the equilibrium crystalline CO_2 feature found at the same frequency, a free jet expansion of pure CO_2 was examined with the source conditions set to p_o = 27 atm and T_o = 298 K. Under these source conditions, light scattering from CO_2 clusters is visible to the naked eye in the cell as the clusters pass through the laser beam. Representative CARS spectra are shown in Figure 4.7 at varying distances from the nozzle tip in units of X/D where X is the distance from the nozzle and D is the nozzle orifice diameter. The very sharp feature at 1276.85 is the O(4) line of CO_2 monomer and served as a useful calibration point. The broad feature to the left of the monomer peak shifts to lower Raman shift and becomes narrower as the cluster cools. This is consistent with the behavior of crystalline CO_2.

By comparing the cluster peak frequency with the peak frequency of the equilibrium solid CO_2 for which the temperature is known, one may estimate the temperature of the cluster. The legitimacy of this comparison is established by comparing the source conditions used in this experiment with conditions used in other reported CO_2 cluster experiments where the number of molecules per cluster is known. For example, Torchet *et al.*[92] reported that for stagnation pressures as

low as six atm., the number of molecules per cluster exceeded 1000 in an expansion of pure CO_2. Thus, in this experiment where the stagnation pressure is 27 atm, cluster sizes are expected to be well within the size regime where the cluster may be treated as bulk material.

From comparing the cluster and solid peak frequencies, the temperature of the cluster as a function of distance from the nozzle has been determined and is presented in Figure 4.8. This figure shows that even at X/D=1, solid CO_2 has already formed and has cooled from the reservoir temperature of 298 K to 152 K, fully 65 degrees below the triple point. This temperature drops further as X/D increases. Beyond X/D=9, the cooling rate slows until at X/D=20, the cluster has a temperature of 128 K. The CARS signal was very weak much past X/D=20, making temperature determination less certain, but the slope of the cooling curve approaches zero leading to a final temperature of ~120 K. This is consistent with the observation of Torchet *et al.*[92] who, using a similar jet expansion, estimated a final temperature of 108 ± 10 K for pure CO_2 clusters using electron diffraction. Moreover, Farges *et al.*[93] showed that the final temperature of a cluster in a pure gas expansion is approximately constant for a given molecule and is related to the well depth of the molecular pair potential. For CO_2, they calculate a final temperature range of 95-115 K, again consistent with our experimental observations.

The rate of cooling of the cluster is dependent on its size, suggesting that the mean size might be deduced by modeling the cooling curve. Attempts to do this were made, taking into account the several factors that alter the cluster temperature in the jet expansion. In the early part of the expansion many collisions occur

between monomers and clusters. Each collision that results in a monomer sticking to the cluster surface will warm the cluster an amount determined by the heat of sublimation and the heat capacity of the cluster. At the same time, since the cluster is warmer than the monomer due to previous condensation, a monomer-cluster accretion event will cool the cluster by an energy amount equal to $C_p\Delta T$, where C_p is the heat capacity of the monomer and $\Delta T = (T_{cluster} - T_{monomer})$. The temperature of the monomer can be calculated using the relationship between source temperature and the temperature in an isentropic expansion[94] at any distance from the nozzle tip. $T_{cluster}$ at any point in the expansion is obtained from a least-squares fit of the data in Figure 4.8.

Besides the collisions, some monomers are evaporating from the surface of the cluster, thereby removing heat. This heat loss is proportional to the surface area which is related to the overall size of the cluster. It is also dependent on the vapor pressure of the solid at the temperature of the cluster. If the cluster is large enough (>1000 molecules), size effects such as variations in the surface tension[95] and latent heat[96] on the thermodynamics of the cluster should play but a minor role in the rate of molecular evaporation.

If size effects are ignored, there are still several unknown variables in the problem. To accurately model the size of the cluster, it is necessary to know the fraction of collisions that result in a molecule sticking to the surface of the cluster (sticking coefficient f) and, further, the average amount of energy passed from the cluster to a monomer in a non-sticking collision.

These questions would be moot if the temperature could be modeled for a

region of the expansion far from the nozzle tip where the monomer cluster collision rate is small compared to evaporation. Such an approach was used previously by Beck *et al.* in modeling cooling of N_2 clusters[80]. Unfortunately in the case of our neat CO_2 expansion, the cluster temperature drops so quickly that the vapor pressure during much of the expansion is so low that the rate of evaporation is minute; hence, the cooling must occur primarily by noncondensing collisions of the colder monomer.

To explore the possible range of the cooling variables, the cluster diameter and the sticking coefficient were varied. The average amount of energy transfer in a non-sticking collision was assumed equal to $C_p\Delta T$. Using heat capacities[97], densities[98], and ΔH_{sub}[97] from the literature, the curves shown in Figures 4.9a and 4.9b were obtained. It was found that to approximate the experimental temperature vs. X/D data, the maximum fraction of collisions resulting in accretion is 0.16, regardless of cluster size. Larger fractions resulted in warming, not cooling of the cluster as X/D increased. A 0.16 sticking coefficient yields a mean cluster diameter of 30 nm, which, assuming a spherical shape, corresponds to ~3.2 x 10^5 CO_2 molecules. Note that at this extreme, the cooling rate close to the nozzle is not well approximated. At the other extreme, if f is greatly reduced to 0.001 for example, the cluster diameter giving the best fit of the data is 600 nm (Figure 4.9b), or 2.5 x 10^9 molecules. The principal conclusions therefore are that the clusters are larger in diameter than 30 nm and that no more than 16% of monomer-cluster collisions result in accretion.

Crystalline CO_2 clusters formed in dilute mixtures

Mixtures of 5% or 10% CO_2 in He were used in the other experiments examining solid CO_2 clusters in a free jet expansion. By using a dilute mixture, the clusters are cooled to a much greater extent than in the experiment using pure CO_2. In the mixture, most of the collisions are between helium atoms and the sample clusters and/or monomers so the internal energy of the cluster is transferred to the kinetic energy of the He. Figure 4.10 shows representative spectra taken at varying distances from the nozzle tip. The most significant feature of these spectra is that both the A_g and T_g mode peaks are visible, clearly establishing that the CO_2 clusters are <u>not</u> amorphous or glassy but have a well-ordered crystalline structure.

The other notable feature is the sharpening of the peaks at colder temperature. Thus, not only the peak frequency but also the peak width can be used to obtain an estimate of the cluster temperature. This was again done by comparison with the equilibrium solid CO_2 spectra taken at known temperatures and is illustrated in Figure 4.11. The lower curve shown in Figure 4.11 shows the cluster temperature as determined by the A_g peak frequency. This shows that in the less than one microsecond that it takes for the cluster to move from the nozzle exit to X/D=1, the cluster temperature has dropped to 78 K. Moreover, in this time period, the cluster has formed into a well-ordered crystalline structure as evidenced by the appearance of both the A_g and T_g mode peaks in the top spectrum of Figure 4.10.

The upper curve gives the temperature predicted by the A_g linewidth and it is apparent that this is consistently higher than the curve based on frequency

position. This is a consequence of an increased linewidth of the jet spectra compared with the equilibrium solid spectra at similar temperatures. That such might occur is understandable when one considers that there is surely a distribution in size and temperature of clusters formed. Near the nozzle, clusters of different size will experience different rates of cooling since the collision rate is proportional to the surface area of the cluster. In addition, the rapid rate of formation and cooling of the clusters may result in some broadening due to residual crystalline disorder. Modeling of the cooling curves to estimate a cluster size was not judged feasible for this experiment since one must consider both CO_2 and He collisions with the clusters. Again the question of how much energy on average is transferred per collision is not easily answerable.

Medium-sized CO_2 clusters formed in dilute mixtures

As was shown in Figure 4.6, several spectral features appear in between the monomer and the solid peaks in the $2\nu_2$ spectrum of a dilute mixture of CO_2 and He. These features were first observed in this group[78] in 1985, using a low resolution predecessor to our current high resolution CARS system. At that time, the peak least shifted from the monomer in frequency was attributed to the Q-branch of the $2\nu_2$ mode of the CO_2 dimer. Recently, Barth and Huisken[99] offered a reinterpretation of the group of peaks as the O-, P-, Q-, R-, and S-branches of this mode of the CO_2 dimer. This seemed unlikely to us since the isotropic Q branch normally dominates the Raman spectrum of most molecules. Thus, in order to better understand the origin of these peaks, several higher

resolution CARS spectra were obtained under a range of conditions.

It was first observed that the relative intensity of the peaks changed dramatically, depending on the source conditions, particularly the stagnation pressure. This can be seen in Figure 4.12, which shows representative spectra taken at a variety of source conditions. In spectrum (a), taken with relatively mild source conditions that would favor the formation of small clusters, only the highest frequency peak of the intermediate group appears. The solid peak is missing and two sharp monomer O-branch lines are visible, indicating that the monomer/cluster ratio is large. Spectrum (b) was taken at a higher source pressure which tends to increase the supersaturation ratio in the condensation zone of the jet expansion; hence more, and larger, clusters are expected to be formed. Indeed, the solid CO_2 peak is now visible and several new features in the intermediate region are apparent. Spectrum (c) was taken with a high driving pressure, a lower initial temperature, and a more concentrated mixture of CO_2 in He. All of these conditions favor the formation of large solid clusters as is manifest by the dominant solid peak which shows both the A_g and T_g mode peaks. Of the intermediate group of peaks, only the lowest frequency peaks are apparent in spectrum (c). It should be noted that the individual spectra in Figure 4.12 are normalized to show the detail of each trace. Experimentally, the CARS signal was several orders of magnitude weaker with the experimental conditions that produced spectrum (a) than with the conditions that produced spectrum (c).

The variation in the relative intensities of the intermediate features is clearly inconsistent with their assignment as O-, P-, Q-, R-, and S-branches of the dimer by

Barth and Huisken[99]. The trends also clearly suggest that those spectral features least red-shifted from the monomer are due to smaller CO_2 clusters, an observation that led to the assignment of the 1281.3 cm^{-1} feature to the Q-branch of $(CO_2)_2$ in the earlier work done in our group[78]. This also appears now to be incorrect, since in the current high-resolution studies, a group of new, sharp peaks immediately surrounding the monomer Q-branch have been discerned under even less-condensing source conditions and these seem more sensibly attributable to dimers and/or trimers, as will be discussed in the following chapter.

The possibility that this group of peaks between 1278 cm^{-1} and 1282 cm^{-1} is due to higher-order polymers, e.g., tetramers, pentamers, etc., was considered but deemed unlikely since such a progression of larger and larger polymers should lead to a continuum of peaks leading up to the solid crystalline peak. This is not observed, and in fact, there is a 1 cm^{-1} gap between the solid and the intermediate features that is totally void of any peaks.

Cluster surface modes

Another possibility is that the 1278-1282 cm^{-1} peaks arise from surface modes on a small cluster. It seems reasonable that molecules on the surface of a cluster will experience a slightly smaller environmental or matrix shift than those in the interior and will thus vibrate at a frequency closer to that of the monomer.

We considered a simple model of a spherical cluster with the outermost layer of molecules comprising a shell. By assuming that the 1278-1282 cm^{-1} peaks originate from this shell and that the solid peak accounts for the core molecules, it

is possible to calculate the ratio of surface molecules to core molecules. This is done by assuming that the Raman cross-sections are the same for all CO_2 units and are additive. By measuring the ratio of the square root of the CARS intensity of the group of surface peaks to the solid peak, the total size and number of molecules in the cluster is then calculable.

For spectrum (c) in Figure 4.12, this calculation gives a cluster size of ~4000 molecules and a diameter of 3.5 nm. The ratio of surface peaks to core peaks is much higher in spectrum (b) and in fact leads to a cluster size estimate of ~58 molecules and a diameter of 0.85 nm. In spectrum (a), no solid CO_2 peak can be seen implying that virtually all of the molecules are on the surface of the cluster. This would be consistent, for example, with a hexagonal close-packed 13-molecule structure with 12 molecules on the surface and one molecule in the core.

Of course, the larger the cluster, the smaller is the relative number of surface molecules to bulk molecules. Thus, under expansion conditions that favor large clusters, e.g., high p_0, pure CO_2 sample, the intensity of the surface Raman vibrational peaks should be minimal compared to that of the bulk peaks. Indeed, no intermediate peaks were observed in the pure CO_2 expansion experiments described above.

Support is lent to this surface-core postulate by a study of the vibrational predisocciation spectra of nitrous oxide clusters by Miller *et al*[100]. In that study, the $\nu_1 + \nu_3$ infrared spectrum and mass analysis of a jet expansion of a mixture of N_2O (typically 15% in He) was obtained for source pressures ranging from 3 atm to 34 atm. As the source pressure is increased, a clear progression of peaks from

the monomer to the solid peaks is observed as in our experiments. This is shown in Figure 4.13a, which was taken from reference 104. From simultaneous mass analysis of the clusters, it is seen that a spectral feature coincident in frequency with the monomer peaks originates mostly from the N_2O dimer when the source pressure is $\leq$4 atm. The solid spectral peak appears at source pressures $\geq$ 8.5 atm; at this pressure, the cluster size estimated from mass analysis is 20-60 monomer units. Finally, at 18 atm, the dominant spectral feature is that of solid N_2O and the cluster distribution peaks at $(N_2O)_{50}$.

In the same study a Monte Carlo simulation of the spectra of $(N_2O)_2$, $(N_2O)_{55}$ and solid N_2O (see Figure 4.13b, also taken from reference 104) showed that the experimental low source pressure expansion spectral peaks could be reproduced with a simulated dimer spectrum. The experimental intermediate cluster spectra were well simulated with a 55 molecule model. In these intermediate cluster spectra, three distinct absorptions are observed. Miller and coworkers attribute the two lower frequency peaks to surface molecules and the upper peak to core molecules. The shift to higher frequencies with larger cluster size is opposite the trend observed in CO_2 but this has been explained on the basis of the difference in the dipole moments of the two molecules. In CO_2, when the molecule is distorted, it obtains a small dipole moment. This dipole moment will cause an increased attraction to neighboring molecules, causing a shift to the red. A distortion of the N_2O molecule would cause a decrease in dipole moment, thereby weakening interactions with neighboring molecules, causing a shift to the blue[100].

These N_2O results are relevant to the current work on CO_2 for many

reasons. First, N_2O and CO_2 are very much alike. For example, both have similar second virial coefficients, similar lattice energies and a cubic crystalline structure with approximately the same lattice parameters. Furthermore, their quadrupole moments are nearly identical. Second, that a similar trend in the appearance of new spectral peaks with increasing pressure is observed for both molecules suggests that the origin of these peaks is the same. Since Miller *et al.*[100] experimentally established an N_2O cluster size range of 2-60 molecules under source conditions comparable to those used in this experiment, we might expect that the peaks seen in our spectra also originate from clusters in this size range.

Another piece of evidence supporting the core-surface model is found in the recent molecular dynamics study reported by Cardini *et al.*[101] In that study, the infrared spectrum of the ν_3 antisymmetric stretch was calculated for CO_2 clusters ranging in size up to 164 molecules. Figure 4.14 is taken from Cardini *et al.*[101] and shows the CO_2 ν_3 spectrum as calculated for various size clusters at 90K. The lower, narrow peaks in Figure 4.14 a-d are calculated with a Pa3 crystalline model while the upper peaks are inhomogeneously broadened versions of the narrow peaks and represent liquid-like clusters that originated with the Pa3 structure. In this simulation, it was postulated that the positive-frequency shifted peaks arise from core-type molecules and the negative-frequency shifted peaks arise from surface-type molecules. In the bottom figure labeled Experimental Spectra, the 116 molecule liquid-like calculated spectrum (lower trace) is compared with a smoothed experimental FTIR spectrum of a jet expansion of a 2% mixture of CO_2 in Ar taken by Barnes and Gough[102] (upper trace). The temperature of the clusters

in the experimental work was estimated to be 90K although the number of molecules was not directly known. The similarity in appearance of the two spectra is remarkable and again gives credence to the idea that peaks arising from the vibration of surface molecules on small clusters may be distinguishable from those originating from core molecule vibrations.

Icosahedral cluster structure

Another interesting alternative explanation of the 1278-1282 cm^{-1} peaks was considered in light of a study by van de Waal[103] wherein the most stable structure of small molecular clusters was calculated. In the case of CO_2, it was found that there was no barrier to rearrangement between a cubic arrangement of 13 CO_2 molecules and a regular 13 molecule icosahedron and that the icosahedral arrangement was actually energetically more favorable (E = -114.6 kJ/mol for the icosahedron vs. -100.5 kJ/mol for the cubic arrangement). It was postulated that in light of this lack of energy barrier, a 55-molecule cubic CO_2 cluster consisting of two coordination shells rather than one might also be intraconvertible with an icosahedral structure without a potential energy barrier in between. The energy difference between the two structures would probably be smaller than the 13 molecule case, and as more shells are added would change sign due to the growing, energetically unfavorable space deficit that is inherent in the icosahedral arrangement. Eventually, the icosahedral structure becomes unstable with respect to the crystalline structure; hence only the crystalline form would exist in large clusters.

In the case of rare gas atomic clusters, Lennard-Jones potential energy calculations have shown that 13- and 55-atom clusters spontaneously rearrange to form icosahedra[104]. Experimentally, Farges *et al.*[93] observed that argon clusters show three different structures, depending on the number of atoms: polyicosahedral for $N < 50$, multilayer icosahedral for $50 < N < 800$, and crystalline fcc for $N > 800$ atoms. The extent to which one may apply these results to a cluster of decidedly aspherical CO_2 molecules is unclear and in fact, electron diffraction data exist that suggest that CO_2 clusters as small as 100 molecules have a cubic crystalline structure[92].

Nevertheless, if small icosahedral CO_2 clusters are formed in a jet expansion, they should be manifest in a vibrational Raman spectrum as peaks at a slightly different frequency than the cubic crystalline peak since nearest neighbor interactions will differ in the two structures. The implications for the possible interpretation of our spectra are as follows. The sole cluster peak seen under mild expansion conditions, as shown in Figure 4.12 (a), may arise from a 13-molecule icosahedron. No peak is observed at the frequency of cubic crystalline CO_2 suggesting that perhaps all of the 13-molecule crystalline clusters have rearranged to the energetically favorable icosahedral structure. The other intermediate peaks that appear with more moderate expansion conditions as shown in Figure 4.12 (b) may be due to multilayer icosahedra that coexist with the cubic form. Finally, under the harsh expansion conditions of Figure 4.12 (c), the remaining intermediate peak may be due to the largest icosahedral CO_2 cluster that is stable with respect to the cubic solid. The observation that no intermediate peaks appear in the spectra of

pure CO_2 expansions is also consistent with the icosahedral cluster model since only the cubic crystalline form should exist under conditions that favor very large clusters.

With the experimental data at hand, either the surface-core or the icosahedron explanations appear possible. However, more evidence, both experimental and theoretical, point to the surface-core model as the correct explanation of the intermediate peaks in the $2\nu_2$ CO_2 cluster spectrum.

CONCLUSIONS AND SUGGESTIONS FOR FUTURE WORK

CO_2 clusters of a variety of sizes have been formed and observed in a free jet expansion. The temperature of the clusters formed in an expansion of pure CO_2, as deduced by comparison with spectral data taken of equilibrium solid CO_2, ranges from 152K to 128K with an estimated final cluster temperature of 120K which agrees well with other experimental and theoretical observations. In expansions of CO_2 in He, both the T_g and A_g modes of the solid CO_2 vibration are visible, confirming the crystallinity of the cluster. Furthermore, a group of peaks appears in the spectrum between the monomer and solid peaks, the intensity of which is highly sensitive to source conditions. These intermediate peaks are believed to arise from small clusters, possibly from surface modes or from a different crystal arrangement.

In future work, it would be instructive to concomitantly examine CO_2 clusters using both spectroscopic and mass analysis techniques to gain a clearer picture of the size of clusters that give rise to the various features in the vibrational spectrum.

It would also be beneficial to develop an accurate inline gas mixing apparatus so that the proportion of sample to diluent could be accurately controlled. By learning to control the source conditions well enough to repeatably create clusters of a narrow size range as determined through mass analysis, it should be possible to learn more of the cluster growth process as well as thermodynamic size effects.

Table 4.1: Transition frequencies and linewidths for the $2\nu_2$ mode of solid CO_2.

Crystal Temperature	A(g) cm^{-1}	T(g) cm^{-1}	A(g) linewidth FWHM cm^{-1}
7.6	1275.371	1275.744	0.040
15	1275.366	1275.738	0.038
22	1275.362	1275.741	0.037
29	1275.379	1275.753	0.050
36	1275.389	1275.764	0.055
43	1275.408	1275.778	0.063
50	1275.442	1275.809	0.067
63	1275.522	1275.882	0.082
73	1275.578	1275.931	0.147
83	1275.644	1275.995	0.180
93	1275.715	1276.071	0.254
103	1275.804	1276.136	0.300
113	1275.880	1276.209	0.308
123	1275.966	1276.294	0.267
133	1276.057	1276.354	0.347
143	1276.150		
153	1276.254		
163	1276.364		
173	1276.464		
183	1276.553		
193	1276.667		
203	1276.811		
213	1276.907		
217	1276.949		

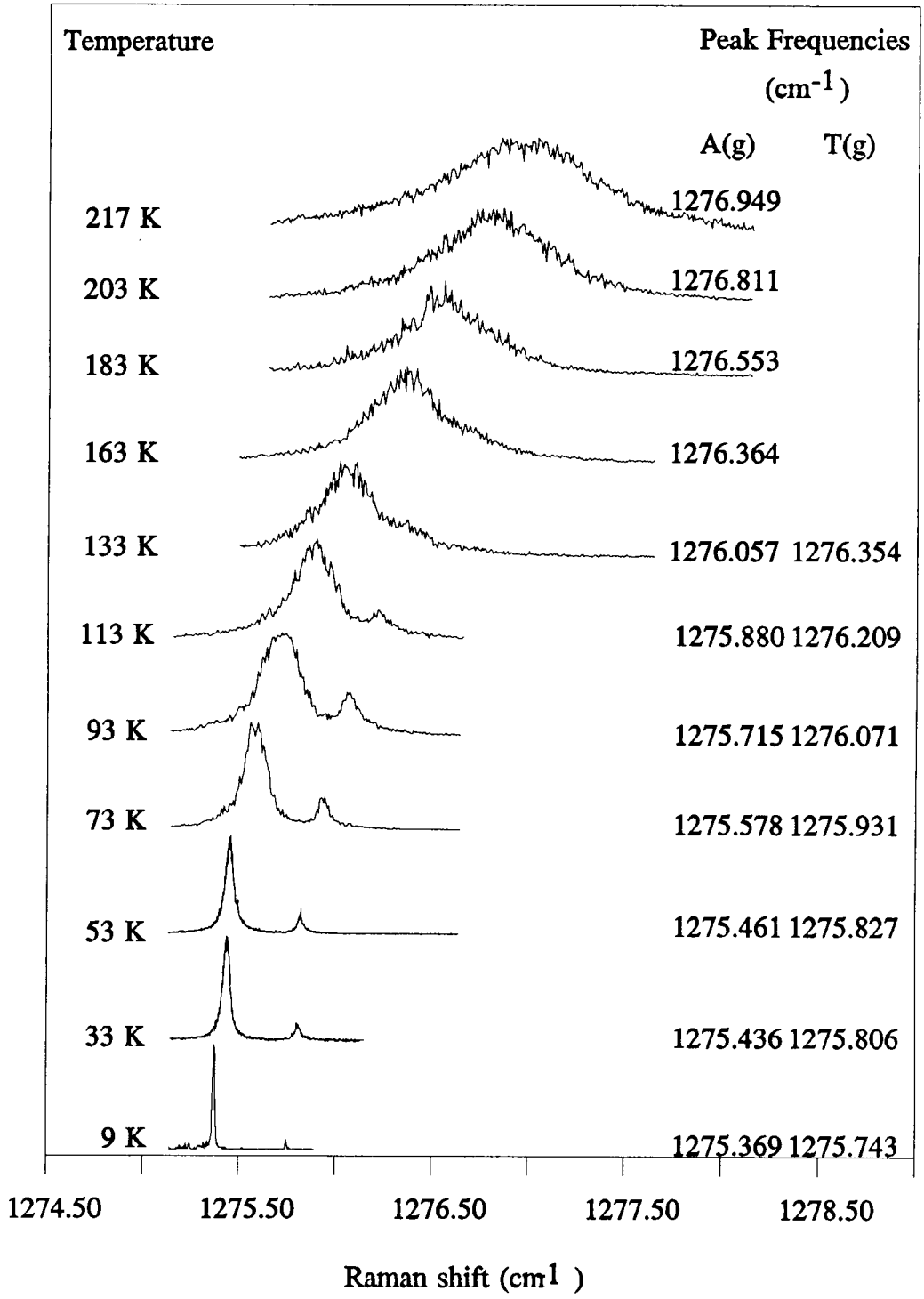

Figure 4.1: CARS spectra of the $2\nu_2$ mode of solid CO_2 at various temperatures.

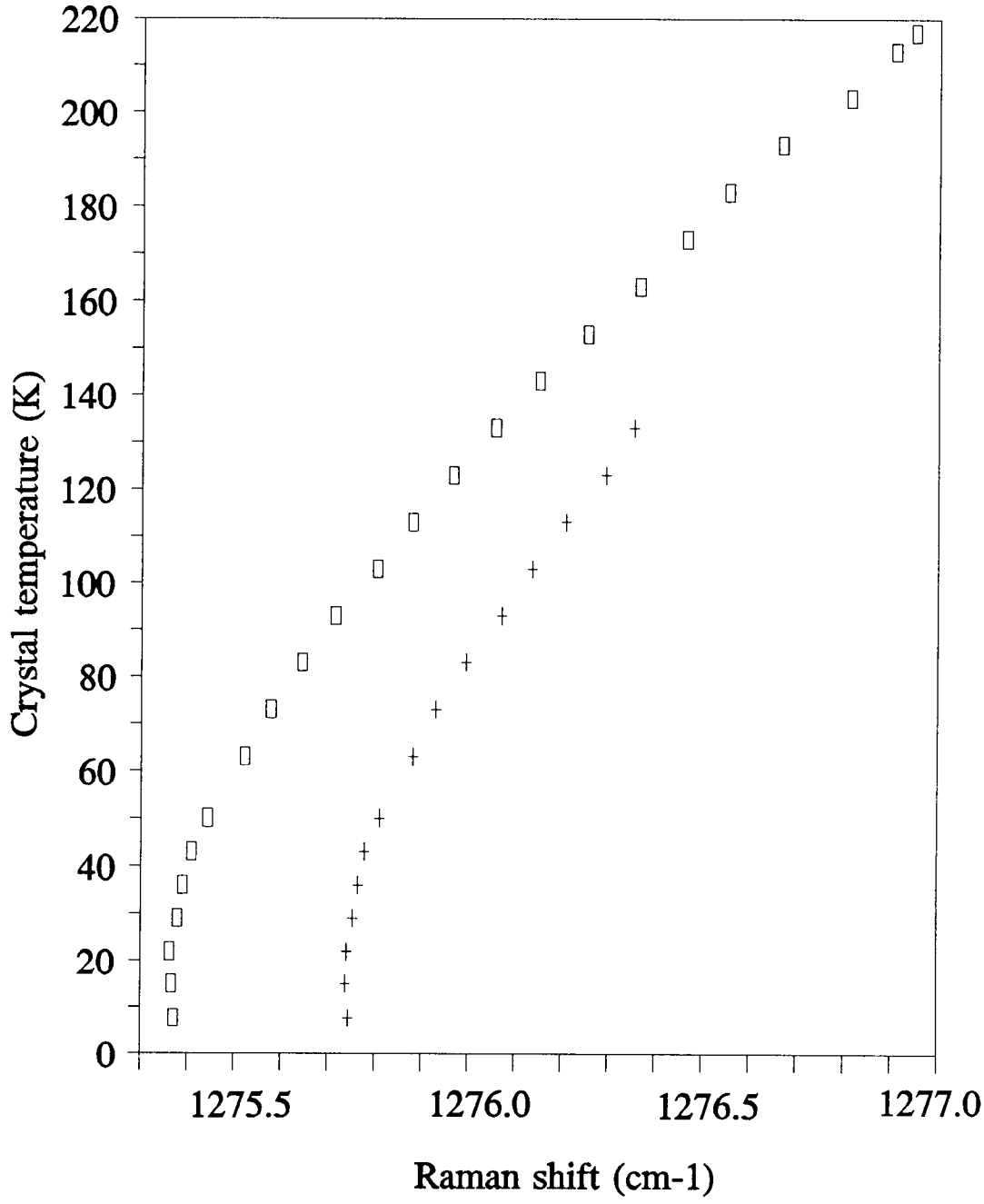

Figure 4.2: Temperature vs. peak frequency for the A_g (□), and T_g (+) $2\nu_2$ mode of solid CO_2.

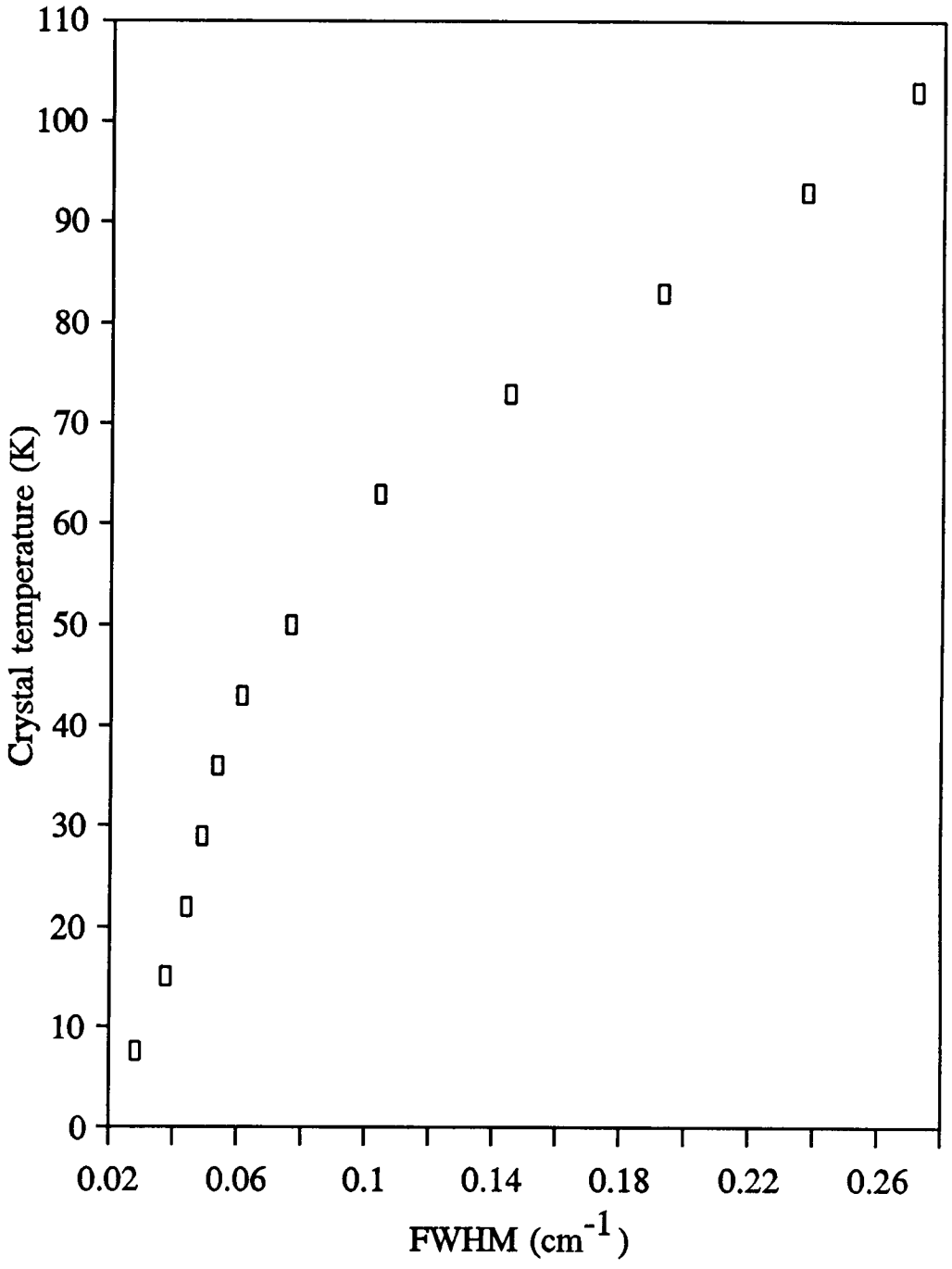

Figure 4.3: CO_2 crystal temperature vs. linewidth (FWHM) of the A_g mode.

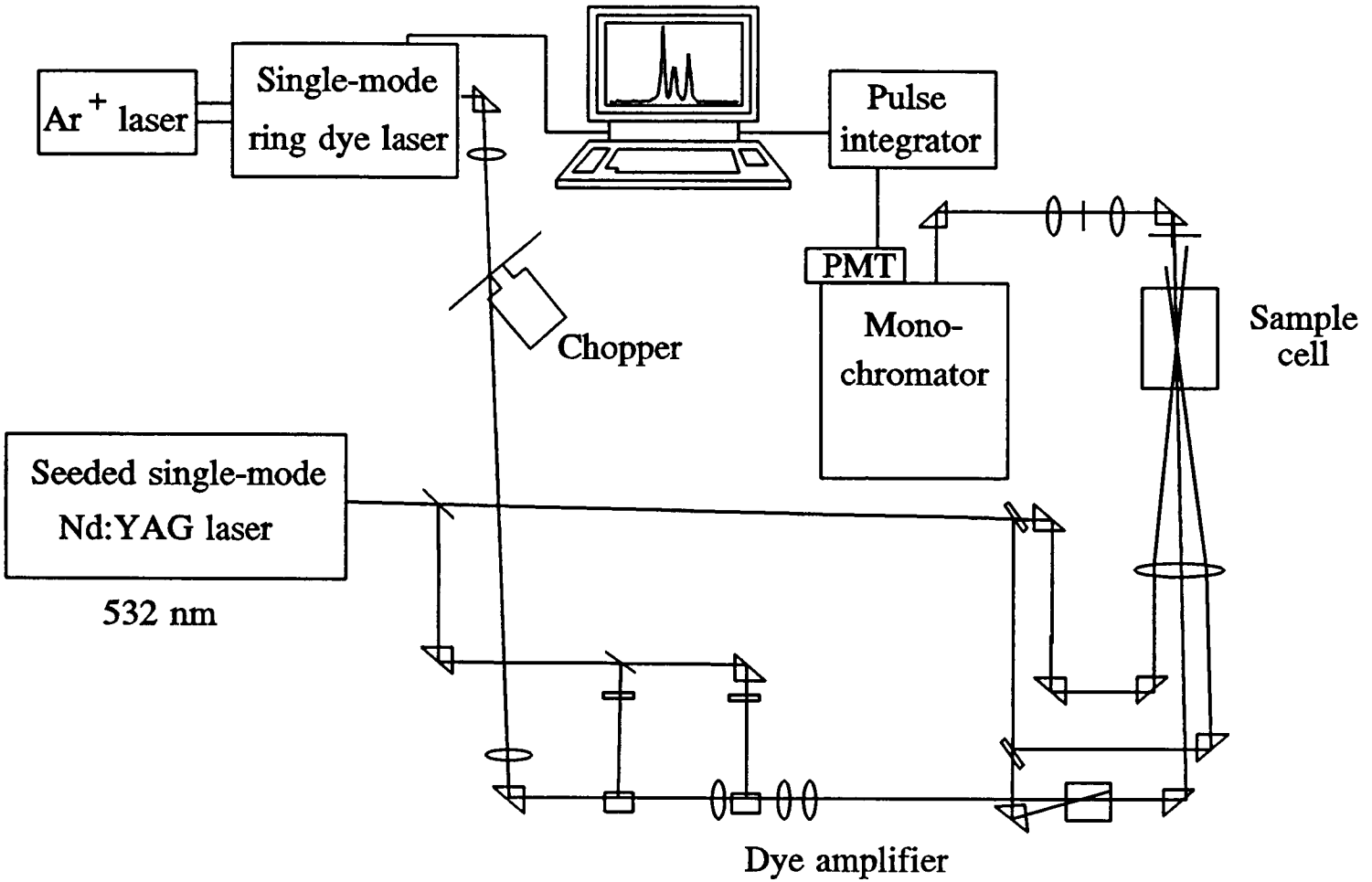

Figure 4.4: CARS spectrometer setup used for studies of CO_2 clusters and solid.

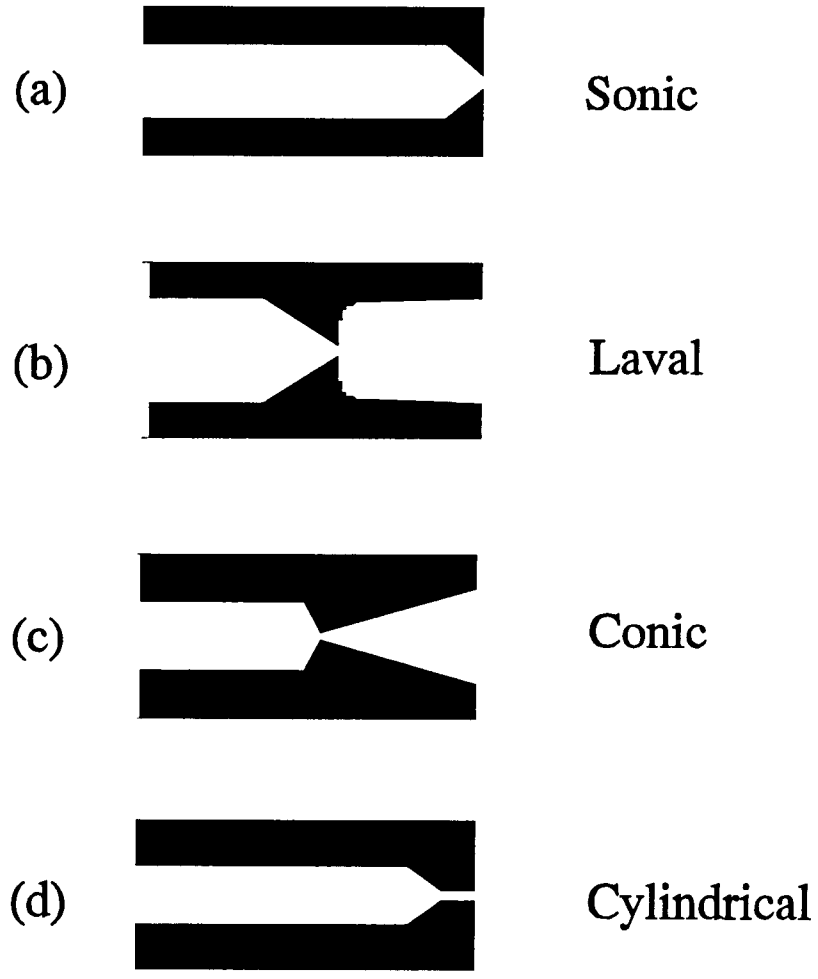

Figure 4.5: Cross sections of various nozzle geometries. A sonic nozzle was used for all experiments reported here except for the CO_2 neat expansion study in which a cylindrical nozzle was employed.

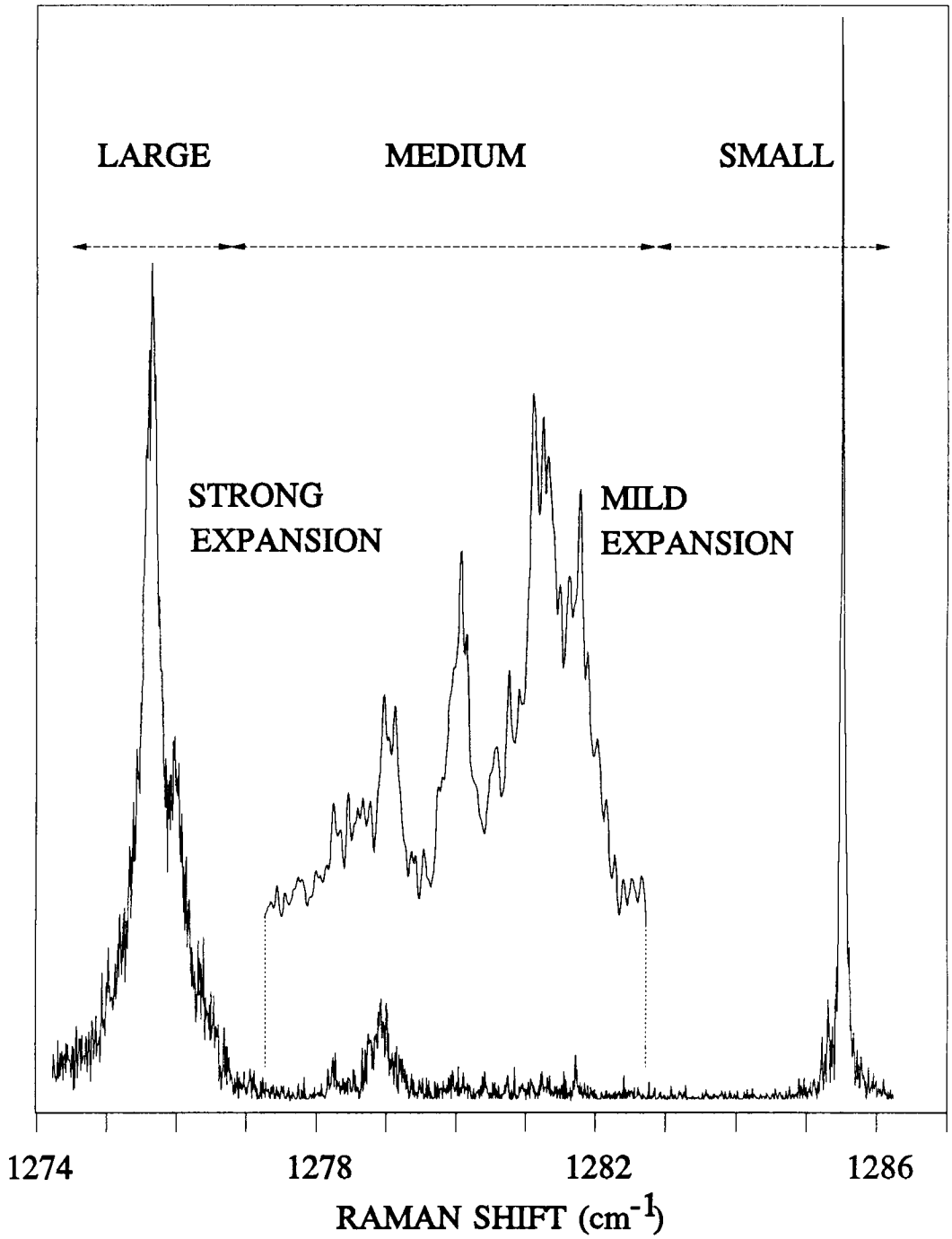

Figure 4.6: Representative spectra of the $2\nu_2$ vibration of CO_2 illustrating the spectral regions where peaks arising from various size clusters are found. The sharp peak at the right is the Q-branch of the monomer.

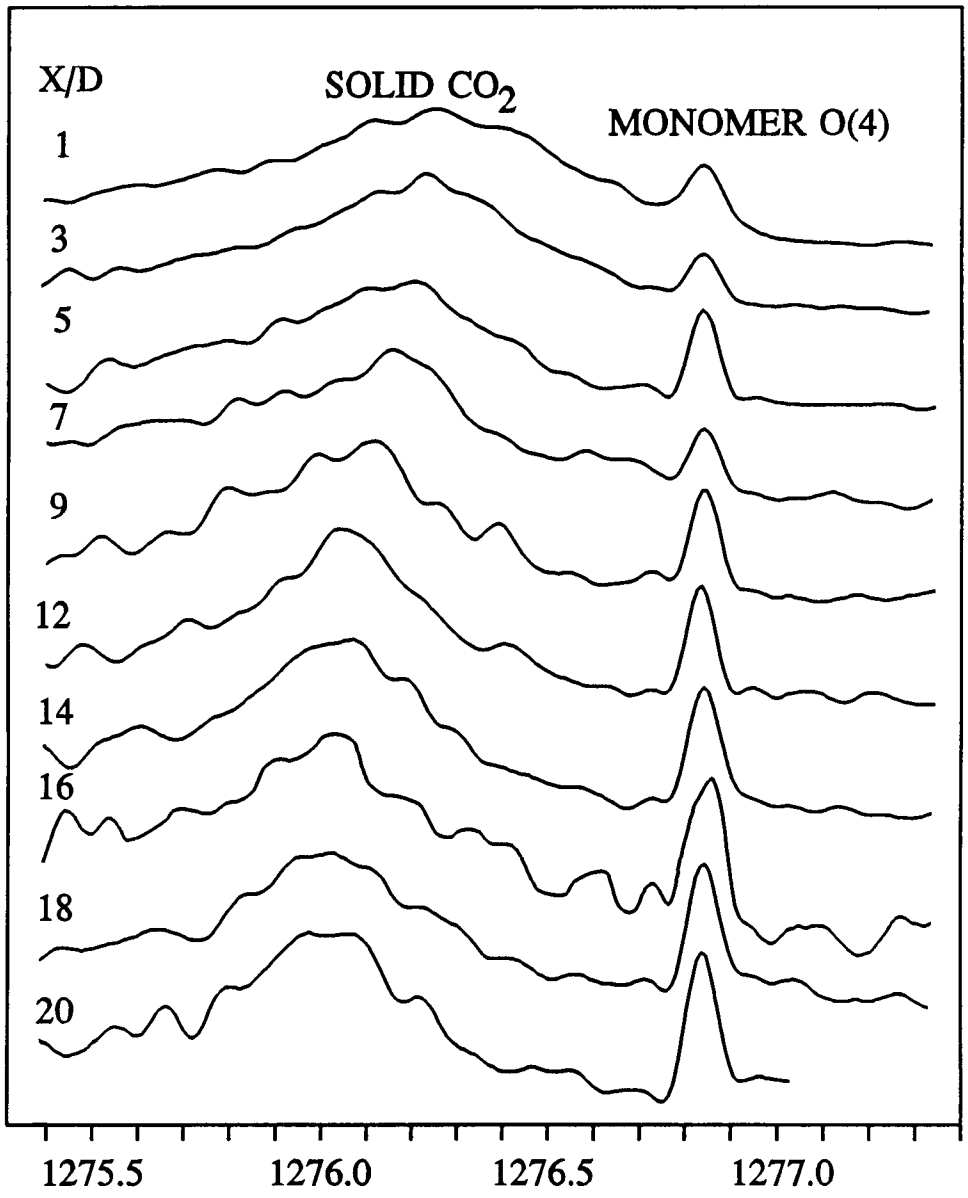

Figure 4.7: CARS spectra of the $2\nu_2$ mode of solid CO_2 formed in a pure free jet expansion.

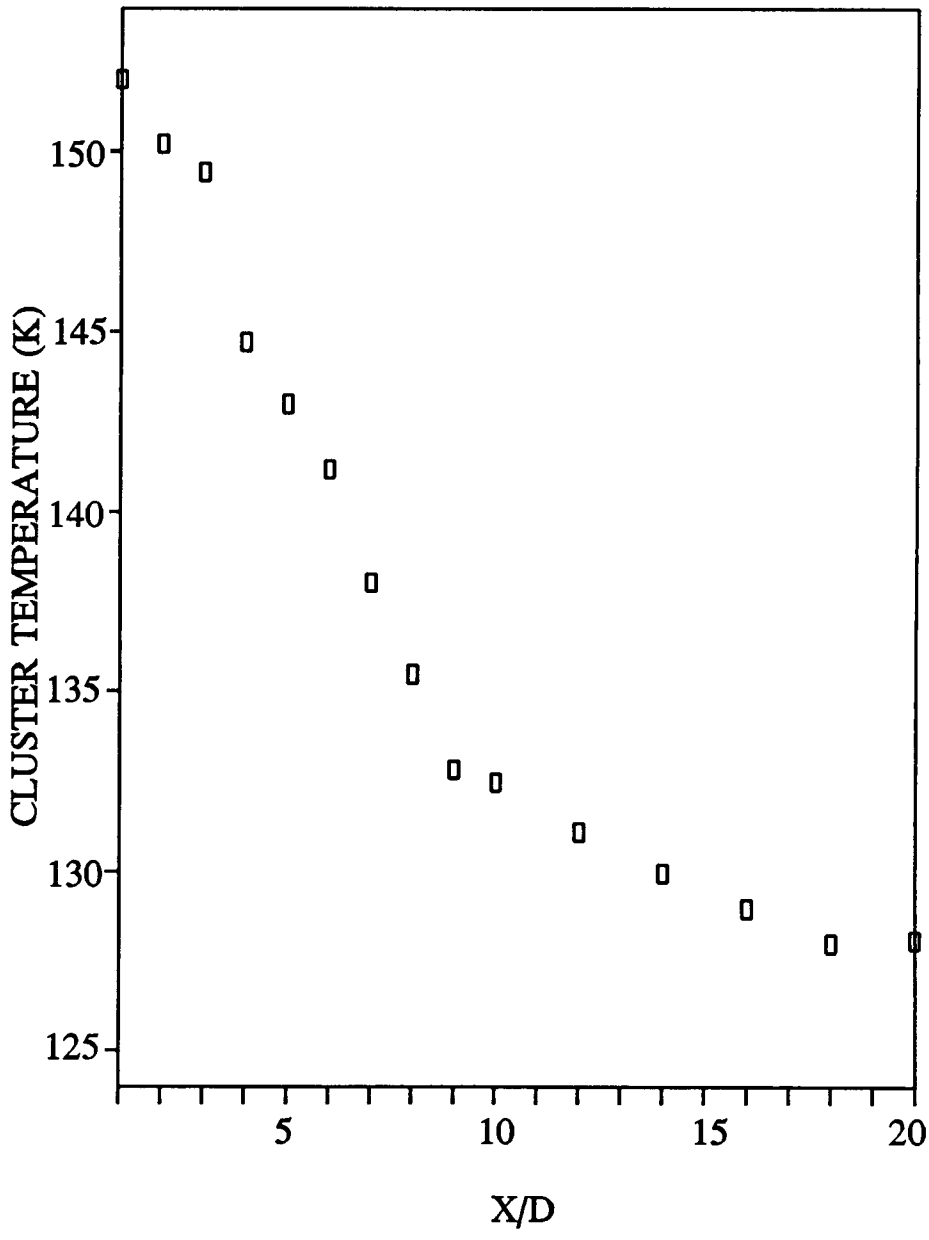

Figure 4.8: Estimated temperature of clusters as a function of X/D for a neat expansion of CO_2 with p_0 = 27 atm and T_0 = 298K.

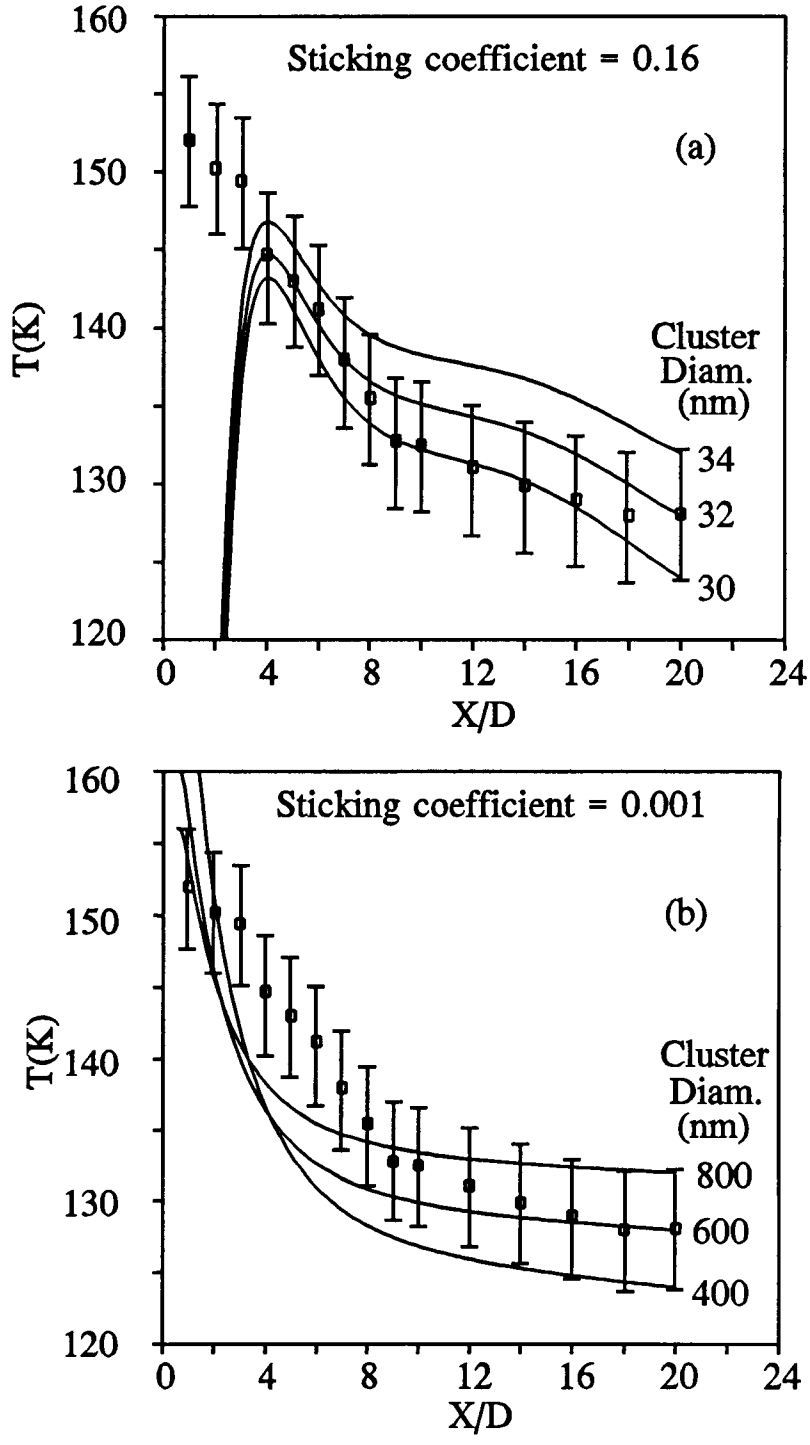

Figure 4.9: Modeling of experimental CO_2 cluster cooling (□) in a free jet expansion. Two extremes of 0.16 and 0.001 sticking coefficient are presented in (a) and (b) respectively.

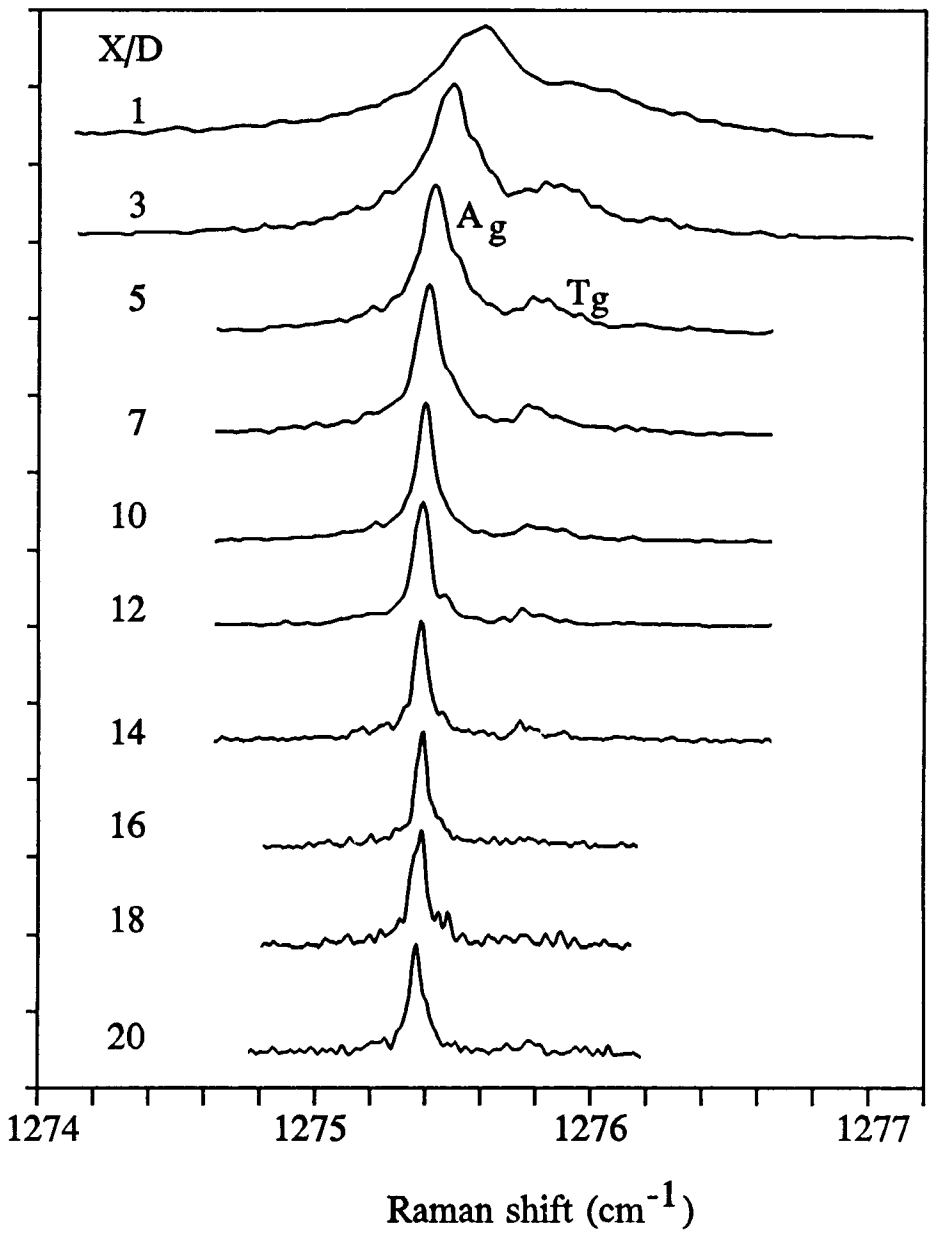

Figure 4.10: CARS spectra of the $2\nu_2$ mode of solid CO_2 as seen in a free jet expansion of 10% CO_2 in He.

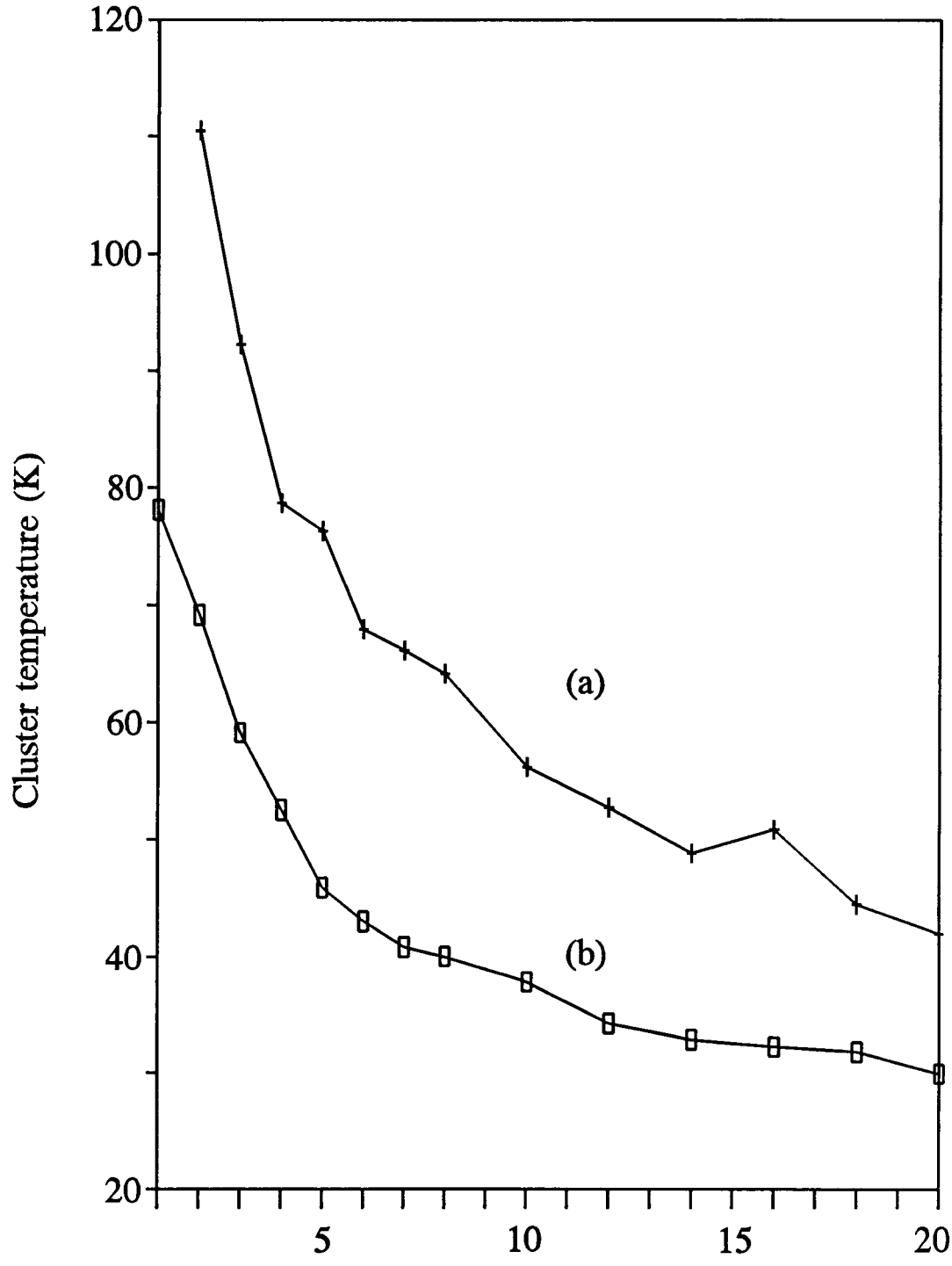

Figure 4.11: Temperature of solid CO_2 clusters formed in an expansion of 10% CO_2 in He as deduced by comparing (a) A_g FWHM and (b) A_g peak frequency with equilibrium spectra.

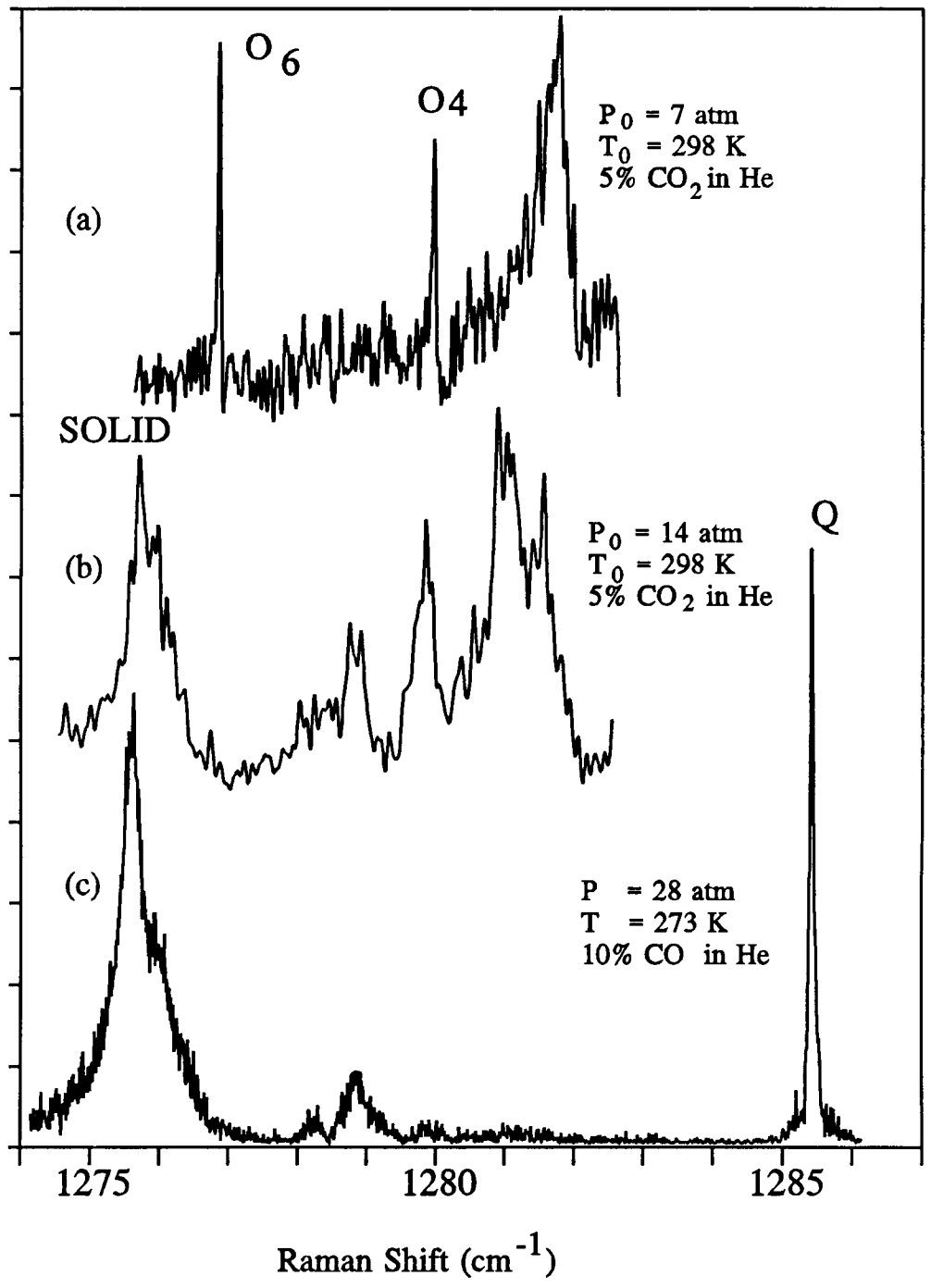

Figure 4.12: $2\nu_2$ spectra of CO_2 under different source conditions, all at X/D=3.

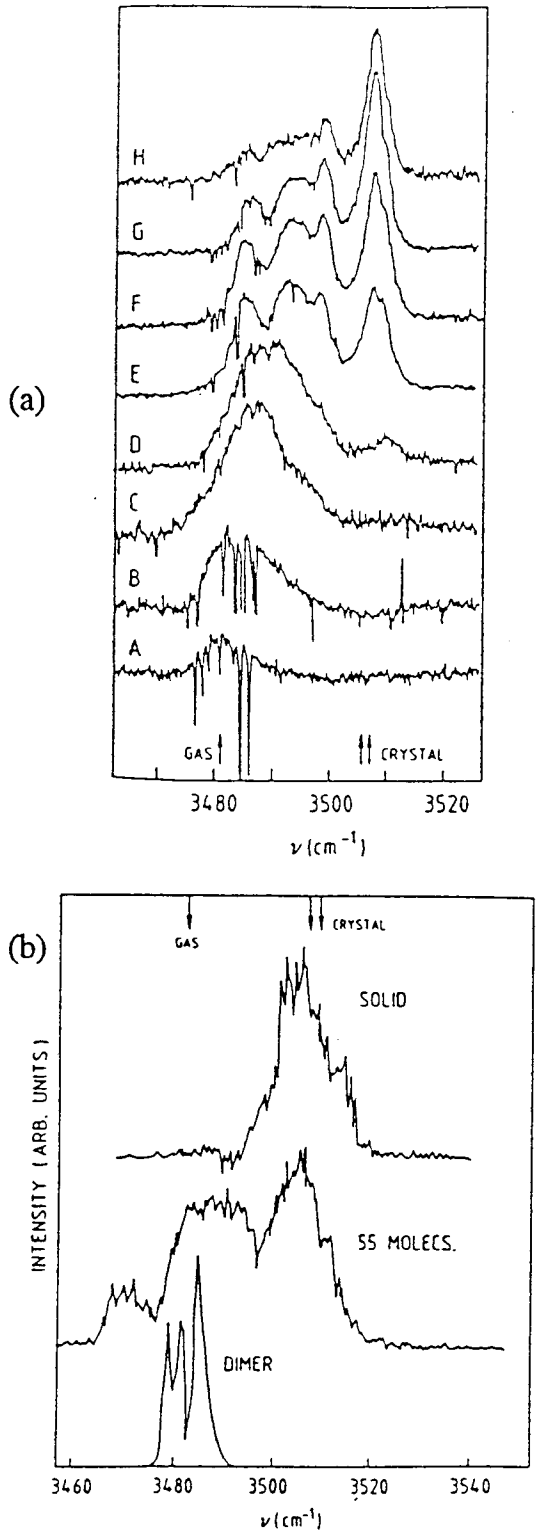

Figure 4.13: From Miller *et al.*[104], spectra of N_2O in free jet expansions. (a) Source pressures and gas compositions (%N_2O in He): A. 3.1 atm (15%) B. 4.3 atm (15%) C. 4.8 atm (15%) D. 8.5 atm (15%) E. 14.5 atm (15%) F. 17.8 atm (15%) G. 23.7 atm (15%) H. 34.1 atm (45%). The negative going peaks in A and B are the monomer absorptions. (b) Also from Miller *et al.*[104], Monte Carlo simulated N_2O cluster spectra.

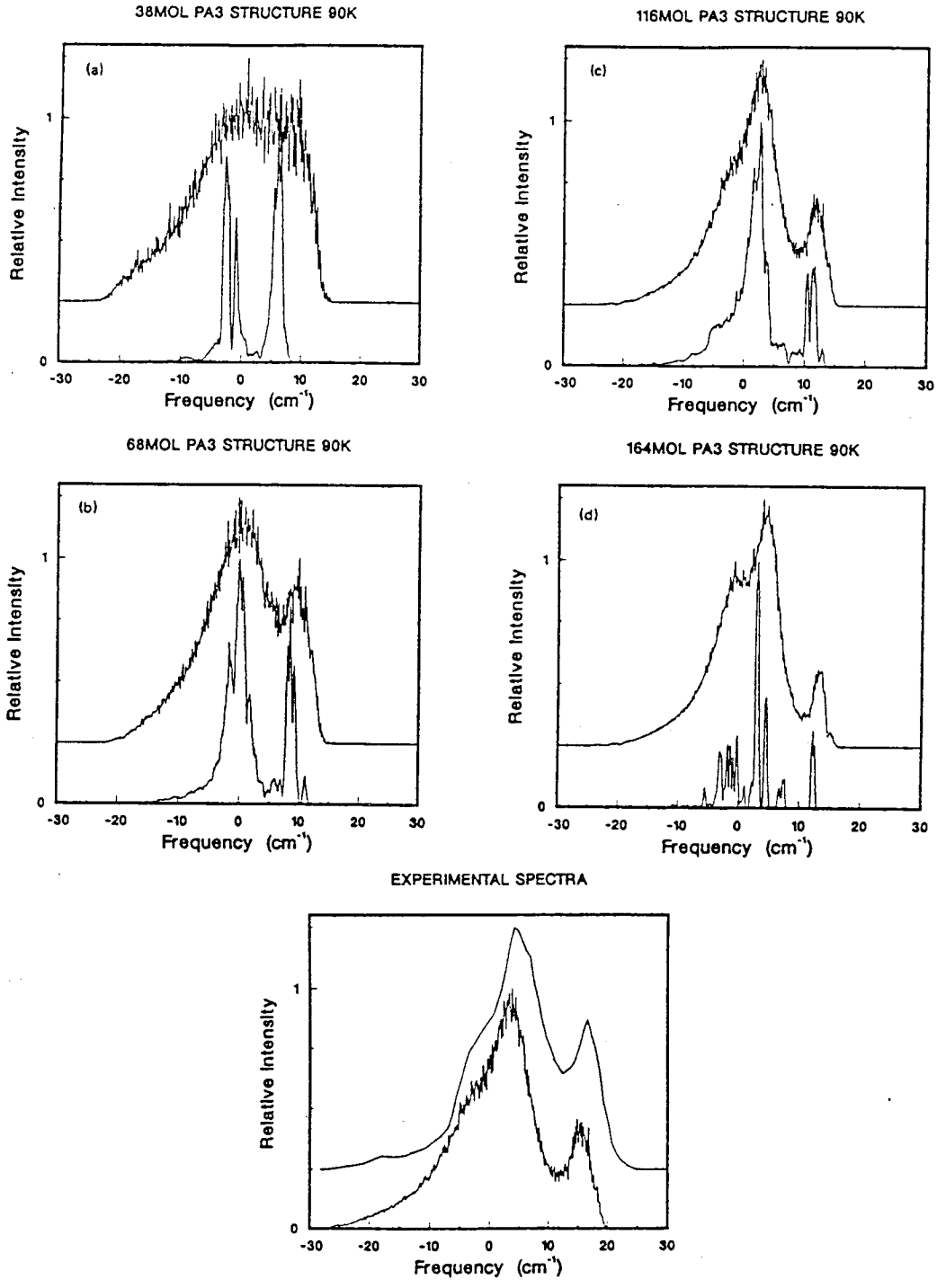

Figure 4.14: Calculated CO_2 cluster ν_3 spectra from Cardini *et al.*[18] (Figs. a-d). The experimental spectrum in the bottom figure (upper trace) is from Barnes and Gough[19].

CHAPTER 5 THE CARS SPECTRA OF CARBON DIOXIDE DIMER

INTRODUCTION

The smallest of all carbon dioxide clusters, $(CO_2)_2$, has been the subject of many experimental and theoretical studies for the past two decades, with considerable debate in the literature centering on the CO_2 dimer structure. Some early studies found that the most likely structure was a polar T-shaped dimer[105,106,107,108,109] while other results suggested that a C_{2h} offset parallel structure was the more stable form[110,111,112,113,114,115]. Recently, however, the infrared spectra of the ν_3 fundamental mode[116] and of the $\nu_3+2\nu_2$, $\nu_3+\nu_1$ Fermi diad[117,118] were resolved and interpreted to obtain rotational constants and structural parameters that definitively confirm the offset parallel structure.

The search for the Raman active $(CO_2)_2$ transitions has centered primarily on a series of spectral features red-shifted 3-7 cm^{-1} from the CO_2 monomer Q-branch of the lower component of the ν_1, $2\nu_2$ Fermi diad, herein denoted $2\nu_2$. In work done in this group in 1985[78], a peak in the CARS spectrum at 1281.3 cm^{-1} was attributed to the CO_2 dimer, an assignment made in part due to the lack of observation of any other spectral features closer to the monomer Q-branch at 1285.5 cm^{-1}. Subsequently, this same peak has been assigned by Barth and Huisken[99] as one of a group of five peaks from 1278.2 to 1281.6 cm^{-1} that they

attribute to the rotational branches (O,P,Q,R,S) of the CO_2 dimer. It has also been attributed to $(CO_2)_2$ by Vigasin and Denisov[119] who have assigned five spectral features ranging from 1281 cm^{-1} to 1372 cm^{-1} to vibrational modes of the dimer.

In this work, we present high-resolution CARS spectra showing new, regular, well-resolved peaks surrounding the monomer Q-branch of the upper ν_1, $2\nu_2$ component, (ν_1). We attribute these peaks to rovibrational transitions of $(CO_2)_2$, marking the first observation, to our knowledge, of a rotationally resolved CARS spectrum of a molecular dimer. The assignment of these peaks to specific transitions is difficult, however, due to many factors that effect the spectrum. In the following sections, the experimental conditions, spectral results and analysis will be presented.

EXPERIMENTAL

The CARS spectrometer and pulsed jet assembly were identical to that used for the study of larger clusters of CO_2 (see Chapter IV). Several different dilute mixtures of CO_2 in a driving gas were tested, with a range of 2-6% CO_2 in either neon or helium proving satisfactory for the spectral observation of the $(CO_2)_2$ peaks. The sample pressure behind the room-temperature 0.2 mm diameter nozzle was varied between 1.0 and 7.0 atm with the lower pressures resulting in more clearly resolved spectra.

These conditions are consistent with the formation of very small clusters and with the conditions reported by other groups who have successfully observed the

CO_2 dimer. For example, Jucks *et al.*[118] expanded a mixture of 10% CO_2 in He through a 0.04 mm nozzle with a stagnation pressure of 2 atm in their study of the $\nu_3 + 2\nu_2$ infrared dimer spectrum and Buck *et al.*[120] used 1% or 5% CO_2 in Ne with 3-4 atm stagnation pressure with a 0.1 mm nozzle in a study of deflection of small CO_2 clusters by a He beam. Walsh *et al.*[116] detected significant dimer formation using a 0.35 mm nozzle with a backing pressure of 3 atm of 3% CO_2 in Ne.

Jet source conditions can be compared using the model of "corresponding jets" developed by Hagena[85,121]. In this model, the mean size of a cluster formed in a jet expansion remains constant if the source pressure p_0 and the source temperature, T_0 are increased simultaneously according to the isentropic relation $p_0 T_0^{\gamma/(1-\gamma)} = \text{const.}$ Furthermore, the model predicts that for jet nozzles of similar geometry (i.e. sonic, laval, conical, etc.) a decrease in nozzle throat diameter d can be compensated by an increase of source pressure p_0 such that $p_0 d^q = \text{const.}$ with $0<q<1$. For CO_2, it was found[121] that $q = 0.6$. Without considering the effect of the different mixtures and different nozzle types used by the other groups who observed CO_2 dimers[116,118,120], we can make a first-order approximation of the pressure needed to form dimers using our 0.2 mm diameter nozzle by comparing p_0 and d. This comparison suggests an optimal source pressure range of 0.76 - 4.2 atm which does in fact overlap the set of conditions used in obtaining the spectra presented in the following section.

RESULTS

Figure 5.1 and 5.2 show CO_2 cluster spectra obtained using a mixture of 2% CO_2 in Ne as a function of distance from the nozzle at a source pressure of 2 atm and 1.6 atm respectively. The broad feature in the center of the spectra is the CO_2 monomer Q-branch, which, it should be noted, exhibits no resolvable rotational structure due to an unusually small $\alpha = B_0\text{-}B_1$ vibration-rotation constant for this diad member. This arises because of a cancellation of inertial changes for the nearly equal stretch and bending coordinates. In fact, line spacing in the monomer Q-branch varies[122] between 10^{-4} cm^{-1} (for J=0, J=2) and 10^{-3} cm^{-1} (for J=10, J=12). In work done earlier in this laboratory by George Pubanz[89] using high resolution stimulated Raman spectroscopy, the entire width of the CO_2 ν_1 Q-branch in a jet expansion of 5% CO_2 in He at 14.6 atm backing pressure was measured to be 0.0047 cm^{-1} (FWHM); hence, none of the surrounding sharp features can be attributed to CO_2 monomer Q-branch lines.

Examination of Figure 5.1 and 5.2 reveals a set of somewhat regularly-spaced peaks reproducible in frequency from scan to scan. The most dominant cluster peaks are indexed in the top spectrum of Figure 5.1. The overall intensity envelope does not shift appreciably with decreasing temperature (increasing X/D) although the intensities of the individual peaks vary somewhat. Each of the spectra is shown with the monomer peak off-scale in order to magnify the cluster features, but by measuring the relative intensity of the group of cluster peaks vs the actual intensity of the monomer peak, the extent of clustering is estimated to be less than 15%.

The average frequency of peak #9, which was prominent in virtually all sixteen of the spectra used in this analysis, was used as a calibration point and each spectrum was shifted a small amount (<0.005 cm^{-1}) so that the frequency of peak #9 matched exactly in each spectrum. This is to compensate for a small drift in the Nd:YAG frequency from day to day. The frequencies of the dominant peaks in each spectrum were then tabulated, indexed and averaged. These average frequencies are presented in column 1 of Table 5.1 with their respective standard deviations listed in column 2, while the peak-to-peak separations are listed in column 3. The data show 23 peaks, separated by an average of 0.050(5) cm^{-1}. Significantly, there appears to be no trend in increasing or decreasing peak-to-peak separations across the spectrum. This near regularity is surprising considering the complicated nature of the system, and we examine in the following section various possible sources for this spectrum.

DISCUSSION AND ANALYSIS

As illustrated in Figure 5.3, the CO_2 dimer has a slipped parallel structure with a C---C distance of ~3.6 Å and an angle of ~58° between the C---C axis and the CO_2 internuclear axis[118]. Table 5.2 summarizes the vibrational-rotational data known from IR studies for the ground and several excited states. The dimer is a near prolate top (κ = 0.94) with A being the unique rotational axis. Due to the orientation of A, both parallel and perpendicular rovibrational transitions are allowed; hence, $\Delta J = 0, \pm 1, \pm 2$ and $\Delta K = \pm 1$ as well as $\Delta K = 0, \pm 2$ transitions could be observed in the Raman spectrum. However, the strengths of the $\Delta J \neq 0$,

$\Delta K \neq 0$ bands depend on the polarizability anisotropy while the $\Delta J = 0$, $\Delta K = 0$ Q-branch depends mainly on the isotropic component of the polarizability. Preliminary calculations performed by Salvador Montero[123] after the manner described in reports by Montero[124] and Montero and del Rio[125] show that the ν_1 band of the CO_2 dimer is highly isotropic and that in fact, the CARS intensity of the anisotropic O-, P-, R-, and S-branches will be less than 1% of the intensity of the Q-branch. Also, the $\Delta K = \pm 1$, $\Delta K = \pm 2$ Q-branch lines are expected to be weak and hence only isotropic $\Delta J = 0$, $\Delta K = 0$ lines should be seen.

This was verified in this experiment by examining the ν_1 monomer/dimer spectrum with both parallel and perpendicular polarization orientations of the input CARS beams. In the perpendicular polarization experiment, dimer peaks arising from parallel transitions should totally disappear while spectral peaks originating from perpendicular transitions of the dimer should only be reduced by a factor of $(3/4)^2$. As shown in Figure 5.4, the monomer peak of this totally symmetric mode is greatly reduced and the dimer peaks are completely absent in the perpendicular polarization experiment, thereby confirming the parallel nature of the dimer transitions observed here. The conclusion from this is that in the prolate top approximation, the CARS spectrum should only exhibit a series of bands given approximately by

$$\nu_{JK} = \nu_0 - \alpha_B J(J+1) - (\alpha_A - \alpha_B)K^2. \qquad (5.1)$$

Another possible complication arises from the four low-lying intermolecular Van der Waals modes. From the centrifugal distortion constants of the CO_2 dimer, Jucks *et al.*[118] calculated harmonic van der Waals vibrational frequencies of 32(2)

and 90(1) cm^{-1} for the A_g "stretch" and "bend" respectively. Recent preliminary calculations by S. Montero[123] show that the harmonic frequencies of the other in-plane bend and the torsion are between 30 and 45 cm^{-1}. If the dimer vibrational transition originates not from the ground vibrational state but rather from one of the low-lying van der Waals levels, the resulting "hot-band" spectra may well overlap the spectrum of dimers originating from the ground state.

To explore the importance of hot-band contributions, thermal populations of the ground and the low lying Van der Waals states were calculated. In order to do this however, it was necessary to estimate a temperature of the sample. This was difficult since we cannot confidently assign any of the dimer transitions and since no monomer Q-branch or O- and S-branch structure was observed in these experiments to allow for an approximate rotational temperature determination. However, a lower bound to the temperature can be established from calculating the translational temperature of the sample in an isentropic expansion as described by Levy[94]. At a distance from the nozzle of X/D = 10, this calculation gives T_{trans} = ~5 K. An upper temperature bound of ~38 K can be estimated by noting the temperature of large CO_2 clusters at a similar distance from the nozzle as determined by comparison of the cluster vibrational frequency with that of bulk solid CO_2 (see Figure 4-11b). Since the dimer is surely colder than a large cluster that has warmed from many accreting collisions and is in all probability somewhat warmer than the translational temperature, we estimate the CO_2 dimer temperature range to be 10-30 K. At these temperatures, the square of the Boltzmann population factor (which is proportional to the CARS signal) of a van

der Waals state at $30cm^{-1}$ is less than 5%. Therefore, no appreciable CARS signal is to be expected from vibrations originating in any of the low-lying van der Waals states or their respective overtone levels.

Another complicating factor is the likelihood that the source conditions used here result in the formation of not only dimers but also trimers and other higher order clusters. Indeed, in an examination of the $\nu_3 + 2\nu_2$ infrared spectrum of the carbon dioxide trimer, Fraser *et al.*[126] observed many dimer transitions as well as strong trimer transitions when using 3% CO_2 in He at 5 atm backing pressure with a 0.04 mm diameter nozzle. Again, using the "corresponding jets" model, we would predict that trimers would be formed at a source pressure of 1.9 atm with our 0.2 mm nozzle. One observation by Fraser *et al.*[126] that is relevant here is that the intensity of the trimer peaks in the infrared spectrum was much more strongly dependent on source pressure than was the intensity of the dimer peaks. For example, at 2 atm backing pressure, a few weak dimer transitions were visible but no trimer peaks. At 3 atm, both trimer and dimer peaks are apparent. At 5 atm, the trimer peaks dominate the spectrum but the intensity of the dimer peaks is approximately equal to the dimer intensity in the 3 atm experiment. In our experiments, the regular set of observed peaks was found to be relatively insensitive to the source conditions. That is, the frequencies of the dominant peaks are consistent in spectra taken over a range of 1-5 atm source pressure, suggesting that the primary contributor to the observed transitions is a single species which we believe to be $(CO_2)_2$. Trimers and higher order polymers are undoubtedly formed however, and may be contributing to some of the "noise" of the observed spectra.

Spectral simulation

With many of the complicating factors dropping out, it becomes conceivable that the observed dimer spectrum might be simulated using a simple model. The use of a simple model is mandatory since we have no direct knowledge of the proper peak assignments nor of the rotational and centrifugal distortion constants of this excited state. Thus, in the spectral simulation described below, the CO_2 dimer was constrained to fit a prolate symmetric top model with the B rotational constant taken to be the average of B and C. The ground state rotational and centrifugal distortion constants were taken from Jucks *et al.*[118] and are listed in Table 5.2.

The energy of each J,K level was calculated with the expression

$$E(J,K) = B[J(J+1)-K^2] + AK^2 - \Delta_J[J(J+1)]^2 - \Delta_{JK}[J(J+1)K^2] - \Delta_K K^4 \quad (5.2)$$

with the frequency of each $\Delta J=0$, $\Delta K=0$ transition calculated from

$$Q(J,K) = \nu_0 + E''(J,K) - E'(J,K). \quad (5.3)$$

Each transition is given a relative CARS intensity by multiplying the transition degeneracy by the square of the ground state Boltzmann population factor. Then each line was given a Lorentzian lineshape to account for natural and any residual collisional broadening and the spectrum was convoluted with Gaussian lineshape functions to account for Doppler and instrumental broadening effects as described in Chapter 3.

In an attempt to fit the experimental spectrum, a range of values of (B′-B″), (A′-A″), and (Δ_J′-Δ_J″) was tried. Unfortunately, to reproduce the observed equal line spacing, it was necessary to use a value for (B′-B″) that was an order of magnitude larger than the equivalent values observed in the infrared ν_3 and $2\nu_2+\nu_3$ studies[116,118] that are shown in Table 5.2. In fact, to counteract the spreading of high J lines due to the J(J+1) term in Equation 5.2, it was necessary to use a value of $\Delta J'$ ten times greater than $\Delta J''$. This reflects the need to consider the asymmetry of the molecule and also to obtain higher resolution coherent Raman data so that a band origin and a few of the rotational lines of the dimer might be assigned.

CONCLUSION

We have observed a set of sharp, regular lines in the vicinity of the CO_2 ν_1 monomer peak that we are led to attribute to rovibrational transitions of the carbon dioxide dimer. Despite the difficulty in modeling the experimental spectrum with a simple symmetric top model, it is encouraging that several possible perturbing factors are found to be relatively unimportant. As higher resolution CARS capabilities are developed, it would be useful to reexamine this problem with the goal of specifically assigning each transition, thereby obtaining an insight into the intermolecular vibrations and rotations of this simple yet complex system.

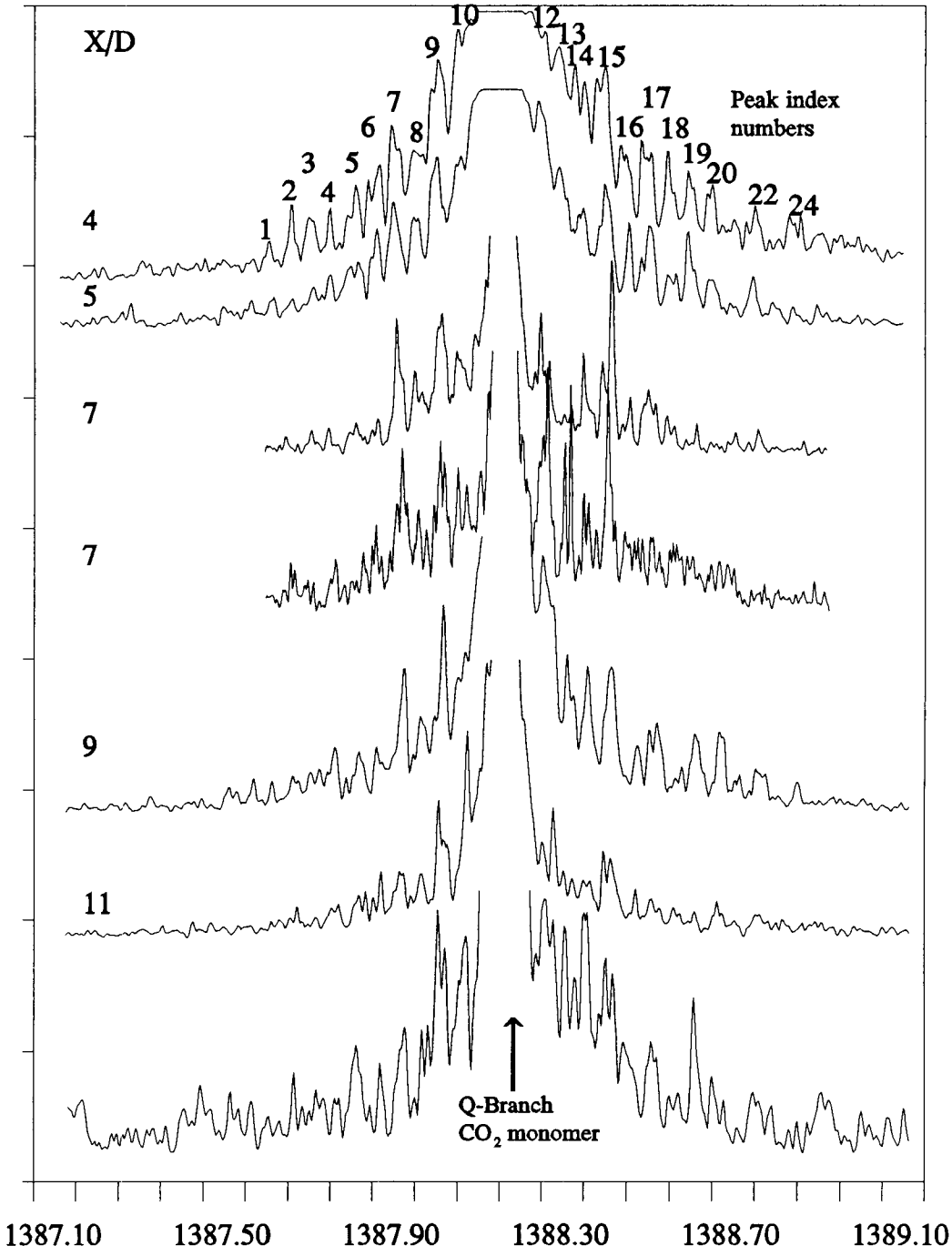

Figure 5.1: CO_2 dimer spectra. Obtained using a mixture of 2% CO_2 in Ne at 2 atm backing pressure.

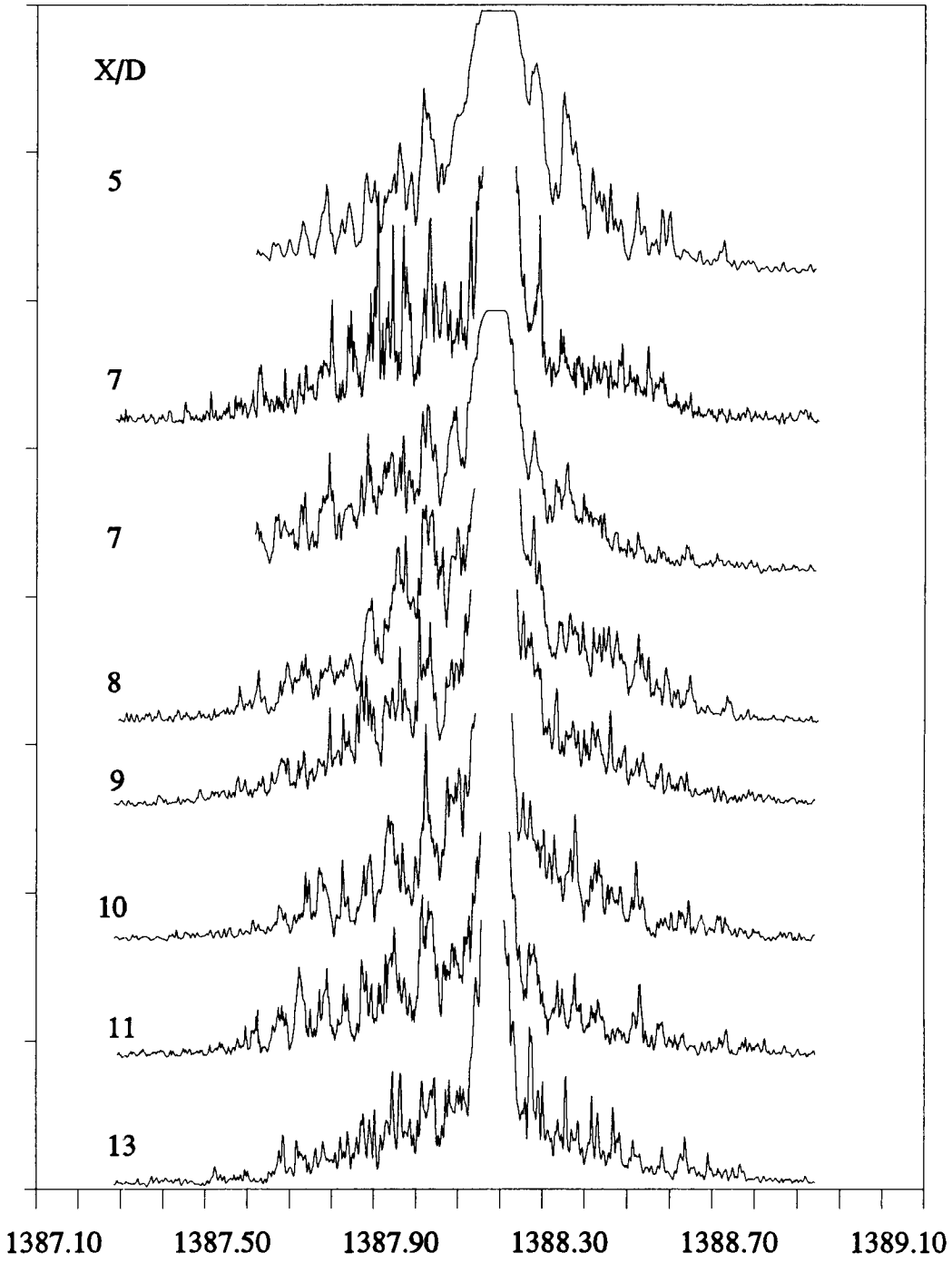

Figure 5.2: CO_2 dimer spectra. Obtained using a mixture of 2% CO_2 in Ne at a source pressure of 1.6 atm.

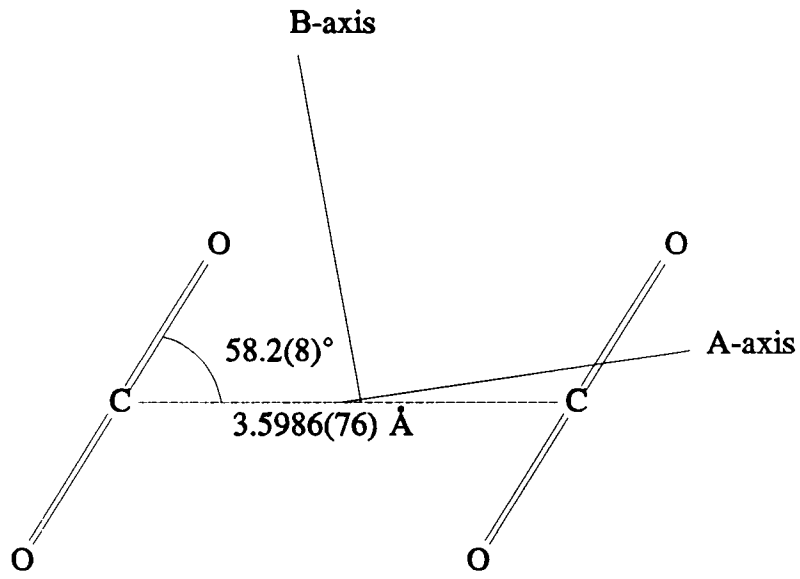

Figure 5.3: CO_2 dimer structure. Structural values are from Jucks *et al.*[122].

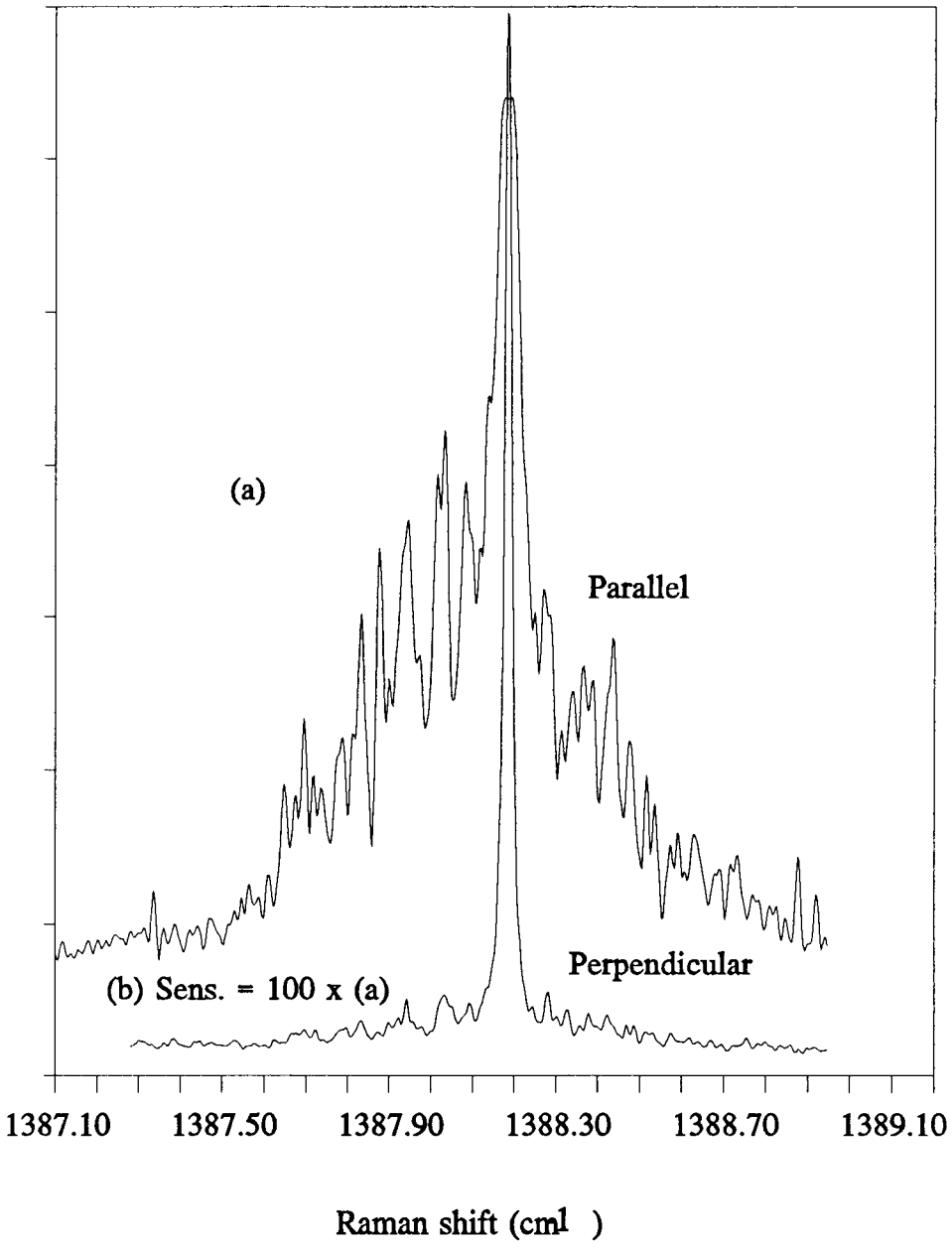

Figure 5.4: Polarization of CO_2 dimer transitions. (a) Parallel polarization. (b) Perpendicular polarization with the sensitivity = 100 x sensitivity of (a).

Table 5.1: Observed $(CO_2)_2$ peak frequencies and separations.

Peak no.	peak frequency	std. deviation of peak freq.	peak-peak separation
1	1387.640	0.0070	
2	1387.690	0.0107	0.0493
3	1387.742	0.0091	0.0526
4	1387.795	0.0116	0.0528
5	1387.846	0.0082	0.0510
6	1387.896	0.0089	0.0498
7	1387.945	0.0096	0.0492
8	1387.984	0.0103	0.0384
9	1388.039	0.0006	0.0556
10	1388.099	0.0099	0.0597
11	1388.287	0.0092	
12	1388.341	0.0112	0.0541
13	1388.383	0.0082	0.0421
14	1388.438	0.0081	0.0548
15	1388.487	0.0087	0.0488
16	1388.536	0.0079	0.0486
17	1388.595	0.0123	0.0591
18	1388.640	0.0106	0.0454
19	1388.687	0.0024	0.0465
20	1388.735	0.0012	0.0481
21	1388.784	0.0073	0.0491
22	1388.830	0.0025	0.0458
23	1388.881	0.0083	0.0511
		average:	0.050(5)

Table 5.2: Rotational constants and structural parameters of $(CO_2)_2$.

	Ground state[a]	$2\nu_2+\nu_3$[a]	$\nu_1+\nu_3$[a]	ν_3[b]
Rotational				
A	0.3002815(39)	0.2985585(43)	....	0.300538(27)
B	0.0536041(13)	0.0536563(16)	0.053900(25)	0.053299(4)
C	0.0453370(13)	0.0453396(14)	0.044163(15)	0.045142(4)
$\Delta_J x10^7$	2.831(55)	2.636(53)	....	2.26(19)
$\Delta_{JK} x10^7$	-2.393(61)	-2.460(52)	....	1.90(3)
$\Delta_K x10^5$	1.343(33)	1.340(18)	....	1.37(2)
$\delta_J x10^8$	5.79(32)	4.28(33)	....	
$\delta_K x10^6$	1.40(6)	1.56(44)	....	
Structural				
ν_0 (cm^{-1})	....	3611.54717(2)	3713.93215(6)	2350.77212(5)
$R_{C...C}$ Å	3.599(7)			3.6081(2)
θ°	58.2(8)			57.65(2)

[a]Ref. 118. [b]Ref. 116.

BIBLIOGRAPHY

1. Raman, C.V. and Krishnan, K.S., *Nature*, 121, 501 (1928).

2. Woodbury, E.G. and Ng, W.K., *Proc. IRE*, **50**, 2367 (1962).

3. Maker, P.D. and Terhune, R.W., *Phys. Rev. A.*, **137**, 801 (1965).

4. Eckbreth, A.C., *Appl. Phys. Lett.*, **32**, 421 (1978).

5. Eesley, G.L., Coherent Raman Spectroscopy, Academic Press, New York, 1982.

6. Levenson, M.D., Introduction to Nonlinear Laser Spectroscopy, Academic Press, New York, 1982.

7. Shen, Y.R., The Principles of Nonlinear Optics, Wiley, New York, 1984.

8. Anderson, H.C. and Hudson, B.S. in Molecular Spectroscopy, ed by D.A. Long, Vol. 5, Chemical Society, New York, 1977.

9. Yuratich, M.A. and Hanna, D.C., *Mol. Phys.*, **33**, 671 (1977).

10. Tolles, W.M., Nibler, J.W., MacDonald, J.R., Harvey, A.B., *Appl. Spectrosc.*, **31**, 253 (1977).

11. Nibler, J.W. and Knighten, G.V., Chap. 7. in Raman Spectroscopy of Gases and Liquids, ed. by A. Weber, Topics in Current Physics, Vol. 11, Springer-Verlag, Berlin and New York, 1979.

12. Nibler, J.W. and Pubanz, G.A., Chap. 1 in Advances in Non-linear Spectroscopy, ed. by R.J.H. Clark and R.E. Hester, Wiley, New York, 1987.

13. Chemical Applications of Nonlinear Raman Spectroscopy, A.B. Harvey, (ed.), Academic Press, New York, 1981.

14. Druet, S. and Taran, J.P., *Prog. Quant. Electr.*, **7**, 1 (1982).

15. Esherick, P. and Owyoung, A., in Advances in Infrared and Raman Spectroscopy, Vol. 9, ed. by R.J.H. Clark and R.E. Hester, Heyden and Son, London, 1982.

16. Maeda, S., Kamisuki, T., Kataoka, H., and Adachi, Y., *Appl. Spectrosc. Rev.*, **21**, 211 (1985).

17. Non-linear Raman Spectroscopy and Its Chemical Applications, ed by W. Kiefer and D.A. Long, NATO Series C, Vol. 93, Reidel, London, 1982.

18. Proc. Xth Intnl. Conf. on Raman Spectrosc., ed. by W.L. Peticolas and B. Hudson, University of Oregon Press, Eugene, 1986.

19. Maier, M., Kaiser, W., Giordmaine, J.A., *Phys. Rev.*, **177**, 580 (1969).

20. Bloembergen, N., Nonlinear Optics, Benjamin, New York, 1965.

21. Lallemand, P. in The Raman Effect, ed. by A. Anderson, Vol. 1, Dekker, New York, 1971.

22. Flytzanis, C. in Quantum Electronics: A Treatise, ed. by H. Rabin and C.L. Tang, Vol. 1, Part A, Academic Press, New York, 1975.

23. Yariv, A., Quantum Electronics, Wiley, New York, 1975.

24. Hellwarth, R.W., *Prog. Quant. Electr.*, **5**, 1 (1977).

25. Ducuing, J. in Nonlinear Optics, ed. by P.G. Harper and B.S. Wherrett, Academic Press, New York, 1977.

26. Moureu, C. and Bongrand, J.C., *Bull. Soc. Chim.* **5**, 846 (1909).

27. Chien, J.C.W. and Carlini, C., *J. Polym. Sci., Polym. Chem. Ed.*, **23**, 1383, (1985).

28. Khanna, R.K., Perere-Jarmer, M.A., Ospina, M.J., *Spectrochim. Acta*, **3**, 421 (1987).

29. Kunde, V.G., Aikin, A.C., Hanel, R.A., Jennings, D.E., Maguire, W.E., Samuelson, R.E., *Nature (London)*, **292**, 683, (1981).

30. Miller, F.A. and Hannan, R.B., *J. Chem. Phys.*, **21**, 110 (1953).

31. Miller, F.A., Hannan, R.B., Cousins, L.R., *J. Chem. Phys.*, **23**, 2127 (1955).

32. Hannan, R.B. and Collin, R.L., *Acta. Crystallogr.*, **6**, 350 (1953).

33. Moureu, C. and Bongrand, J.C., *Ann. Chem.*, **14**, 5 (1920).

34. Nibler, J.W. and Pubanz, G.W., in Advances in Non-Linear Spectroscopy, Clark, R.J.H., Hester, R.E., Eds., Wiley, Chichester, U.K. (1988) Vol. 15, Chapter 1.

35. Gunderson, G. and Hedberg, K., *J. Chem. Phys.*, **51**, 2500, (1969).

36. Hedberg, L. *Abstracts,* Fifth Austin Symposium on Gas Phase Molecular structure, Austin, TX 1974, p.37.

37. Robiette, A.G., in Molecular Structure by Diffraction Methods, Sim, G.A., Sutton, L.E., senior reporters; Burlington House, London (1973), Vol. 1, Chapter 4.

38. Schactschneider, J.H., Shell Development Co. Technical Report No. 57-65 (1965).

39. Lafferty, W.G., Maki, A.G., Plyler, E.K., *J. Chem. Phys.*, **40**, 224 (1964).

40. Herzberg, G Molecular Spectra and Molecular Structure III: Electronic Spectra and Electronic Structure of Polyatomic Molecules, Van Nostrand, Princeton, NJ (1966).

41. Frisch, M.J., Binkley, J.S., Schlegel, H.B., Raghavachari, K., Melius, C.F., Martin, R.L., Stewart, J.J.P., Bobrowicz, F.W., Rohlfing, C.M., Kahn, L.R., Defrees, D.J., Seeger, R., Whiteside, R.A., Fox, D.J., Fleuder, E.M., Pople, J.A. GAUSSIAN 86, Carnegie-Mellon Quantum Chemistry Publishing Unit, Pittsburgh, PA (1984).

42. Ohshima, Y., Yamamoto, S., Kuchitsu, K., *Acta Chem. Scand. A*, **42**, 307 (1988).

43. Pariseau, M.A., Suzuki, H., Overend, J., *J. Chem. Phys.*, **42**, 2335 (1965).

44. Smith, D.F. Jr., Overend, J., *J. Chem. Phys.*, **54**, 3632 (1971).

45. Ohshima, Y., Yamamoto, S., Nakata, M., Kuchitsu, K., *J. Chem. Phys.*, **91**, 4696 (1987).

46. Tanimoto, M., Kuchitsu, K., and Morino, Y., *Bull. Chem. Soc. Jpn.*, **44**, 386 (1971).

47. Morino, Y., Kuchitsu, K., Hori, Y., Tanimoto, M., *Bull. Chem. Soc. Jpn.*, **41**, 2349 (1968).

48. Cyvin, S.J. and Meisingseth, E., *Acta Chem. Scand.*, **22**, 1289 (1969).

49. Smith, W.H. and Leroi, G.E., *J. Chem. Phys.,* **45**, 1767 (1966).

50. Fusina, L. and Mills, I.M., *J. Mol. Spectrosc.*, **89**, 123 (1980).

51. Callomon, J.H. and Stoicheff, B.P., *Can. J. Phys.*, **35**, 373 (1957).

52. Westenberg, A.A. and Wilson, E.B. Jr., *J. Am. Chem. Soc.*, **72**, 199 (1950).

53. Maki, A.G., *J. Chem. Phys.*, **43**, 3193 (1965); Edwards, H.G.M. and Mansour, H.R., *J. Mol. Struct.*, **160**, 209 (1987).

54. Baducci, A., Ghersetti, S., Hurlock, S.C., Rao, K.N., *J. Mol. Spectrosc.*, **59**, 116 (1976).

55. Rank, D.H., Skorinko, G., Eastman, D.P., Wiggins, T.A., *J. Opt. Soc. Am.*, **50**, 421 (1960).

56. Rasetti, F., *Z. Phys.*, **61**, 598 (1930).

57. Jammu, K.S., St. John, G.E., Welsh, H.L., *Can. J. Phys.*, **44**, 797 (1966).

58. Rich, N.H., Lepard, D.W., *J. Mol. Spectros.*, **38**, 549 (1971).

59. Renschler, D.L., Hunt, J.L., McCubbin, T.K., Polo, S.R., *J. Mol. Spectros.*, **31**, 173 (1969).

60. Altmann, K., Strey, G., Hochenbleicher, J.G., Brandmuller, J., *Z. Naturforsch.* **27**, 56 (1972).

61. Hill, R.A., Owyoung, A., Esherick, P., *J. Mol. Spectros.*, **112**, 233 (1985).

62. Lepard, D.W., *Can. J. Phys.*, **48**, 1664 (1970).

63. Kramers, A., *Z. Physik*, **53**, 422 (1929).

64. Butcher, R.J., Willetts, D.V., Jones, W.V., *Proc. Roy. Soc. Lond. A.*, **324**, 231 (1971).

65. Berard, M., Lallemand, P., Cebe, J.P., Giraud, M., *J. Chem. Phys.*, **78**, 672 (1983).

66. Johns, J.W.C. and Lepard, D.W., *J. Mol. Spectros.*, **55**, 374 (1975).

67. Gerstenkorn, S. and Luc, P. Atlas du Spectre d'Absorption de la Molecule d'Iode, Editions du Centre National de la Recherche Scientifique, Paris, 1978; *Rev. Phys. Appl.*, **14**, 791 (1979).

68. Greenhalgh, D.A. in Advances in Non-Linear Spectroscopy, ed. by R.J.H. Clark and R.E. Hester, John Wiley & Sons, New York, 1988.

69. Ouazzany, Y., Boquillon, J.P., Lavorel, B., *Can. J. Phys.*, **65**, 1588 (1987).

70. Berard, M. and Lallemand, P., *Opt. Commun.*, **30**, 175 (1979).

71. Palmer, R.E., "CARSFT Computer Code", Sandia Report SAND89-8206, UC-13, NTIS copy A03.

72. Weber, A. in The Raman Effect, vol. 2, ed. by A. Anderson, M. Dekker, N.Y. (1973).

73. Farrow, R.L. and Rahn, L.A., *Phys. Rev. Lett.*, **48**, 395 (1982).

74. Gardiner, W.C. Jr., Pickett, H.M., Proffitt, M.H., *J. Chem. Phys.*, **63**, 2149 (1975).

75. Anderson J.B. in Molecular Beams and Low Density Gasdynamics, ed by P. Wegener, Dekker, Inc., NY (1974).

76. Hagena, O.F. in Molecular Beams and Low Density Gasdynamics, ed. by P.P. Wegener, Dekker, Inc., NY (1974).

77. Ashkenas, H. and Sherman, F.S., in Rarefied Gas Dynamics, ed by J.H. de Leeuw, Vol. II, Academic Press, NY (1966).

78. Pubanz, G.A., Maroncelli, M., Nibler, J.W., *Chem. Phys. Lett.*, **120**, 313 (1985).

79. Hopkins, G.A., Maroncelli, M., Nibler, J.W., Dyke, T.R., *Chem. Phys. Lett.*, **114**, 97 (1985).

80. Beck, R., Nibler, J.W., *Chem. Phys. Lett.*, **148**, 271 (1988).

81. Beck, R.D., Hineman, M.F., Nibler, J.W., *J. Chem. Phys.*, **92**, 7068 (1990).

82. McDonald, J.E., *Am. J. Phys.*, **30**, 870 (1962).

83. Plummer, P.L.M. and Hale, B.J., *J. Chem. Phys.*, **56**, 4329 (1972).

84. Stein, G.D. *The Physics Teacher*, **17**, 503 (1989).

85. Hagena, O.F. and Obert, W., *J. Chem. Phys.*, **56**, 1793 (1972).

86. Fermi, E., *Z. Physik*, **71**, 250 (1931).

87. Ouillon, R., Ranson, P., and Califano, S., *J. Chem. Phys.*, **83**, 2162 (1985).

88. Richardson, A., Master's thesis, Oregon State University, to be written.

89. Pubanz, G.A., Ph.D. Thesis, Oregon State University (1986).

90. Kappes, M. and Leutwyler, S., in Atomic and Molecular Beam Methods, chap. 15, Vol. 1, ed. by G. Scoles, Oxford University Press, New York, 1988.

91. Beck, R., PhD Dissertation, Oregon State University, 1989.

92. Torchet, G., Bouchier, H., Farges, J., de Feraudy, M.F., Raoult, B., *J. Chem. Phys.*, **81**, 2137 (1984).

93. Farges, J., de Feraudy, M.F., Raoult, B., Torchet, G., *Surf. Science*, **106**, 95 (1981).

94. Levy, D.H., *Ann. Rev. Phys. Chem.*, **31**, 197 (1980).

95. Tolman, R.C., *J. Chem. Phys.*, **17**, 333 (1947).

96. Wegener, P.P. and Parlange, J.Y., *AGARD Conf. Proc.*, **12**, 64 (1967).

97. Giauque, W.F. and Egan, C.J., *J. Chem. Phys.*, **5**, 45 (1937).

98. Braker, W. and Mossman, A.L., Matheson Gas Data Book, 6th Ed., Matheson, Secaucus, NJ, 1980, p. 125.

99. Barth, H.-D. and Huisken, F., from address given at The International Symposium on Coherent Raman Spectroscopy, Samarkand, USSR, September, 1990.

100. Miller, R.E., Watts, R.O., Ding, A., *Chem. Phys.*, **83**, 155 (1984).

101. Cardini, G., Schettino, V., Klein, M.L., *J. Chem. Phys.*, **90**, 4441 (1989).

102. Barnes, J.A. and Gough, T.E., *J. Chem. Phys.*, **86**, 6012 (1987).

103. van de Waal, B.W., *J. Chem. Phys.*, **79**, 3948 (1983).

104. Burton, J.J., *J. Chem. Phys.*, **52**, 345 (1970); Hoare, M.R. and Pal, P., *Nature (London)*, **230**, 5 (1971); Fukano, Y. and Wayman, C.M., *J. Appl. Phys.*, **40**, 1656 (1969).

105. Mannik, L, Stryland, J.C., Welsh, H.L., *Can. J. Phys.*, **49**, 3056 (1971).

106. Novick, S.E., Davies, P.B., Dyke, T.R., Klemperer, W., *J. Am. Chem. Soc.*, **95**, 8547 (1973).

107. Fredin. L., Nelander, B., Ribbegard, G., *J. Mol. Spectrosc.*, **53**, 410 (1974).

108. Hashimoto, M. and Isobe, T., *Bull. Chem. Soc. Jpn.*, **47**, 40 (1974).

109. Lobue, J.M., Rice, J.K., Novick, S.E., *Chem. Phys. Lett.*, **112**, 376 (1984).

110. Koide, A. and Kihara, T., *Chem. Phys.*, **5**, 34 (1974).

111. Brigot, N, Odiot, S., Walmsley, S.H., Whitten, J.L., *Chem. Phys. Lett.*, **49**, 157 (1977).

112. Guasti, R., Schettino, V., Brigot, N., *Chem. Phys.*, **34**, 391 (1978).

113. Barton, A.E., Chablo, A., Howard, B.J., *Chem. Phys. Lett.*, **60**, 414 (1979).

114. Gough, T.E., Miller, R.E., Scoles, G., *J. Phys. Chem.*, **85**, 4041 (1981).

115. Miller, R.E. and Watts, R.O., *Chem. Phys. Lett.*, **105**, 409 (1984).

116. Walsh, M.A., England, T.H., Dyke, T.R., Howard, B.J., *Chem. Phys. Lett.*, **142**, 265 (1987).

117. Jucks, K.W., Huang, Z.S., Dayton, D., Miller, R.E., Lafferty, W., *J. Chem. Phys.*, **86**, 4341 (1987).

118. Jucks, K.W., Huang, Z.S., Miller, R.e., Fraser, G.T., Pine, A.S., Lafferty, W.J., *J. Chem. Phys.*, **88**, 2185 (1988).

119. Vigasin, A.A. and Denisov, A.N., *Dokl. Akad. Nauk SSSR*, **310**, 55 (1990).

120. Buck, U., Lauenstein, C., Sroka, R., Tolle, M., *Z. Phys. D*, **10**, 303 (1988).

121. Hagena, O.F., in Rarefied Gas Dynamics, ed. by L. Trilling and H.Y. Wachman, Vol. II, p. 1465, Academic, New York 1969.

122. Rothman, L.S., *Applied Optics*, **25**, 1795 (1986).

123. Montero, S., personal communication, 9 Sept. 1991, Corvallis, Oregon.

124. Montero, S., *Indian J. Pure & Appl. Phys.*, **16**, 186 (1978).

125. Montero, S. and del Rio, G., *Molecular Physics*, **31**, 357 (1976).

126. Fraser, G.T., Pine, A.S., Lafferty, W.J., Miller, R.E., *J. Chem. Phys.*, **87**, 1502 (1987).